POLITECNICO
MILANO 1863

Scuola di Ingegneria Industriale e dell'Informazione

Laurea Magistrale in Ingegneria Nucleare

in collaborazione con il Dipartimento di Fisica e Istituto di Fotonica e Nanotecnologie IFN-CNR

Femtosecond Laser Writing of a Broadband Integrated Nulling Interferometer for Exoplanet Detection

Candidato : **Andrea Baglivo**
Matricola: **893396**

Supervisore : **Professor Roberto Osellame**
Co-supervisore : **Simone Piacentini**

Anno Accademico 2019-2020

ABSTRACT

The observation of exoplanets has gained an increasing interest in the recent years, since their study could provide information about their composition and habitability. However, the direct imaging of exoplanets is a challenging task, since the light they emit is much fainter than the one of their host stars. In this respect, nulling interferometry is a technique capable of removing the contaminating starlight by destructive interference, leaving only the exoplanet signal to be analyzed. This technique can take advantage of an integrated approach for achieving a higher interferometric stability and a miniaturization of the setup. However, integrated photonic devices usually show a response dependent both on the polarization and the wavelength of the incoming light, so they should be used together with filters and polarizers, further reducing the faint exoplanet signal.

In this work we present the development of an integrated nulling interferometer with a behavior independent of polarization and wavelength of the injected light. The device was fabricated by Femtosecond Laser Micromachining in glass, followed by a thermal annealing process for reducing the waveguides losses and birefringence, thus achieving polarization insensitivity. The circuit is composed of a cascade of directional couplers, with reduced interaction length and distance for broadband operation, and was designed for performing the interference of the light collected by two telescopes. The characterization with classical light showed overall insertion losses of 2 dB, and a variation of the splitting ratio of the couplers < 2% depending on the input polarization and < 5% in the spectral range 1310 nm – 1610 nm. The fabrication of thermal phase shifters on top of the waveguides will allow a full control of the phase difference of the input beams, enabling the cancellation of the star signal.

SOMMARIO

L'osservazione di esopianeti ha riscosso un interesse crescente negli ultimi anni, dal momento che il loro studio può fornire informazioni sulla loro composizione e abitabilità. Tuttavia, l'osservazione diretta di esopianeti è un arduo compito, poiché la luce che emettono è molto più debole di quella della stella intorno a cui orbitano. In questo contesto, la nulling interferometry è una tecnica capace di rimuovere l'indesiderata luce stellare attraverso interferenza distruttiva, ottenendo come risultato il solo segnale del pianeta che può essere analizzato. Questa tecnica può avvalersi di un approccio integrato per raggiungere una più alta stabilità interferometrica e una miniaturizzazione della strumentazione. Tuttavia, i dispositivi ottici integrati solitamente mostrano una risposta dipendente sia dalla polarizzazione che dalla lunghezza d'onda della luce in ingresso, perciò dovrebbero essere utilizzati insieme a filtri e polarizzatori, riducendo ulteriormente il debole segnale planetario.

In questo lavoro presentiamo lo sviluppo di un interferometro integrato capace di estinguere la luce stellare in modo indipendente dalla polarizzazione e dalla lunghezza d'onda della luce in ingresso. Il dispositivo è stato realizzato in un campione di vetro attraverso la microfabbricazione con laser a femtosecondi, seguita da un processo di rilassamento termico per ridurre le perdite delle guide e la birifrangenza, raggiungendo così l'insensibilità alla polarizzazione. Il circuito è composto da una cascata di accoppiatori direzionali, con lunghezza di interazione e distanza ridotte per operazioni a banda larga, ed è stato progettato per implementare l'interferenza della luce raccolta da due telescopi. La caratterizzazione con luce classica ha mostrato delle perdite di inserzione complessive di 2 dB, e una variazione della riflettività degli accoppiatori <2% in base alla polarizzazione in ingresso e <5% su una banda spettrale tra 1310-1610 nm. La fabbricazione di sfasatori termici al di sopra delle guide d'onda consentirà un pieno controllo della differenza di fase degli fasci in ingresso, permettendo la cancellazione del segnale della stella.

Riassunto

La ricerca di pianeti al di fuori del sistema solare e lo studio delle loro caratteristiche è un tema centrale nell'astrofisica moderna. Non solo si cercano indizi sull'esistenza di forme di vita diverse dalla nostra, ma si vuole anche ampliare la comprensione delle dinamiche che hanno portato alla formazione del nostro sistema solare, aprendo le porte a risvolti fondamentali nella fisica moderna. Dato che l'oggetto di studio sono corpi celesti lontanissimi che orbitano attorno a stelle molto più luminose di loro, è molto difficile saperli individuare e distinguere con chiarezza. Per questo motivo, esistono molte tecniche di rilevazione, che spesso traggono forza dalla loro sinergia. Nella maggior parte dei casi, si usano evidenze indirette dell'esistenza di un esopianeta: si possono individuare oscillazioni che questi inducono nello spettro di emissione di una stella o una riduzione dell'intensità luminosa di questa dovuta al loro transito. Ci sono tecniche che addirittura sono capaci di individuare alterazioni del tessuto spazio-temporale di una stella esercitate dalla presenza di un pianeta orbitante attorno. Tuttavia questi metodi, seppur in grado di individuare i pianeti, non sono in grado di carpine tutte le loro proprietà. Se si riuscisse a isolare la luce di un esopianeta, si potrebbe ricostruire la mappa della loro atmosfera, conoscere le condizioni di pressione e temperatura, rilevare le tracce di specifiche molecole presenti su di esso ed di eventuali indicatori biologici. Un approccio di questo tipo prende il nome di imaging diretto, in quanto si analizza direttamente la luce emessa dal pianeta, contenente informazioni sullo spettro di trasmissione della sua atmosfera.

In tutti i casi in analisi, si fa affidamento su potenti telescopi, posti a distanza il più elevata possibile tra loro per incrementarne la risoluzione e quindi essere in grado di distinguere oggetti che appaiono vicinissimi. Tradizionalmente, la luce raccolta dai telescopi viene fatta interferire costruttivamente, in modo da accentuare il più possibile il segnale del pianeta. In questo modo, tuttavia, l'intensità della stella rimane, ed essendo la stella miliardi di volte più intensa, il guadagno che se ne trae è molto relativo. Nel 1978 Bracewell propose una metodologia alternativa: anziché far interferire costruttivamente i segnali provenienti dai telescopi, è possible invece selettivamente annullare il segnale della stella, lasciando inalterato il segnale del pianeta. Questa tecnica è chiamata nulling interferometry e il suo scopo è quello di filtrare dalla luce analizzata il contributo stellare, salvando il flebile pianeta. Il grande vantaggio è che non ci sono limitazioni riguardo all'intensità della stella e quindi potenzialmente anche il più debole pianeta può essere scoperto.

La luce analizzata con tecniche di imaging diretto può appartenere sia allo spettro visibile che all'infrarosso; in quest'ultima finestra spettrale però l'emissione del pianeta, che si trova a temperature inferiori rispetto alla una stella, risulta più marcata, mentre la stella avrà una lunghezza d'onda di massima emissione verso valori più prossimi al visibile, nonostante ciò la sua intensità risulta comunque maggiore rispetto a quella del pianeta su tutta la banda spettrale. Quindi sono preferibili dispositivi che siano in grado di far interferire la luce nella zona infrarossa dello spettro elettromagnetico. Tuttavia, non tutta la luce può generare frange di interferenza: condizione necessaria è la natura coerente della luce in esame, che consiste nell'avere un fronte di fase costante nel tempo e nello spazio. Dato che l'emissione luminosa da parte di

stelle e pianeti è dovuta al comportamento casuale dei singoli atomi sulla loro superficie, l'operazione di interferenza apparirebbe impossibile, perché tali sorgenti sono per definizione incoerenti, dato che ciascun atomo emette radiazione indipendentemente dagli altri in istanti diversi nel tempo e quindi non in fase tra di loro. Tuttavia esiste un importante teorema in ottica, il quale afferma che se un corpo si trova a sufficiente distanza e può essere identificato come una sorgente puntiforme, allora è possibile trattarlo come una sorgente coerente, perché si instaura una correlazione nella luce emessa che dipende dalla posizione della sorgente stessa. Questo significa che un pianeta e una stella, occupando posizioni diverse nel cielo, saranno sorgenti di luce correlata con se stessa e che può quindi interferire solo con se stessa. Da qui si può capire come sia possibile eliminare il contributo della stella e non quello del pianeta: se si impone la condizione di interferenza distruttiva per la luce emessa dalla stella, si avrà comunque la possibilità di rivelare il segnale emesso dal pianeta, perché quest'ultimo si trova in una posizione angolare diversa rispetto alla stella, e quindi avrà un fronte di fase differente.

All'atto pratico, cancellare la luce di una stella non significa distruggere la sua luce, in quanto sarebbe una violazione del principio di conservazione dell'energia, bensì separare il suo contributo da quello del pianeta utilizzando un dispositivo che una volta raccolta tutta la luce dai telescopi abbia due uscite differenti, una delle quali senza la stella. Tutto ciò può essere realizzato da sofisticate strumentazioni, che nel caso più diffuso utilizzano sistemi di specchi e materiali purissimi per regolare il ritardo dei fasci e quindi la fase della luce in ingresso. Tali sistemi, seppur efficaci, hanno problematiche importanti. Grandi telescopi, come il Keck interferometer sulle isole Hawaii, devono tener conto degli effetti che l'atmosfera terrestre ha sulla luce raccolta, la quale è in grado di distorcere il fronte d'onda e di compromettere drasticamente il processo di interferenza, costringendo a ricorrere a complessi sistemi di ottica adattiva e elementi ottici, i primi estremamente sofisticati e questi ultimi contribuenti inevitabilmente ad una riduzione dell'intensità della luce in esame, rendendo ancora più difficile il processo di rilevazione.

Il lavoro sviluppato in questa tesi parte da qui: un interferometro integrato costituisce una tecnologia in grado di eliminare qualunque forma di disturbo che possa essere indotta dalla presenza dell'atmosfera, in quanto prevede intrinsecamente un'azione di filtraggio. L'interferometro integrato proposto in questo lavoro è un dispositivo costituito da un campione di vetro nel quale sono state scritte delle guide d'onda a singolo modo per mezzo di un laser a femtosecondi; il dispositivo prevede inoltre un controllo attivo della fase tra i due ingressi. Le guide d'onda sono zone dove un indice di rifrazione del vetro più elevato rispetto al resto del substrato permette di confinare e controllare la luce. La possibilità di guidare il solo modo fondamentale, quindi una sola distribuzione spaziale del campo elettrico della luce, è alla base dell'azione di filtraggio: le distorsioni del fronte d'onda si manifestano come variazioni del campo e quindi dell'intensità misurata, che fluttua durante la misurazione. Sistemi di ottica adattiva presenti nei grandi telescopi sicuramente incrementano l'efficienza della rilevazione, motivo per cui il dispositivo è stato realizzato per guidare luce infrarossa centrata a $\lambda = 1550$ nm, nella banda H di trasmissione dell'atmosfera terrestre e destinato ad essere validato proprio al Keck interferometer alle Hawaii.

L'interferometro presenta due ingressi per raccogliere la luce raccolta dai telescopi,

per poi ramificarsi: due rami si avvicinano per andare a costituire il cuore del dispositivo, l'accoppiatore direzionale, mentre gli altri due si allontanano costituendo i canali fotometrici, con i quali è possibile misurare l'intensità totale e controllare l'afflusso di luce nell'accoppiatore. Qui le due guide provenienti dagli ingressi si avvicinano, interagiscono tramite accoppiamento evanescente e si allontanano verso le uscite.

L'accoppiatore direzionale ha la capacità di distribuire l'intensità alle due uscite a seconda della differenza di fase che si impone ai suoi ingressi: ciascun ingresso dell'accoppiatore accoglierà un segnale contenente il contributo sia della stella che del pianeta e, attraverso un controllo della fase realizzato con degli sfasatori termici montati su di esso, sarà in grado di convogliare tutto il contributo della stella in una sola uscita, lasciando nell'altra solo quello del pianeta. Tutto ciò ha dei vincoli importanti, che costituiscono il fulcro di questo lavoro. Innanzitutto, per avere un processo di interferenza ottimale l'accoppiatore deve raccogliere segnali di pari intensità da ciascun ingresso e la sua capacità di dividere la luce nei due rami, detta *riflettività*, dovrà essere bilanciata, in caso contrario la cancellazione della stella sarebbe incompleta. Deve essere insensibile alla polarizzazione, ovvero la distribuzione dell'intensità deve essere indipendente dalla direzione di oscillazione del campo elettrico. Ma soprattuto questo comportamento bilanciato deve valere per il maggior numero di lunghezze d'onda possibili, coprendo una banda di almeno 100 nm. Il tutto deve essere progettato per minimizzare le perdite di propagazione che la luce inevitabilmente avrà all'interno del dispositivo.

Per realizzare un dispositivo con tutte queste caratteristiche, è stata impiegata la micro-fabbricazione con laser a femtosecondi. Questa tecnica consente di focalizzare un laser a impulsi molto brevi e intensi all'interno di un substrato trasparente e di promuovere un processo di assorbimento non lineare che consente di inscrivere le guide d'onda. Ottimizzando i parametri geometrici dell'accoppiatore e sperimentando diversi valori della velocità di scrittura, è stato studiato il coefficiente di accoppiamento evanescente e sono stati realizzati tanti accoppiatori con performance molto soddisfacenti. L'ampia risposta in banda è stata realizzata implementando accoppiatori a distanza ravvicinata ($\sim 6\ \mu m$) con lunghezza di interazione nulla, mentre l'insensibilità alla polarizzazione è stata ottenuta grazie ad un processo di annealing termico del vetro. Il comportamento bilanciato è stato raggiunto con un controllo dei raggi di curvatura e della velocità di scrittura che hanno consentito di modulare la curva di riflettività. Se la velocità di scrittura è la stessa per entrambi i rami, si ha un accoppiatore non detunato, in caso contrario detunato. I migliori valori di riflettività, comportamento in banda e polarizzazione sono leggermente migliori per gli accoppiatori detunati; tuttavia presentano un'asimmetria nel processo di fabbricazione che ha portato alla scrittura nel dispositivo finale di guide d'onda non detunate. Nel dispositivo finale, i valori di riflettività dell'accoppiatore centrale in base alla polarizzazione sono risultati inferiori al 2%, essendo al primo ingresso del 50.9% e 51.7% per polarizzazione verticale e orizzontale, di 51.6% e 52% al secondo. La variazione di comportamento in banda è inferiore al 5% su una finestra di 200 nm, risultato estremamente soddisfacente se rapportato alla letteratura. Le perdite di inserzione si attestano ad un valore inferiore a 2 dB.

La grandezza che appura maggiormente la qualità di un nulling interferometer è il rapporto di estinzione, i.e. l'intensità del canale di annullamento rapportata all'altra

uscita. Nonostante la realizzazione degli sfasatori termici non sia stata realizzata a causa della pandemia mondiale, una stima rudimentale di questo indice è stata ottenuta implementando un interferometro di Michelson modificato, ottenendo un valore di 2 10^{-2}. Tale valore è piuttosto lontano dalle performance richieste, che risulterebbero ottimali con due ordini di grandezza in meno. Tuttavia ha dimostrato l'effettivo funzionamento del dispositivo: si confida che la futura fabbricazione delle resistenze sulle guide d'onda porterà ad un notevole miglioramento delle prestazioni, in modo da poterne validare il funzionamento tramite delle misure al Keck interferometer alle isole Hawaii.

Contents

Are we alone in the universe? According to Isaac Asimov, *if we were alone, the immensity would really be a waste*. From centuries, all cultures of mankind turned their eyes upon the sky struggling with the burning desire of receiving a sign able to cancel the fear of existential loneliness. Although the eternal stars and the deepest skies of night have never given an answer, the inspiration of the crowned poets and the curiosity of the restless scientists are not faded away: they are trying every night to bring the human spirit closer to the truth.

We live at the birth of an exciting epoch, because for the first time in history we own devices allowing us to inspect the deepest zones of the universe, true eyes and ears capable of collecting clues coming from unknown worlds. The branch of science dealing with the study and solving the mysteries of the universe is *Astrophysics*, a discipline aiming to promote the human knowledge of our cosmo dealing with the main gift of a star: light.

In this frame, *Astrophotonics* plays a central role: this is a very new field of research, born at the beginning of the millenium, involving the manufacturing of miniaturized devices able to manipulate light particles, called photons, to get fundamental information about the emitter of the photons themself. We can reveal position, temperature, chemical components and several details only analyzing the light spread out between galaxies. Light is collected by a telescope then analyzed by *optical integrated circuits*, structures of different shape and functions, able to confine and guide photons in order to exploit their physical proprieties. These photon trails are called *waveguides* and their combination can make light splitters, directional couplers and other unities that can be combined to develop further processes.

There are billions and billions of shining objects and others whose nature is instead *obscure*; besides, not all the laws ruling the universe are today well understood and unified. We do not really know what we may discover studying stars and hunting new planets, but one thing is certain: in the past the study of sky has enriched also other science fields different from astrophysics. It happened when Newton, inspired by the Kepler Laws, formalized the Laws of Dynamics in his *Principia*. Isn't it a moral duty to give answers and try to do a little step forward a giant leap for mankind?

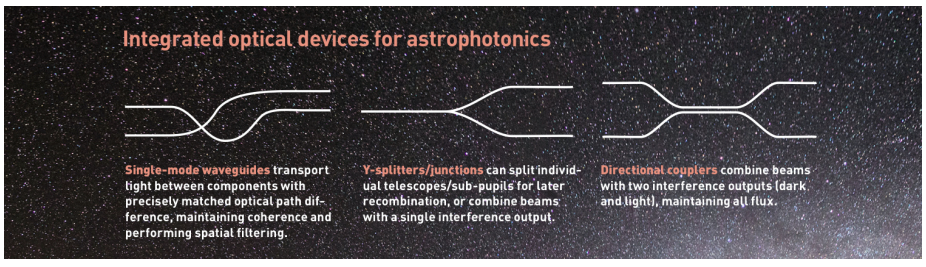

Figure 1: Main astrophotonic components [1].

1 Astrophotonics for exoplanet detection

1.1 Exoplanet research

An exoplanet is a planet living beyond our solar system **[2]**, which orbits a massive celestial object, like a star or a pulsar. Although there are no universally adopted criteria for establish a dividing line between planetary and other substellar objects **[3]**, a lot of conventions exist, dealing with the most characterizing physical proprieties. According to the IAU 2003 recommendation, a fundamental parameter is *mass*: an extrasolar planet is an object with a true mass below the limiting one for thermonuclear fusion of deuterium, independently of its formation **[4]**. If this limit is overcome, these systems are called *brown-drawfs*, whereas free-floating objects below the limiting mass are called *sub-brown-drawf* **[4]**. Some scientists rely more on their *formation*, labelling a planet as the product of disk accretion around a primary star or substar, quantifying the domination degree on the other masses sharing its orbiting zone **[5]**. This last definition can be in contrast with the former, because the two situations are not mutually exclusive; however this provides an upper mass limit, expressed in Jupiter masses, of $\sim 30\,M_J$, taken as reference for the NASA Exoplanet Archive **[3,4]**.
At the end of last year, the exoplanet count hit 4000. Very astonishing discovering have been made, thanks to the observation of extreme physical conditions reached on some of these planets. The extraordinary pressure and thermal excursion achievable due to gravity and to the vicinity to the host star have created states of matter that are only theoretical for us, because unachievable on Earth **[2]**. The Super-Earth *Cancri 55 e*, has physical proprieties that can be explained by a carbon-rich interior composition **[6]**, and due to the high pressure it could be in theory a diamond planet.

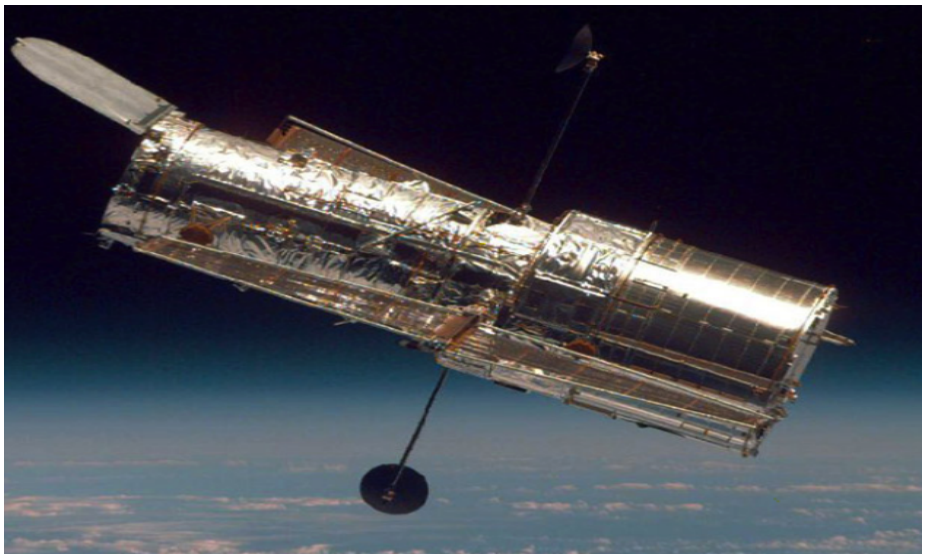

Figure 1: Hubble Space Telescope, launched in 1990, example of space-based-observation. It is considered a milestone of astronomy **[2]**.

A central task in these cosmological researches is to find planets where life is possible. The *Habitable zone* defines a region around a star that owns the right physical conditions for hosting liquid water covering a rocky planet. Energy source to drive metabolic reactions, liquid solvent and a suite of nutrients to build biomass and enzymes to catalyze these reactions are fundamental requirements for life development **[7]**.
It is clear the necessity to collect a lot of information about the atmospheric transmission spectra of the exoplanets, because these can provide clues about their composition, temperature, pressure and atmospherical structure; bisignature gases like oxygen, ozone and methane play a crucial role **[8]**.

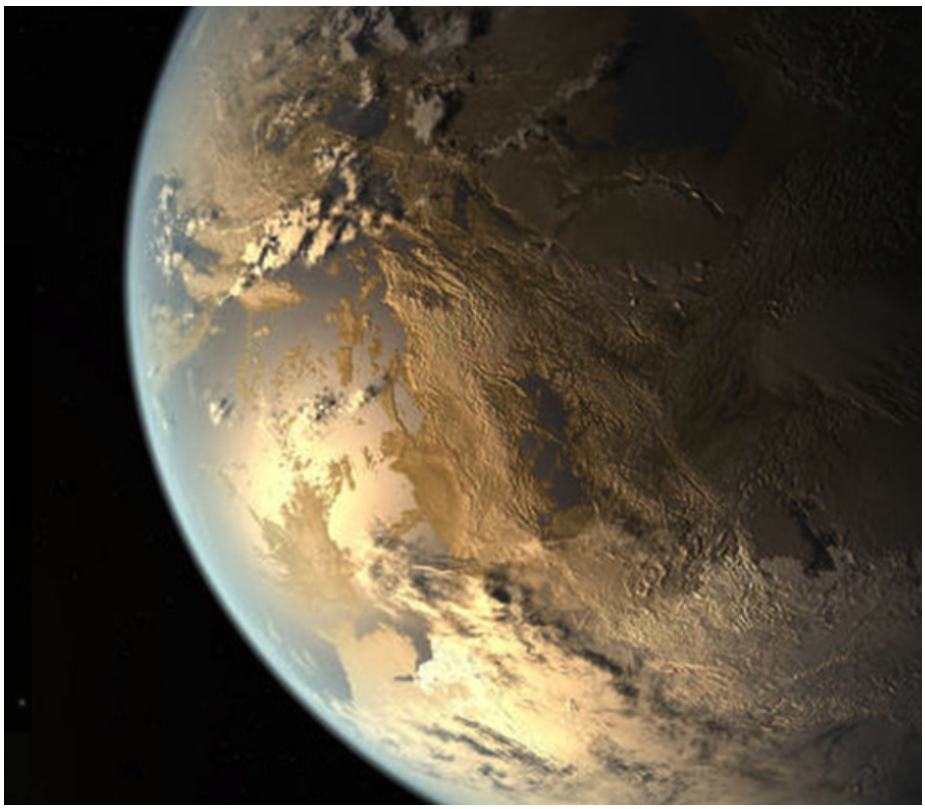

Figure 2: Artistic impression of Kepler 186f, the first Earth-sized exoplanet discovered in a Habitable zone, in 2014 thanks to the Kepler mission. The existence of liquid water is possible, it is 10% larger than Earth, rocky, orbiting a star half the size of the Sun. Kepler 186f is about 500 light-years far away **[2]**.

1.2 Detecting exoplanets

There are several methods applied by the astronomers to discover new worlds: this pluralism is fundamental because it allows to verify the validity of the publications comparing stellar, planetary and orbital results from different observations **[3]**. Aspects of planet motion and starlight emission are taken into account and their lack of completeness in grasping all the interesting features is sorted out by their simultaneous application, to obtain confirms from different points of view.

1.2.1 Radial velocity

The gravitational force induced by an orbiting planet affects the movement of its host star, generating by Doppler Effect a shift in the emitted light. This phenomenon is stronger the bigger is the exoplanet: in fact the radial velocity technique has roots in the study of binary star astronomy and the exoplanet applications represent the low-companion mass limit **[9]**. The method is largely used to confirm the existence of planets detected by other techniques, revolutionizing our understanding of the ubiquity and diversity of exoplanets **[10]**.
E.g., if the system Sun-Jupiter was seen from a distance of several light years, it would be possible to observe a sinusoidal variation in the amplitude of the radial velocity of 12 m s^{-1}; for six years above the mean and for other six below **[14]**. Among the main observatories able to detect the radial velocity we mention the Keck Telescopes in Hawaii and the La Silla Observatory in Chile.

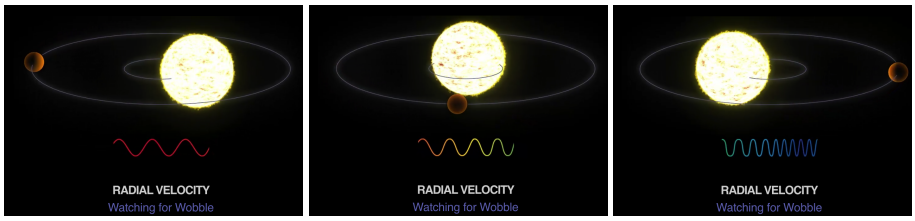

Figure 3: Doppler effect of a star induced by an orbiting planet, at the basis of the radial velocity detection method **[2]**.

1.2.2 Transit method

A planet orbiting a star projects a shadow, causing a reduction of the star's brightness. The scientists look for the transit-induced dimming, an event very similar to an eclipse we are familiar to. The light-curve in Fig. 4 gives important information about the size and the distance from the star: the deeper is the dimming, the bigger is the planet, being blocked a greater light amount. The longer the valley remains, the farther is the planet, because in this case the planet has a wider orbit and takes more time to cross the star, and the shadow lasts more.
This method has gained a great success, especially thanks to statistical data collected by the Hubble Space Telescope and the Kepler Mission **[28, 29]**; this last one discovered

the first exoplanet in the habitable zone **[2]**. The CHEOPS mission (CHaracterizing ExOplanets Satellite) is an important ground-based ESA mission aiming to improve the transit light curve of exoplanets below Neptune mass, discovered with radial velocity methods, and determine their radius **[11]**.

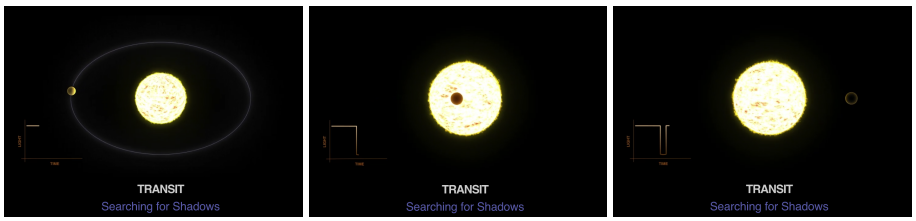

Figure 4: Exoplanet orbit and dimming curve in the transit observation, from **[2]**.

1.2.3 Direct imaging

The aim is to analyze directly the exoplanet's light removing the overwhelming contribution of its host star, which makes this task extremely hard. The traditional technique requires the usage of light-blockers, that allow the inspection of other objects, like a hand may do to reduce the blinding glare of the Sun in a summer's day. There are, up to now, two main consolidated methods : the first one, *coronography*, employs blockers in the telescope optics before light reaches the detector, and is mainly used in ground-based telescopes, i.e. telescopes located on the surface of Earth. The second one instead, *starshading*, employs shading devices before the telescope aperture for preventing the starlight to enter the telescope, and is mainly used in space-based observations in outer space. Direct imaging is at the beginning of its stages and it is very promising in the characterization of exoplanets, giving information about atmospheric patterns, oceans, landmasses, weather and signs of life **[2]**.
The DARWIN ESA mission had the task to detect Earth-like planets characterizing their atmospheres and involved the exploitation of several space-based telescopes, but it has been cancelled due to high cost **[27]**. The Space Spietzer Telescope has instead registered the first IR image of an exoplanet **[2]**.

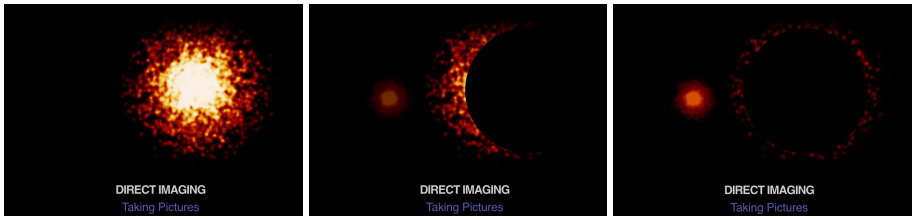

Figure 5: Representation of the light-blockers in direct imaging detection **[2]**.

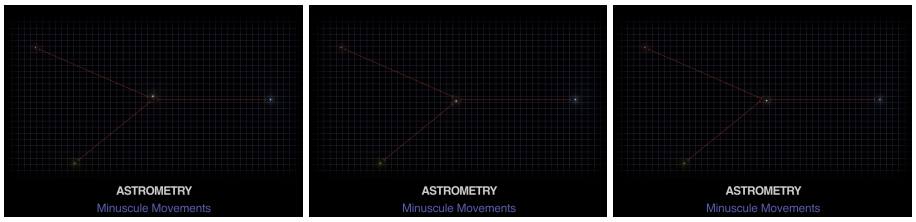

Figure 6: Schematic views of different position of a star with respect to other taken as reference points **[2]**.

1.2.4 Astrometry

A planet orbiting a star induces an oscillation of the star around the center of mass of the system, that can be inspected in relation to other fixed stars taken as points of reference. It is extremely difficult to grasp these star wobbles, especially for Earth-sized exoplanets which can have a lower gravitational force with respect to Jupiter-sized ones. This technique requires a very precise and stable optics, since the astronomers need to compare several pictures taken at different times. Moreover, the optical setup should allow to reduce the disturbance induced by the Earth's atmosphere, which may distort and bend starlight.

1.2.5 Gravitational microlensing

According to general relativity, the structure of the universe, space-time, can be distorted by massive objects. Light travels in space-time, so some bending effect can be observed: this change of direction of the light is successful when light of a distant star is focused to the observer due to another star with its exoplanet. These focus light with their transit, that results in a brightness increase, peak, and decrease, whereas the proper exoplanet action emerges in a brief blip of brightness due to its specific lensing action and this is the sign of its presence. Astronomers have to spend a lot of time observing the transit of celestial object hoping for a blip of light, that is not predictable and may also be caused by a free-floating planet in space **[2]**.

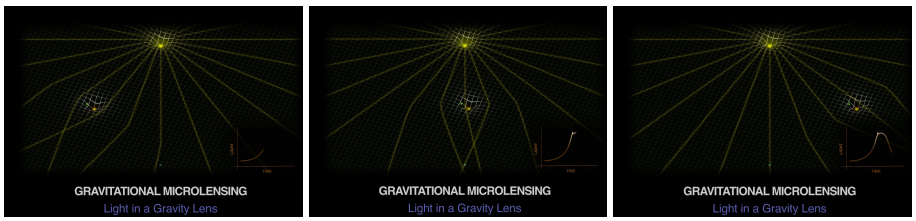

Figure 7: Deformation of space-time and microlensing action of a star-exoplanet system **[2]**.

1.3 Nulling interferometry

1.3.1 Young's Experiment

The nulling interferometry approach for exoplanet detection is inspired to the classical Young's Experiment. In 1802, Thomas Young conduced his famous experiment which is considered a milestone of physics, because it showed the wave nature of light, also introducing important concepts like diffraction and coherence. Young took a light source illuminating at large distance a screen containing two pinholes and beyond a second photosensitive screen was placed. It is important to place the first screen far enough from the light source, because if we assume that light has a wave nature, in the far-field approximation we can treat a spherical wave, emitted by a point-like source, as a plane wave. So, the two pinholes are invested by a plane wave-front, i.e. by light possessing the same phase. We may think by analogy to a stone thrown into a pond: close to the stone, waves are close circles (spherical waves) and moving further they relax and become more like parallel lines (plane waves).

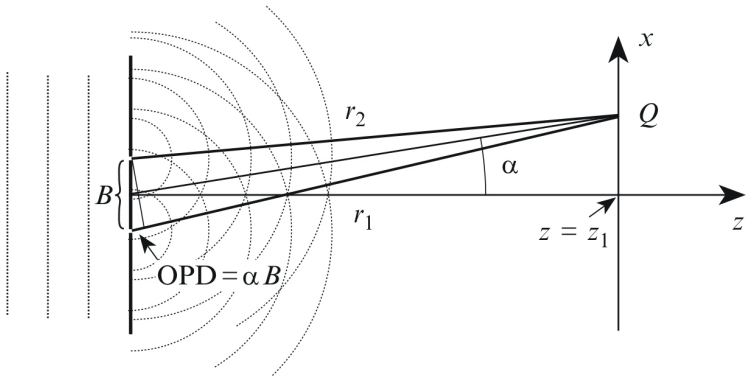

Figure 8: Young experiment geometry [13].

The light passes through the pinholes which behave like two spherical light sources, that, as two stones thrown into a pond may do, generate waves that interfere between them in a very precise and geometric way that draws a so called *fringe pattern* onto the final sensitive screen. The fringe pattern shows zones of constructive interference, where the electric fields of the two waves have the same sign and therefore add up, and zones of destructive interference, where instead have opposite signs and so no intensity is detected on the screen. The expression of intensity the monochromatic spectral intensity results to be:

$$I_{screen}\,(x, \nu) \propto (1 + cos\,(kB\alpha))\,.$$

Studying the maxima and the minima of the fringe pattern, we can retrieve position and spacing between the fringes. The position of the first minimum results:

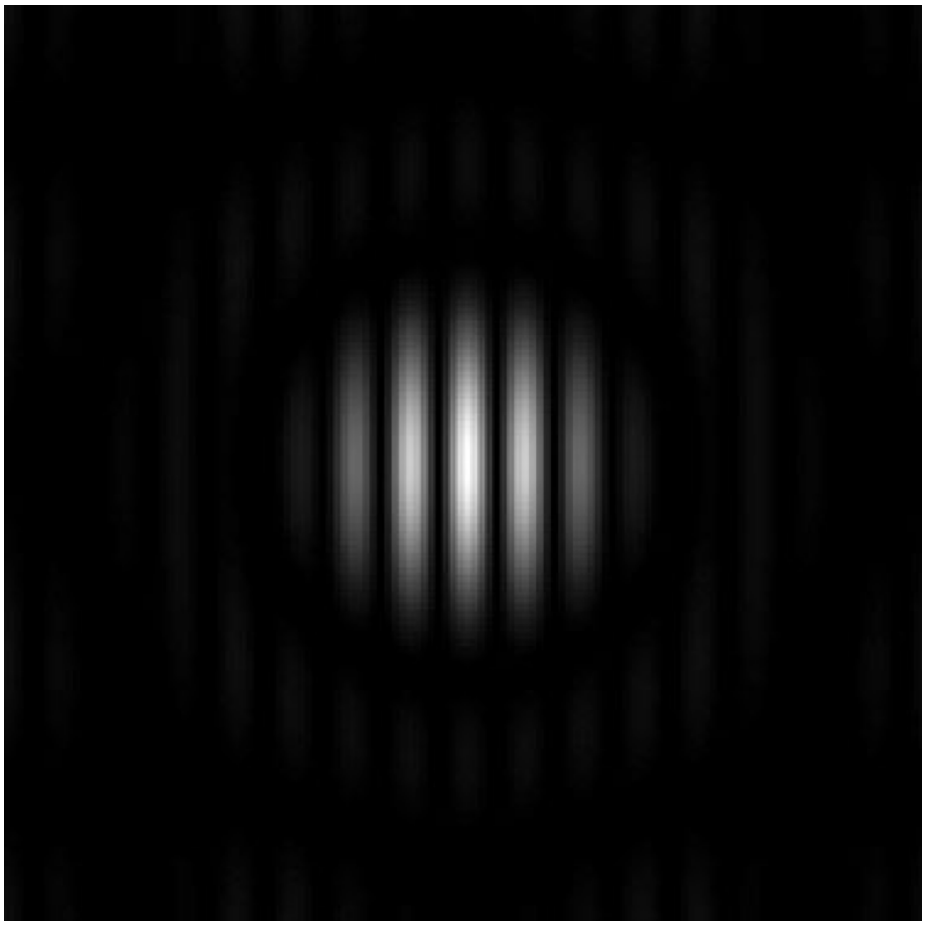

Figure 9: Fringe pattern from a stellar interferometer with two apertures in monochromatic illumination

$$I_{-} \Rightarrow cos(k\alpha B) = -1$$

$$\frac{2\pi}{\lambda}\alpha B = (2n+1)\pi$$

$$\alpha_{min} = \frac{\lambda}{2B}.$$

The position of the fringe pattern depends on the wavelength of the source, that in the monochromatic case is fixed and on the distance B between the pinholes. The overall experiment is ruled by the OPD, which spatially determines the phase difference between the two spherical waves. A difference in the optical path length can be seen

as a difference in the arrival time at the sensitive screen, called *time delay* between the light of the two sources:

$$\tau = \frac{OPD}{c} = \frac{\alpha B}{c}.$$

In the case of a different propagation direction of the original impinging plane wave, the two pinholes are invested by the same wavefront in two distinct instants in time: therefore they will emit the spherical waves with a relative phase difference, function of the angular position of the source. This means that the point of zero phase, where the constructive interference takes place, will be shifted closer to the delayed pinhole, and the overall finge pattern on the screen will translate.
If we repeat the experiment with two light sources emitting in different angolar positions, we would see two overlapped fringe patterns, each one resulting from the interference process of one source with itself. Moreover, between the two patterns there would be a shift due to the different angular position of the two sources, in such a way that the maxima and minima of one source would not have the same positions of the ones of the second source.
This concept is at the basis of the nulling interferometry technique, which provides a way of cancelling the intense starlight during the detection of the faint exoplanet signal. Indeed, an exoplanet and its host star have different angular positions in the sky, so if we use two telescopes for their observation, their wavefronts will reach the telescopes with different OPDs. Therefore, if we implement the interference between the light beams of the two telescopes, we can exploit the shift between the two generated interference fringes to obtain some regions on the detector where the starlight is zero, but the faint signal emitted by the exoplanet is still present.
In an interference process, a key parameter determining how good is this pattern discrimination is the *fringe visibility*, introduced by Michelson:

$$V = \frac{I_{\mathrm{MAX}} - I_{\mathrm{MIN}}}{I_{\mathrm{MAX}} + I_{\mathrm{MIN}}}$$

Note that if $I_{\mathrm{MAX}} = 1$ and $I_{\mathrm{MIN}} = 0$, the contrast of the fringe pattern is $V = 1$, meaning perfect constructive interference in the maxima and totally destructive interference in the minima; such condition sets the perfectly coherent condition of the sources, which means that the ideal cancellation could only be achieved if the wavefronts of the signals were perfectly flat, so that the phase difference at all points would be constant **[10]**.
The light emission of a star or a planet results from the random oscillation of the atoms contained in them. Each point on the surface spreads in all direction light independently of the other, therefore the photons do not have a phase relation among them and this kind of light is by definition *incoherent*. So, in principle stellar light should not lead to any interference pattern, because of the lack of the fundamental hypothesis of coherence. An important theorem allows to overcome this obstacle.

1.3.2 Van Cittert-Zernike theorem

As shown in the Young's experiment, it is necessary a degree of coherence between the sources to lead to an interferometric pattern and this is in contrast with incoherent nature of the celestials bodies. In order to clarify this point and showing that at large distance incoherent sources can be treated as coherent, we should introduce a quantity called *Mutual Coherence Function*, defined as a temporal average:

$$\Gamma = (\boldsymbol{x_1}, \boldsymbol{x_2}, \tau) =< v(\boldsymbol{x_1}, t + \tau)v^*(\boldsymbol{x_2}, t) >$$

The dimensionless quantities v_i are the optical disturbances, proportional to a component of the electric field. Γ determines the degree of correlation between two electric fields in two points ($\boldsymbol{x_1}$ and $\boldsymbol{x_2}$) like two telescopes, in two instants in time (t, t + τ). Note that if we evaluate the quantity at the same point and at the same time, i.e. $\boldsymbol{x_1} = \boldsymbol{x_2}$ and $\tau = 0$, we get the intensity:

$$\Gamma = (\boldsymbol{x}, \boldsymbol{x}, 0) =< v(\boldsymbol{x}, t)v^*(\boldsymbol{x}, t) >= I(\boldsymbol{x}).$$

The pure correlation of the optical disturbances expresses the probability to measure the same value for a pair of points normalizing the mutual correlation function to the intensities:

$$\gamma(\boldsymbol{x_1}, \boldsymbol{x_2}, \tau) = \frac{\Gamma(\boldsymbol{x_1}, \boldsymbol{x_2}, \tau)}{\sqrt{\Gamma(\boldsymbol{x_1}, \boldsymbol{x_1}, 0)\Gamma(\boldsymbol{x_2}, \boldsymbol{x_2}, 0)}}$$

$$0 \leq |\gamma(\boldsymbol{x_1}, \boldsymbol{x_2}, \tau)| \leq 1$$

where $\gamma(\boldsymbol{x_1}, \boldsymbol{x_2}, \tau)$ is called *Second order correlation coefficient* and contains both the spacial and the temporal coherence of the light.
To look at the modification fo the mutual coherence function through space, it is possible to refer to Fourier optics, introducing the *Mutual coherence density function*, that describes the spatial coherence at a frequency ν and it is linked to the mutual coherence function through a Fourier transform:

$$\Gamma(\boldsymbol{x_1}, \boldsymbol{x_2}, \tau) = \int \hat{\Gamma}(\boldsymbol{x_1}, \boldsymbol{x_2}, \nu)e^{-2\pi i\nu\tau}d\nu,$$

$$I(\boldsymbol{x}) = \Gamma(\boldsymbol{x}, \boldsymbol{x}, 0) = \int \hat{\Gamma}(\boldsymbol{x}, \boldsymbol{x}, \nu)d\nu = \int I(\boldsymbol{x}, \nu)d\nu,$$

being $I(\boldsymbol{x}, \nu)$ the spectral intensity. Through these functions it is possible to study spacial and temporal coherence of any kind of light and their propagation in space and through optical systems.
We want to describe spatially incoherent sources, like stars and in this frame the Van Cittert-Zernike theorem takes place. For hypothesis, we consider the shape of the star (or planet) independent of the wavelength observed in its spectrum: in this way we can

define the spectral intensity as the product of the source brightness distribution $I(\boldsymbol{\theta})$ and a source spectrum $G(\nu)$:

$$I(\boldsymbol{\theta}, \nu) = I_b(\boldsymbol{\theta})G(\nu)$$

having defined with $\boldsymbol{\theta}$ the angular position of the celestial object with respect to an observation plane. According to the specific system faced in stellar interferometry, some fundamental hypothesis simplify drastically the discussion:

1. Incoherent sources;
2. Fresnel approximation $\Rightarrow \theta$ is very small;
3. Quasi-monochromatic approximation $\Rightarrow G(\nu)$ is narrow $\Delta\nu \ll \nu_0$; the observed time differences are smaller than the coherence time $\tau \ll \frac{1}{\Delta\nu} \Rightarrow OPD \ll l_c$.

Hypothesis (1) allows to write the mutual coherence function in the plane of observation as function of the coordinate difference only, whereas a point-like source and a the narrow spectral band (2+3) assure the invariance of the Fourier transform over $\Delta\nu$ and the possibility to evaluate it at the average frequency ν_0 and wavenumber k_0, obtaining:

$$\Gamma_{qm}(\boldsymbol{x_1} - \boldsymbol{x_2}, 0) = \int I_b(\boldsymbol{\theta}) e^{-ik_0(\boldsymbol{x_1}-\boldsymbol{x_2})\cdot\boldsymbol{\theta}} d\boldsymbol{\theta}.$$

The expression represents the *Van Cittert-Zernike theorem* and states that the spacial coherence at $\tau = 0$ in the plane of observation is the Fourier transform of the brightness intensity distribution and it depends on the shape of the source. Normalizing we can obtain the degree of coherence $\gamma(\tau = 0)$, called complex *Visibility function*:

$$\mu_{\nu_0}(\boldsymbol{x_1} - \boldsymbol{x_2}) = \frac{\Gamma_{qm}(\boldsymbol{x_1} - \boldsymbol{x_2}, 0)}{\sqrt{I(\boldsymbol{x_1})I(\boldsymbol{x_2})}} = \frac{\int I_b(\boldsymbol{\theta}) e^{-ik_0(\boldsymbol{x_1}-\boldsymbol{x_2})\cdot\boldsymbol{\theta}} d\boldsymbol{\theta}}{\int I_b(\boldsymbol{\theta}) d\boldsymbol{\theta}},$$

$$0 \leq |\mu_{\nu_0}(\boldsymbol{x_1} - \boldsymbol{x_2})| \leq 1$$

$$\mu_{\nu_0}(0) = 1.$$

The visibility function owns a phase $\phi_{\nu_0}(\boldsymbol{x_1} - \boldsymbol{x_2})$; in order to better grasp its meaning we can apply the theorem to the Young's experiment, where the pinholes plays the role of the two telescope being $\boldsymbol{x_1} - \boldsymbol{x_2} = \mathbf{B}$, called baseline. The spectral intensity onto sensitive screen results to be:

$$I(\boldsymbol{\alpha}, \nu) \propto G(\nu)(1 + |\mu_\nu(\mathbf{B})| cos(\phi_\nu(B) - k\boldsymbol{\alpha} \cdot \mathbf{B})).$$

The modulus of the visibility plays the role of a damping factor, therefore is strictly related to the contrast of the fringes, whereas the phase at the baseline shifts the overall pattern. In every kind of nulling interferometry the aim is to set the phase $\phi_S(\mathbf{B})$ of a

star equal to π, in order to evaluate the intensity into a minimum. If a planets orbits a star, it will occupy a different angular position and so the phase of its visibility shall be different, avoiding to cancelling.
The *Van Cittert-Zernike theorem* shows that the correlation of the complex amplitudes is proportional to the Fourier transform of the object distribution at a spacial frequency: changing the baseline of the apertures the Fourier transform can be obtained at a large number of frequencies, allowing to reconstruct the object image **[32]**. The Young experiment is the extreme case where the intensity distribution can be expressed through a delta of Dirac (apart normalization) and being the Fourier transform of such distribution a plane wave, we obtain a simple and intuitive model.

1.3.3 Stellar nulling interferometry

The cancellation of the unwanted light makes it possible to achieve the best contrast reachable among all spectrographic techniques, because the discrimination is independent of the absolute brightness of the sources. This condition is particularly interesting in the research of an exoplanet, which can be till 10^{10} times fainter than its parent star **[1]**. The mathematical description of a nulling interferometer implementation is independent of the setup involved: both bulk optics and integrated interferometers rely on systems capable of combining (at least) two beam and a delay line. We consider two telescopes, which collect the light from the sky into two apertures, as shown in Fig. 10. On the basis of the precedent discussion, we can consider both star and planet two point-like sources, therefore their brightness distribution can be simplified with a delta function and being the Fourier transform of a delta function a plane wave, we express the star and planet light as plane waves.

$$\begin{pmatrix} E_{Telescope1} \\ E_{Telescope2} \end{pmatrix} = \begin{pmatrix} E_{Star1} + E_{Planet1} \\ E_{Star2} + E_{Planet2} \end{pmatrix},$$

$$\begin{pmatrix} T_1 \\ T_2 \end{pmatrix} = \begin{pmatrix} S\,e^{i\theta_1} + Pe^{i\varphi_1} \\ S\,e^{\theta_2} + Pe^{i\varphi_2} \end{pmatrix},$$

being θ_i and φ_i respectively the phases of the star and planet at telescopes i, and S and P the amplitudes of the electric fields or optical disturbances. To one telescope, e.g. telescope 2, it is imposed a phase delay $\Delta\phi$, through a control of the optical path difference. After the phase shift, the two beams are combined into a beam splitter, which carries the proper interferometric process. The interference is carried out efficiently if from one output the star does not exit. A balanced beam splitter, i.e. a beam splitter capable to distribute the incoming light 50:50, is mathematically expressed by a 2x2 complex and unitary matrix:

$$\begin{pmatrix} Out_1 \\ Out_2 \end{pmatrix} = \frac{1}{\sqrt{2}} \begin{bmatrix} 1 & i \\ i & 1 \end{bmatrix} \begin{pmatrix} S\,e^{i\theta_1} + Pe^{i\varphi_1} \\ (S\,e^{i\theta_2} + Pe^{i\varphi_2})\,e^{i\Delta\phi} \end{pmatrix}$$

If we want to null the star contribution in output 1, we have to find a condition of the imposed $\Delta\phi$ to do that.

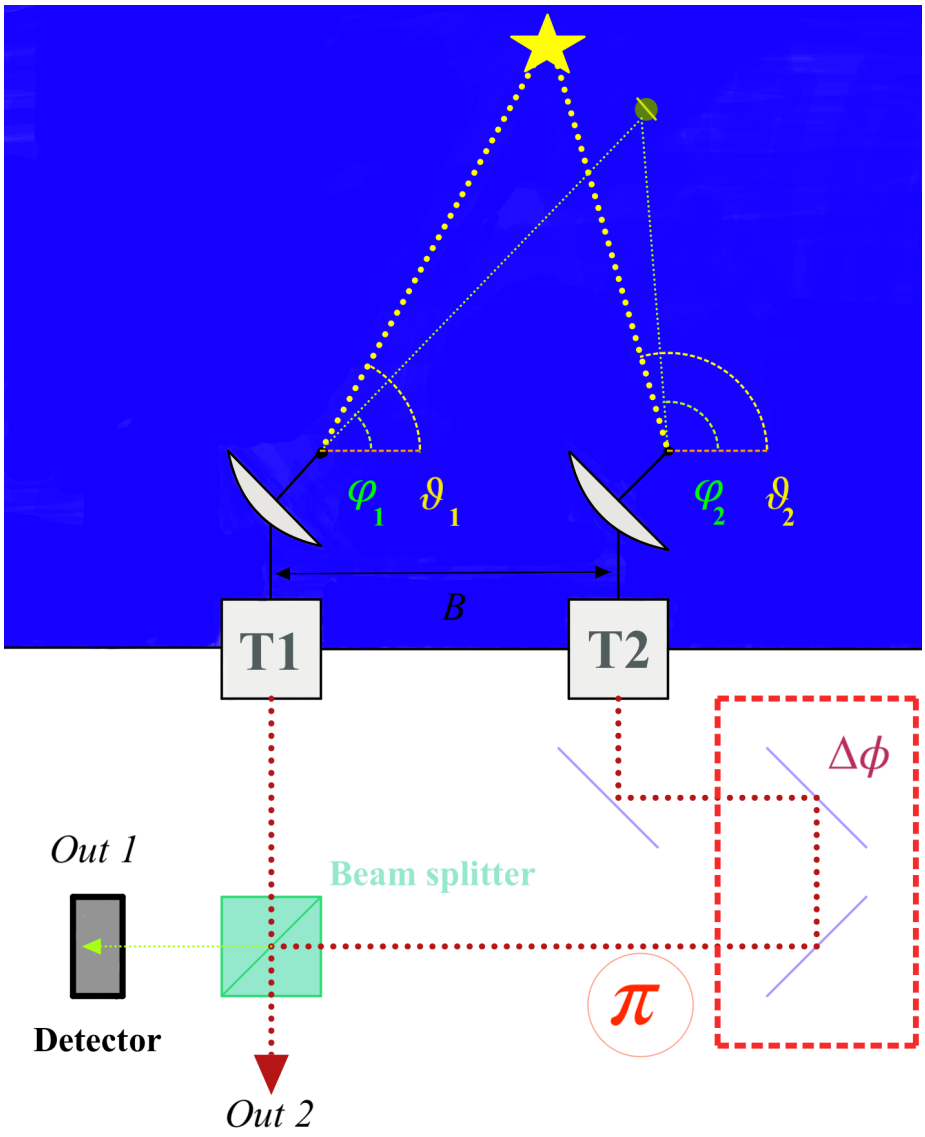

Figure 10: Nulling interferometer setup. Two telescopes collect light from a star and a planet: in one arm is imposed a phase control $\Delta\phi$ so that the starlight visibility pattern is π-shifted, setting the dark fringe on-axis allowing the planet detection only.

$$O_1 = \frac{1}{\sqrt{2}}\left[S\,e^{i\theta_1} + Pe^{i\varphi_1} + ie^{i\Delta\phi}\left(S\,e^{i\theta_2} + Pe^{i\varphi_2}\right)\right],$$

being $i = e^{\frac{i\pi}{2}}$ and gathering the amplitudes of the celestial bodies, we get:

$$O_1 = \frac{1}{\sqrt{2}}\left\{S\,e^{i\theta_1}\left[1 + e^{i(\Delta\phi+\Delta\theta+\frac{\pi}{2})}\right] + Pe^{i\varphi_1}\left[1 + e^{i(\Delta\phi+\Delta\varphi+\frac{\pi}{2})}\right]\right\}$$

where $\Delta\theta = \theta_2 - \theta_1$ and $\Delta\varphi = \varphi_2 - \varphi_1$. Till now, we have dealt with fields, but what we measure on a detector is an intensity value. Therefore, we must take the squared modulus of the output fields, after having called:

$$\alpha = \Delta\phi + \Delta\theta + \frac{\pi}{2}$$

$$\beta = \Delta\phi + \Delta\varphi + \frac{\pi}{2}$$

resulting:

$$I_{out1} = \frac{1}{2}\left\{|S|^2\left|e^{i\theta_1}\right|^2\left|1 + e^{i\alpha}\right|^2 + |P|^2\left|e^{i\varphi_1}\right|^2\left|1 + e^{i\beta}\right|^2\right\}.$$

Note *It is important to underline that taking the modulus square of the sum of two complex numbers leads to another factor:*

$$z_A = Ae^{i\eta_A}, z_B = Be^{i\eta_B}$$

$$|z_A + z_B|^2 = |z_A|^2 + |z_B|^2 + 2cos(\eta_B - \eta_A)$$

for two incoherent sources, the quantity $(\eta_B - \eta_A)$ *is not a constant, but varies very rapidly in time. The measurement carried out by a detector is not as fast as these oscillation: the sensor averages the values of the intensity and being* $< cos(\eta_B - \eta_A) >= 0$*, this term does not appear in the expression of the intensity.*
The squared modulus cancels some global phases terms, so the intensity at one output of the beam splitter results:

$$I_{out1} = \frac{1}{2}\left\{|S|^2\left|1 + e^{i\alpha}\right|^2 + |P|^2\left|1 + e^{i\beta}\right|^2\right\}$$

In order to null the light contribution of the star from the output, it must be:

$$\alpha = \pi,$$

that implies:

$$\Delta\phi + \Delta\theta + \frac{\pi}{2} = \pi,$$

$$\Delta\phi = \frac{\pi}{2} - \Delta\theta.$$

This is the condition that the interferometer sets through the phase control, which does not affect the planet:

$$\beta = \frac{\pi}{2} - \Delta\theta + \Delta\varphi + \frac{\pi}{2},$$

$$\beta = \pi - \Delta\theta + \Delta\varphi.$$

The planet would be nulled if $\beta = \pi$, that means:

$$\Delta\varphi = \Delta\theta,$$

but this condition is true only if the star and the planet occupy the same position in the sky and, because they are two distinct celestial objects owning to different angular positions, it will always be $\Delta\varphi \neq \Delta\theta$.
In 1978 Bracewell proposed this method to increase the spacial resolution of detectors. He took into account the system Sun-Jupiter seen from a distance of 33 ly and showed that in the optimal condition, i.e. total null of the star and a maximum of interference for the planet, the power ratio $P_{Jupiter}/P_{Sun}$ would exceed 80 **[14]**.
The basic performance parameter for a nulling interferometer is the *nulling ratio* **[15]**:

$$nl(\lambda, \tau) = \frac{I_{min}}{I_{max}},$$

where I_{min} is the intensity of the on-axis dark fringe, resulted from the π-shift, and I_{max} the off-axis bright one. The nulling ratio strictly depends on the wavelength and on the integration time τ. An instrumentation is demanded to provide a nulling ratio of $\sim 10^{-5}$ and a high level of stability, i.e. longer exposure times should not reduce the contrast.
The most convenient band region to carry out the interferometric process is the IR: it offers an advantage over visible light of 10^5 as regards the ratio of power received from star and planet **[14]**, being in the thermal infrared the planet's emission strongest and the star's one relatively weaker **[19]**. Moreover, this spectral region is remarkably informative, as it could contain absorption features of water (under 8 μm), ozone (9.6 μm), and carbon dioxide (15 μm) **[16]**. A good device must also discriminate the signal planet from the exozodiacal dust, whose quantity around other solar systems is poorly known **[16,17]**.

1.3.4 Bulk nulling interferometers implementations

The IR radiation collected by the two telescopes in the nulling configuration has to be brought to a common location where the interference can take place, where angular position of the constructive interference is set by the baseline length of the interferometer and by the orientation of the array **[14, 21]**. The imposed phase delay must be

achromatic, i.e. the position of the central wideband null has to be independent of the wavelength **[20,14]**.
In order to achieve a high value of the extinction ratio, the combined wavefronts have to be very similar in amplitude, phase and polarization distribution: different optical paths introduce differential defects of the wavefronts, decreasing the quality of the null **[21]**. An interference carried out with no OPD assures fully achromaticity **[20]**. Bulk nulling interferometers face these issue involving several optical elements and spacial filters, like pinholes positioned in at the focal planes of a lens, eliminating high spacial frequencies **[21]**. A π-shift can also be realized through a control of the geometric phase, because the implementation of half-wave plates and polarizers in succession can lead to a cyclic change in the state of polarization causing an achromatic phase shift **[20]**. However, solutions involving several optical elements have the problem to induce high transmission losses in the materials, making more appealing reflection configuration **[14]**.

Figure 11: On the right, Twin W.M. Keck Telescopes on Mauna Kea summit, at the height of 4145 m. The absence of nearby mountains, the thermal stability of the Pacific Ocean and very low light pollution make this site one of the best seeing site on Earth **[2]**.

In this frame, for *ground-based telescopes* a major problem is represented by atmospherical turbulence, which distorts the wave-front of starlight. Therefore, ground-based telescopes are very large systems, often involving segmented mirrors to bring light into a focus **[1]**. The W.M. Keck observatory in Mauna Kea (Hawaii) gathers two telescopes owing an aperture of 10 m with a baseline of 85 m, a weight of 300 tons and a system of four outriggers telescopes **[17]**. It is equipped with an *Adaptive Optics* system (AO) of extraordinary technology: a primary mirror subdivided into 36 hexagonal segments, whose AO technology allow them to work in concert as a single piece of reflective glass in order to correct the wave-front distortion induced by the

Earth's atmosphere. The control of these components is extremely precise, showing an accuracy at nanometric scale, thanks to the deformable mirror which can change shape 2000 times in a second. This assures the clearness of the images, going from a detail map of Uranus's atmosphere to the detection of the darkest galaxy known up to know, from gravitational waves to supermassive black holes **[22]**.
Space-based telescopes instead show smaller dimensions and are not constrained by the atmospherical turbulence issues. They are composed in general by three or more telescopes whose aperture is on the meter scale (0.4 - 1.5 m) and can implement different functions, like nulling and visibility measurements modes; moreover if composed by distinct satellites have the great advantage to range the space baseline till several hundreds of meters, increasing angular resolution **[16,23]**. However, this kind of systems is more sensitive to instrumentation temperature, that due to the black body emission is the main noise contributor at longer wavelengths, limiting drastically the number of detected exoplanets **[30]**.

1.4 Integrated optics

An alternative approach to the bulk implementation of a nulling interferometer is exploiting optical integrated devices, i.e. compact and stable systems capable of confining and controlling light, which can operate both in the IR and optical regimes. Integrated optics is applied in many fields of physics, from astophotonics **[47]**, microfluidics **[48]**, quantum communication **[49]** and computing **[50]**.
Astronomers have come to recognize the benefits of integrated photonics, often in combination with optical systems to solve the major challenges of detection **[1]**. In fact, in parallel to nulling interferometers, it is possible to create devices like photonic lanterns **[51]**, pupil remappers **[52]** and microspectrographs **[53]**: one of the greatest advantages is the possibility to implement several functions within the same chip.

1.4.1 Quantum analogy

The principle at the basis of the light confinement into a dielectric material is the creation of region with an higher refractive index with respect to the surrounding. The modified paths are called *waveguides*, which can describe any geometry bringing light between different points of the device **[24]**.

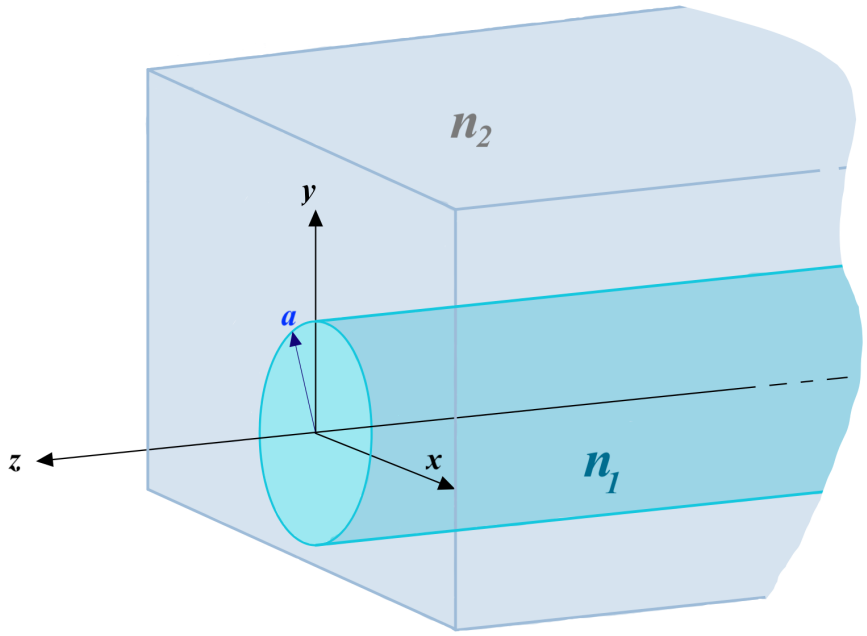

Figure 12: Waveguide layout. The region with higher refractive index n_1 is called *core*, whereas n_2 is defined as *cladding*.

The Helmholtz equation describes the spacial propagation of a monochromatic electromagnetic wave into a dielectric material with a space-dependent index profile $n(x, y, z)$:

$$\nabla^2 E + \frac{\omega^2}{c^2} n(x, y, z) E = 0,$$

being E the scalar electric field **[24]**. If the refractive index profile can be considered a smoothly varying function of the propagation direction z, i.e. the variations take place over a region much wider than λ, a solution for the electric field can be written as:

$$E = E_0(x, y, z) e^{i(\frac{2\pi}{\lambda} n_{eff})z},$$

where in case of a waveguide $n_2 < n_{eff} < n_1$ is the effective refractive index and depends on all its parameters. Substituting this expression in the Helmholtz equation and considering E_0 a slowly varying function of the propagation direction z, we obtain:

$$i\lambda\!\!\!^{-} \frac{\partial E}{\partial z} = -\frac{\lambda\!\!\!^{-2}}{2n_{eff}} \nabla^2_{x,y} E + N(x, y, z) E,$$

where $\lambda\!\!\!^{-} = \frac{\lambda}{2\pi}$ and $N = \frac{n_{eff} - n(x,y,z)}{2n_{eff}}$. The expression resembles the time dependent Schrödinger equation for a quantum particle in a potential well, holding the parallelisms:

$$z \Leftrightarrow t, \qquad \lambda\!\!\!^{-} \Leftrightarrow \hbar, \qquad n_{eff} \Leftrightarrow m, \qquad N(x, y, z) \Leftrightarrow V(x, y, z).$$

The role of the eigenvalues of the energy is played in this case by the propagation constant $\beta_{m,n} = k_0 n_{eff}$, where m, n label the spacial mode of the field: to each propagation constant corresponds a transverse distribution of the electric field extending outside the core region of the waveguide with an exponentially decreasing tails **[24]**. If two waveguides are kept close enough, it is possible to exchange power between them due to overlapping of these tails, as a tunneling effect for quantum particles: this phenomenon is called *evanescent coupling*. It is at basis of the working principle of a *directional coupler*, an optical integrated unity that can mix light contribution and performe also interference between two input light beams. Actions like the phase control can be carried out exploiting the potential $N(x, y, z)$, e.g. thanks to the thermo-optical effect induced by phase-shifters.

In a lot of applications, first of all astrophotonics, it is crucial to work with *single mode* waveguides, because they propagate only the fundamental mode for each wavelength, providing an intrinsic spatial filtering that is capable to clean the signal affected by atmospheric turbulence **[1]**. The transverse amplitude and phase of the propagated wave is uniquely determined by the opto-geometrical parameters of the guiding structure, independently of the input conditions **[35]**.The modal filtering action is set by the cutoff frequency:

$$\omega_{cutoff} = \frac{2\pi}{\lambda} a \sqrt{n_1^2 - n_2^2},$$

where a is the core radius. The single mode regime lies for $\omega_{cutoff} < 2.4$ **[35]**.

1.4.2 Directional coupler

The directional coupler is a four ports device composed of two waveguides brought very close, in order to obtain a power transfer between them by exploiting the evanescent coupling.

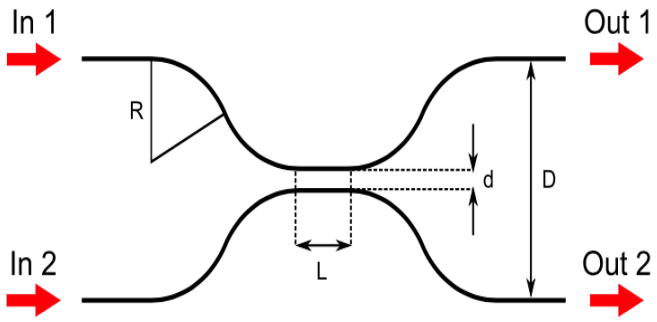

Figure 13: Directional coupler layout. R: curvature radius, L: interaction length, d: coupling distance **[24]**.

Two bending waveguides get closer and closer, so an overlap of tails of the guided modes gradually occurs and the modes of light are no more independent. The key fabrication parameters governing the induced power transfer are three coefficient generating a periodic behavior of the splitting ratio, defined as:

$$SR(\lambda) = \frac{P_{bar}}{P_{cross} + P_{bar}} = \sigma^2(\lambda) sin^2\left(\frac{\kappa(\lambda)}{\sigma(\lambda)} L + \phi(\lambda, R)\right),$$

where P_{bar} is the power output of the injection waveguide, whereas P_{cross} the one at the cross coupled waveguide. The expression is ruled by:

- L : *interaction length*, straight paths region where the guides get closer;
- κ : *coupling coefficient*, that describes the strength of the interaction between the waveguides in the coupling region of length L, and is proportional to the overlap integral of the two guided modes **[24]**:

$$\kappa \propto \iint E_1(x, y) E_2(x, y) dx dy \ ;$$

- ϕ : *bending phase* taking into account the initial coupling associated to the curvature and to the progressive approaching of the waveguides till the parallel coupling region;

- σ : *dephasing* term which reduces the maximum cross-coupling ratio according to the degree of waveguides asymmetry, expressed by the difference between the two propagation constants $\Delta\beta(\lambda)$ **[33]**, according to the relation:

$$\sigma = \left[1 + \left(\frac{\Delta\beta}{2\kappa}\right)^2\right]^{-1/2}.$$

It is worth noting that all the presented parameters show a strong dependence on the wavelength of light, so in general the splitting ratio of a directional coupler will be chromatic. This can be a problem in astrophotonic, since for obtaining a reliable measure, some bandpass filters should be used, further reducing the already faint available signal.
These factors are varied with the task to reach the 50:50 splitting condition in the most precise and broadband way **[25]**. Their optimization plays in concert with the geometrical parameters, the distance d between them and the curvature radius R. Smaller d-values lead to a stronger coupling, thus accelerating the power transfer and reducing the period of the splitting ratio; but at the same time causes a premature coupling in the bending region **[25]**.
We can define a further term, expressing the *effective coupling coefficient*:

$$F(\lambda) = \frac{\kappa(\lambda)}{\sigma(\lambda)}.$$

In a matrix formalism, the directional coupler can be expressed in a general way through a 2×2 unitary matrix U, which describes the operation of an arbitrary lossless device acting on two optical modes, is written as **[26]**:

$$\hat{U} = e^{i\phi}\begin{bmatrix} r & it \\ it^* & r^* \end{bmatrix},$$

where $r, t \in \mathbb{C} : |r|^2 + |t|^2 = 1$, and ϕ is a global phase term.
Due to the fabrication process, the waveguides show a defined birifringence axis: during the propagation to each mode correspond two different polarization modes (e.g. H and V) which do not exchange power within the device **[26]**. In real applications, imperfections in the core shape and refractive index homogeneity induces slightly different propagation constants, resulting in random cross-talks between the modes **[35]**. According to the birifringence of each waveguide $b_i = \frac{\lambda}{2\pi}(\beta_{i,H} - \beta_{i,V})$, a path-dependent rotation of the polarization state occurs, which however does not affect the splitting ratio **[26]**.

1.4.3 Advantages

The great and intrinsic advantages of integrated circuits, especially for astrophotonic applications are:

1. Intrinsic modal filtering, proper of waveguides and fibers which are capable to impose the fundamental propagation mode not affected by noise, especially the atmospheric one **[1,31]**;
2. Robustness and high stability to temperature and vibration, thanks to the monolithic structure which do not need alignment or calibration **[25]**;
3. Multitasking operation, the capability to inscribe several components with different functions in the same device (e.g. a remapper) **[1,31]**;
4. Lightness and small dimensions, ideal for space-operations **[35]**;
5. Design in 3 dimensions, increasing the device possible functions **[36]**;
6. Great versatility due to the different usable materials and geometry degrees of freedom;
7. Compatibility with communication technologies well established.

1.4.4 Integrated optics nulling interferometers

In order to achieve a high extinction ratio, a nulling integrated interferometer has to own an accurate level of symmetry in terms of optical paths, polarization, amplitude and chromatism **[34]**. In the selection of the substrate material, the transparency range is fundamental: chemically stable and non-toxic glasses, like fused silica, are well established, but the IR-absorption bands must be carefully taken into account . Thermal and mechanical stability are necessary, as well as the compatibility with cryogenics operations **[35]**. We will focus our attention on devices similar to the one presented in this work, but we have to remember that astrophotonics allow to develop a huge number of different devices that can address the same task following different ways. An integrated 2D-nulling interferometer has the layout showed in Fig.14.
The idea at the basis of nulling interferometry is to filter out the signal of the star and to isolate the one of a planet: in bulk setups the interferometric process is carried out in a beam splitter, whereas the phase control by a modification of the optical path. In case of an integrated interferometer, the beam splitter is replaced by a directional coupler and the phase control is performed by thermal phase shifters. In this frame, we can say that the interferometry in the integrated case is carried out internally a single device.
Another important requirement for integrated interferometers is losses minimization: polarization and wavelength dependent losses are a limiting factor in performances, because constrain to use optical elements to clean the beam before injection, reducing further the signal.
An example of these problem can been seen in Fig.15. The behavior of the splitting ratio shows the progressing chromatic dispersion with increasing L, leading to a less broadband device. One of the important aims of this work was to obtain a broadband

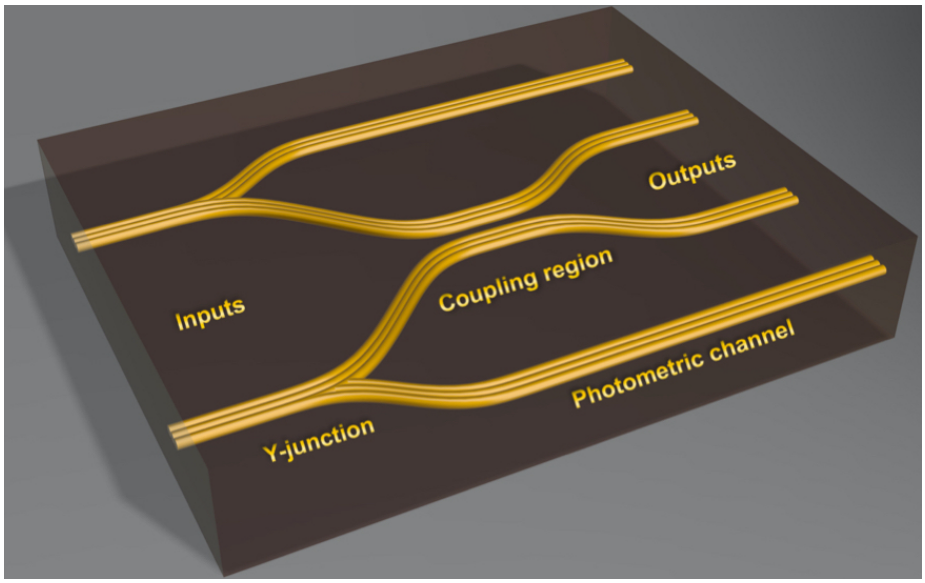

Figure 14: Layout of the nulling integrated interferometer presented in **[25]**.

behavior as wide as possible, because for a device of this kind it means a greater detecting window.
Studying the fundamental components of an integrated circuit has lead to fabricate a concrete device known as GLINT, which in 2020 was recognized as the first on-sky demonstration of an integrated nulling interferometer **[10]**. This devices was tested in the Subaru Telescope (Hawaii) demonstrating the huge potential of this technology and design. It was possible to measure with milliarcsecond accuracy the angular diameter of stars via null-depth measurements, achieving a precision of null-depth on sky of 10^{-4}.
The operation wavelength was $\lambda = 1.6$ μm and the bandwidth $\Delta\lambda = 50$ nm, the interaction length was $L = 3.75$ mm and the interaction length $d = 10$ μm, resulting in a monolithic chip in boroaluminosilicate glass of 41 mm in length by 10 mm in width and a thickness of 0.7 mm. The major dimensions of the device were so high because it was necessary to introduce a displacement between the inputs and the interferometer, in order to avoid undesired uncoupled light contribution **[10]**.

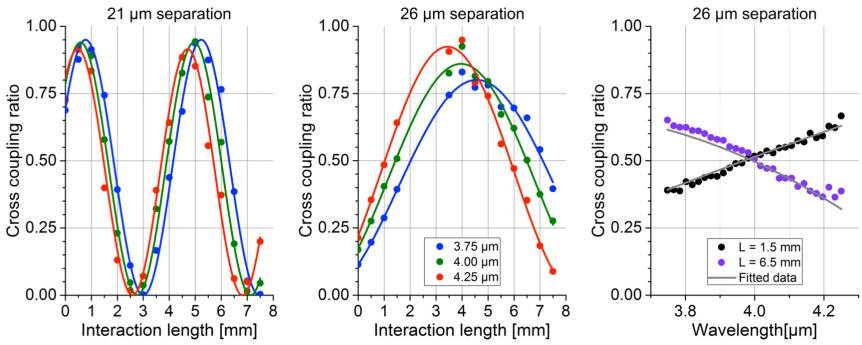

Figure 15: Splitting ratio in function of the incoming wavelength for two different interaction lengths for a nulling interferometer fabricated in chalcogenide glass. The device has been realized with FLM, in a wavelength range 3.6 µm $< \lambda <$ 4.2 µm. showing propagation losses $< 0.22 \pm 0.02$ dB cm^{-1} and polarization dependent losses <0.1 dB cm^{-1} **[25]**.

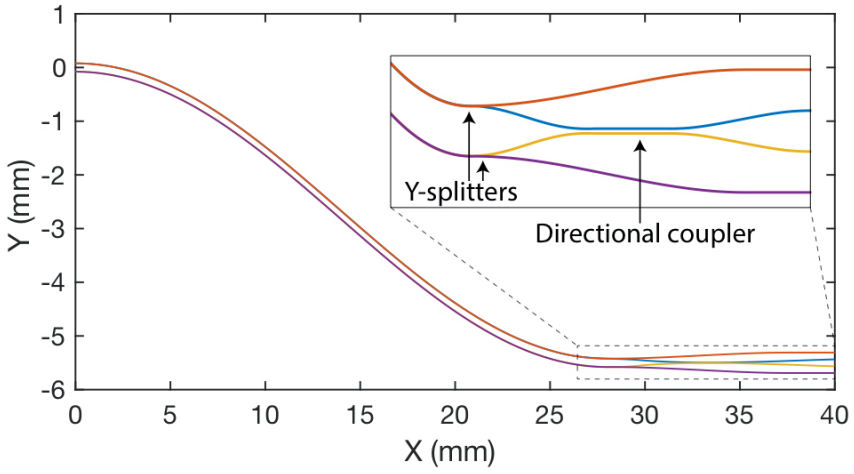

Figure 16: Top-down view of the GLINT photonic circuit **[10]**.

2 Femtosecond Laser Micromachining

2.1 Overview

Among the techniques allowing the fabrication of integrated photonic circuits, femtosecond laser micromachining is able to provide high quality waveguides with low losses and high compatibility with optical fibers **[36]** .
Femtosecond lasers are capable of providing high-energy-density pulses which can be focalized into transparent materials to induce a permanent increase of the refractive index **[38]**. Since bulk glasses do not have any linear absorption at the wavelength of the femtosecond laser, a non-linear absorption process is required **[37]**. By focusing the laser beam beam through objectives, multiphoton photochemical reactions can occur, inducing the writing of transparent but visible round-elliptical damage lines inside those materials **[38]**. The non-linear nature of the required absorption process confines the modification of the refractive index only to the focal volume **[37]**: this allow to scan regions by the focal point realizing complex and three-dimensional patterns in the glass **[38]**.

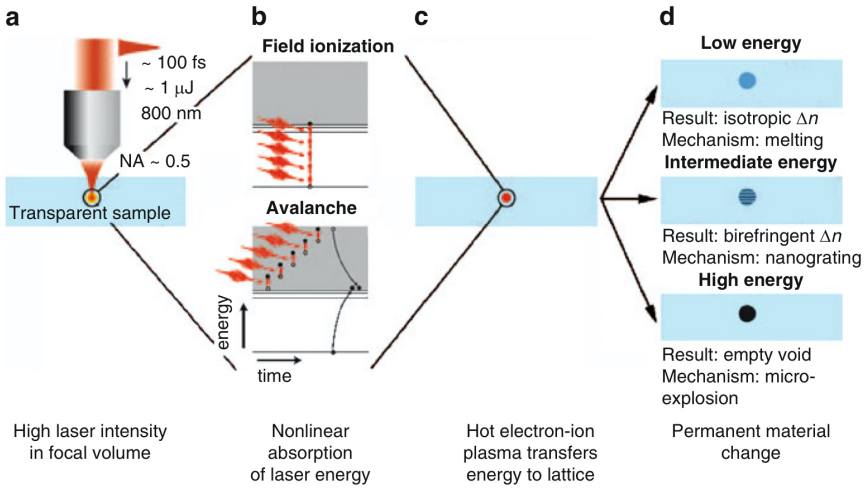

Figure 1: Working principle of FLM in a fused silica sample. a) The femtosecond laser is focused below the surface resulting in a high intensity at the focal volume. b) A nonlinear absorption processes leads to an avalanche ionization and the formation of an electron-hole plasma. c) The plasma energy is transferred to the lattice in picosencond time scale. d) Three modification according to the irradiation regime**[36]**.

The index modification in the damaged region is strictly dependent on the radiation dose, reaching till $\Delta n = 0.01 - 0.035$ in pure Ge-doped silica glasses **[38]**. In facts, at the focus of the laser the intensity is high enough to lead to three different modification regimes depending on the laser energy deposited during the irradiation. Considering $NA = 0.6$, $\lambda = 800$ nm and $\tau = 100$ fs **[36]**:

- at low pulse energy (E_p = 100 nJ), the modification is smooth, suitable for writing waveguides for the development of communication circuits **[54]**, quantum devices **[55]** and stellar interferometers **[10]**;
- at higher pulse energy (E_p = 150 − 500 nJ), oriented planar nanostructures are created: they confer to the guide a birifrangent behavior, so the response of the guide to a light input is strictly dependent on its polarization component. Their origin is linked to an interference process between the laser electric field and the electron plasma formed during writing **[39]**. The planes are more subjected to the attack of strong acids, so *preferential chemical etching* can be employed to carve channels into the glass, opening the way to the research field of micro-fluidics **[56]**.
- a most severe regime (E_p > 500 nJ) causes plasma micro-explosions, whose pressure in the focal volume exceeds the Young's modulus, digging vacuum tunnels surrounded by a region of higher refractive index. These voids are useful for quantum memories **[57]** or photonic bandgap materials **[58]**.

The absorption process is independent on the material, therefore several optical devices can be fabricated in a wide range of different substrates **[37]**.

2.2 Laser-matter interaction

2.2.1 Glass

Glasses are transparent to visible and to most of infrared light; only a few portion of the energy of an incoming light beam is effectively absorbed under the form of heat, the rest is transmitted and only a small part is reflected at the interface. These materials are everything but cristalline solids: glasses are amorphous systems because do not display a regular lattice where it is possible to identify precise translation geometries and so draw a clear band structure through Bloch's theorem, which rely on the presence of a periodic potential **[40]**.
Furthermore, glasses should be considered solid neither, but *undercooled liquids* whose proprieties are well described by modeling them as fluids with a huge viscosity, whose dependence on temperature is capable to induce in standard conditions enormous relaxation times in the order of millions of years.
A proper and deep description of glasses is hard to achieve, because the theory of particles behavior in random potentials is not complete. However, we could develop the fluidic parallelism and consider a Fermi-liquid model applied to a glass, obtaining a *Fermi-glass*. Since the potential is random, a glass band is split into *localized* and *extended states*: the former result from the absence of a long-range correlation of the electronic wavefunction, permitting only a local description of electrons fixed at the Fermi Energy **[40, 41]**. The trapped electrons fill a continuous energy range of localized states up to a *mobility edge*, where the range of the correlation become infinite and extended states take place. Critical energies E_c separate localize states from extended regions, whose position are function of the degree of disorder of the material **[40]**. We can change it or the density of state varying the glass composition **[41]**. For

practical purposes, we consider a valence band as the collection of the localized states at the Fermi Energy, the conduction band as extend states and the average of the critical energies as the bandgap. The thermodynamical proprieties of a glass as specific heat and Pauli paramagnetism can be explained with the Sommerfeld model of a metal, but with an important difference: whereas for metal a temperature decrease improve the electronic conductivity, in glasses does not, due to the the trapped condition, which imposes a minimum value for the electronic conductivity **[41]**.

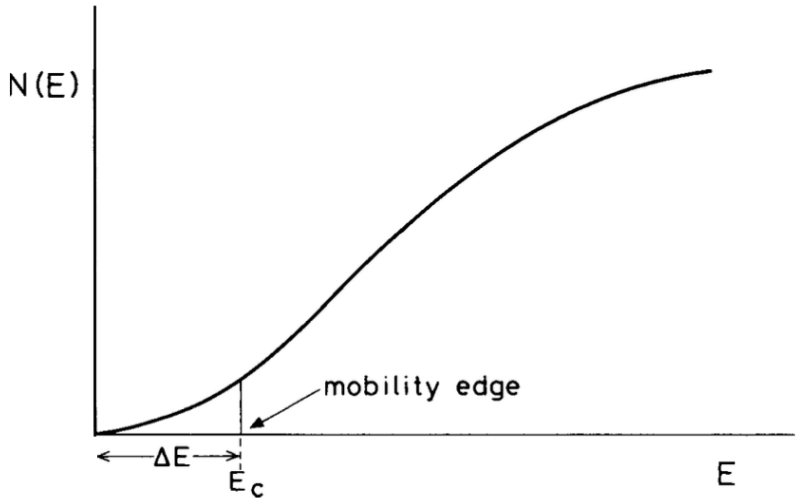

Figure 2: The density of states in the conduction band of a non-crystalline material, showing the mobility edge Ec separated by an energy ΔE from the band edge **[41]**.

2.2.2 Laser

The laser must provide high energy pulses, so that short time duration are required. This feature is addressed by femtosecond lasers, which generate pulses up to hundreds of mJ, with a time duration of some fs and a repetition rate ranging from some Hz to THz **[42]**. The laser beam is focalized through microscope objectives into the material, reaching peak intensities on the order 10 TW cm^{-2} **[36]**. The resulting non-linear absorption occurs thanks to two main processes: the *tunneling effect* and the *multi-photon absorption*, which in concert can promote an *avalanche ionization* in the material. It is important to underline that this last process is a linear, therefore is the major responsible of the induced index modification **[37]**. Then the energy of the generated electron-hole plasma is transferred to the lattice in the order of picoseconds, leading to cooling down in diffusive times.

2.2.3 Tunneling effect

In case of tunneling effect, we consider the promotion of an electron from the valence band, a collection of localized states, to the conduction band seen as a set of free traveling electron affected by the potential of the surrounding portion of the lattice. The valence electrons have no sufficient energy to go to the upper band in standard condition, so the probability of tunneling is lower the greater the bandgap is. However, if a strong electric field is acting, a distortion of the bands occurs, making the relative distance between them rapidly oscillating in time and bringing to favorable situation in which the top of the valence band coincides with the bottom of the conduction one in terms of energy. This lowering of the bandgap increments the tunneling probability, so that an electron can travel to the conduction band without the absorption of photons, but only benefitting form the induced alteration of the band structure. This process is more probable at high field intensities and low frequencies **[36]**, so that $h\nu < E_{gap}$: the high electric field modifies locally the dispersion relation and a linear absorption can occur, with the formation of an hole in the valence band.

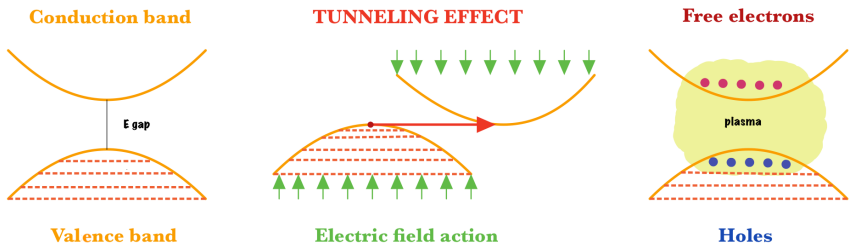

Figure 3: The strong electric field intensity of the laser pulses distorts the band structure reducing the bandgap, making possibile and intra-band transition by tunneling effect and making possible the formation of an electron-hole plasma.

2.2.4 Multi-photon absorption process

Multi-photon absorption competes to tunneling and leads in the same way to a non linear ionization, but in this case the process is more favorable at low intensities and high frequencies and the condition to fulfill is $mh\nu > E_{gap}$ **[36]**. Under these conditions, an electron is able to absorb more photons within a time interval inferior to its thermalization time, determined considering its mean free path **[43]**, so that it can acquire sufficient energy to overcome the energy bandgap, reaching the conduction band and leaving a hole behind.
Tunneling effect and multi-photon absorption can be unified by the Keldish's parameter **[36, 43]**:

$$\gamma = \frac{\nu}{2\pi e}\sqrt{\frac{m_e c n \epsilon_0 E_{gap}}{I}},$$

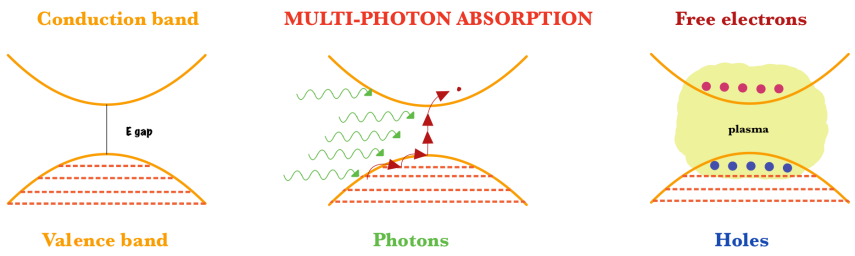

Figure 4: The electrons in the valence band can absorb high frequency photons to overcome the bandgap and forming and electron-hole plasma.

where ν is the laser frequency, e and m_e the electron charge and mass, c and ϵ_0 the speed of light and the permittivity of vacuum, n the linear refractive index, E_{gap} the energy gap and I the intensity at the focus.
For small values of the Keldish parameter, $\gamma \ll 1.5$, the tunneling effect dominates; vice versa, for $\gamma \sim 1.5$, multi-photon absorption is more probable **[36]**. For traditional bulk glasses, a value of γ is around 1, so that the electron-hole plasma formation can be considered as a result of both processes.

2.2.5 Avalanche ionization

The tunnel effect and the multi-photon absorption process lead to the excitation of several electrons into the valence band, where collisions among free electrons can take place. The electrons already present in the conduction band can acquire the photon energy by *linear* absorption to overcome the bottom of the conduction band by an amount superior to the bandgap energy: through collisions this "energy excess" can be transferred to the bound electrons in the valence band, promoting an *avalanche ionization* **[36]**. The linear dependence of the avalanche ionization probability on intensity is the real responsible for the final index modification for the high excitation density achieved **[37]**.
Since the electron excitation occurs in the short pulse duration of some femtoseconds, whereas the time required for an energy transfer between the plasma and the lattice, i.e. the electron-phonon scattering, is around one picosecond, the material modification is confined to the focal volume and it also allows to decouple the plasma formation from the lattice heating process **[37, 36]**.
It is important to underline that in the absence of the linear behavior of the avalanche ionization, the index modification would rely only on the tunneling and the multi-photon absorption, leading to a non linear dependence of the intensity on the energy gap too, so that:

$$E_{gap} = N\hbar\omega$$

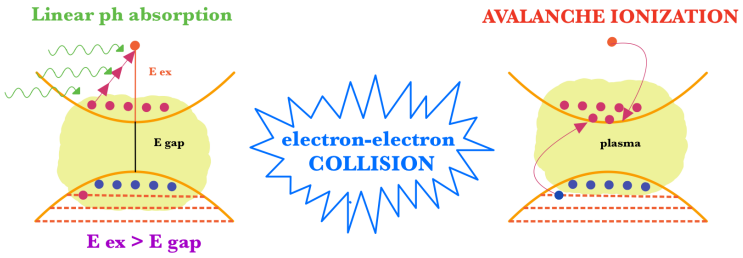

Figure 5: The excited electron in the plasma can linearly acquire the photon energy and transfer it to the bounded electron in the valence band through collisions, promoting an avalanche ionization.

$$I_{modification} = I_{field}^{N}$$

This would imply that depending on the bandgap, hence on the material, the threshold intensity required to achieve an index modification would vary enormously, but thanks to the linear behavior of the avalanche ionization probability this problem does not subsist and very different materials may show only slightly dependences on the fabrication parameters, making FLM extremely versatile **[37]**.

2.2.6 Optical breakdown

Thanks to the avalanche ionization, the plasma number density grows very fast until the frequency of the laser approaches the plasma frequency: at this critical density the plasma dynamics changes, leading to a strongly absorbing behavior that favors the light transmission and the consequently energy absorption by free carriers of the remaining part of the incoming femtosecond pulse **[36, 37]**.

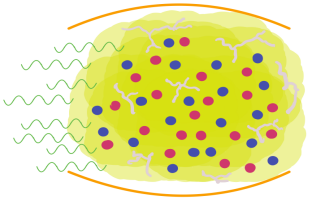

Figure 6: Optical breakdown: the plasma number density is huge and the plasma is absorbing. In picoseconds the energy is transmitted to the lattice, inducing damage.

If we consider a plasma without an external magnetic field, where the main contribution to the plasma frequency is given by the electrons, we have:

$$\omega_e = \sqrt{\frac{n_e e^2}{\epsilon_0 m_e}},$$

which at the critical density n_{crit} equals the frequency of the laser, $\omega_e = \frac{\nu}{2\pi}$:

$$n_{crit} = \frac{4\pi\epsilon_0 m_e \omega^2}{e^2}.$$

For a laser frequency in the infrared $\nu = 10^{15}$ Hz, the critical density would be:

$$n_{crit} \sim 10^{21} cm^{-3}$$

This resonant condition is called *optical breakdown* and it is achievable for intensities in the order of 10^{13} W cm^{-2}. Femtosecond pulses are so short that allow to use relative less energy to achieve optical breakdown and, in concert with the uncoupling between absorption and lattice heating, to increase the accuracy of FLM with respect to competitive techniques involving longer pulses **[36]**.

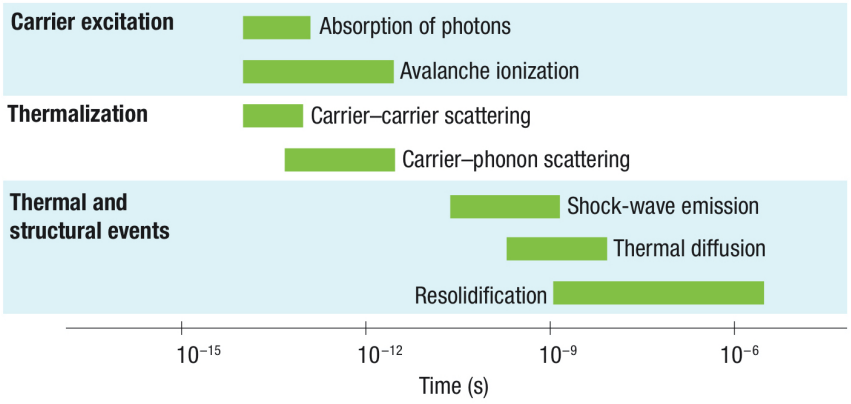

Figure 7: Timescale of the physical phenomena associated with the interaction of a femtosecond laser pulse with transparent materials. The green bars represent typical timescales for the relevant process. Note that although the absorption of light occurs at the femtosecond timescale, the material can continue to undergo changes microseconds later **[37]**.

For FLM the optical breakdown results to be deterministic, because it is possible to control the seed electron population through the non linear absorption processes above discussed, whereas the use of longer pulses would rely on the presence of defects and impurities to carry out the refractive index modification, leading to a stochastic occurrence **[59, 60]**.

2.2.7 Waveguides farbrication

The fabrication procedure relies on a computer controlled motion stage that allows to shift the sample in 3D changing the position of the focus in the substrate. The great potential of FLM lies in the freedom of choice of the writing parameters: all kind of geometry can be realized by modeling it, and the translation speed affects drastically the energy deposited. Moreover, it is possible to scan the waveguides several times, further controlling their performance.

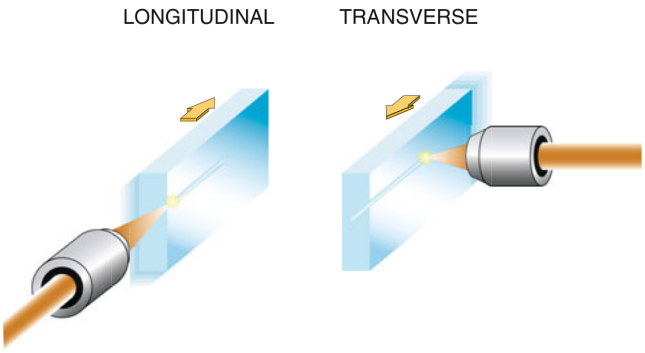

Figure 8: Writing geometry configurations **[36]**.

Two different writing geometries can be employed: a longitudinal configuration can induce a cylindrical symmetry well suited for the propagation of a mode with a symmetric profile but limited by the focal length of the lens, leading to limits in device's dimensions. A transverse configuration instead imposes no limits under this point of view, however it loses the cylindrical symmetry due to variation of the focusing condition in the direction parallel to the beam **[36]**. This configuration provides therefore waveguides with an elliptical cross-section and a propagated mode which becomes dependent on the light polarization. This problem can be overcomed by implementing beam shaping techinques **[61]**, by employing objectives with correction collars, or by oil and water immersion techniques.
During the fabrication process the laser is properly aligned through a sequence of mirrors, then the beam is focalized into the substrate thanks to *compensated objectives*. These allow to establish the depth of the focus and to reduce the risk of producing aberrations, being unreproducible. Moreover, the objectives increment the intensity at the beam waist, that naturally comes out from the divergence of the laser and the focusing action of the substrate, usually owing an higher refractive index with respect to the surrounding, in general air, water or oil. The immersion writing techniques has the advantage to remove every kind of dust particles from the upper surface of the sample, which may interact with the laser beam causing wrong energy deposition, inducing heterogeneity and aberrations within the same waveguide, affecting negatively the performance **[36]**.

Figure 9: Waveguides' fabrication.

2.3 Thermal diffusion regime

The energy relaxation of the plasma occurs through electron-phonon scattering (10^{-12}s) and happens long after the passage of the femtosecond pulse (10^{-15}s) and depending to the degree of excitation, cracking, void formation and localized melting can take place **[37]**.
It is so a crucial parameter the *repetition rate* of these pulses, i.e. the number of pulses that the laser can generate in a second. By changing this value and restricting the analysis to the waveguides writing, two different situations can be achieved, the *athermal regime* and the *cumulative heating regime* **[25]**. The former is reached for low repetition rates, in the order of kHz, and the modification is caused by each single pulse since the material has time to cool down, making this regime appealing for fused silica. Good performance can be achieved, but the Achilles heel is the slow writing velocity required, that would impose for centimeters long devices with complex geometries till hundreds of hours of writing time, being $v_{tras} \sim 10$ μm s^{-1} **[44]**. Moreover, this athermal regime is often coupled to a *multiscan* procedure, i.e. the focus of the laser passes through the already inscribed region to increase the performance.
But the major problem is represented by the low step index that could be achieved in the athermal regime in substrate like fused silica, resulting in lower confining waveguides with high propagation (1dB cm^{-1}) and bending losses (2 dB cm^{-1} with r = 90 mm). Also the coupling with optical fiber is negatively affected: the overlapping integral is $\sim$ 50 %, so about half of the light is lost.

It has been observed that for equal energy pulses and density, increasing the repetition rate leads to progressively lower propagation losses, enhancing thermal diffusion up to the cumulative heating regime, at MHz repetition rates **[25]**. At the *heat cumulative regime* the time interval between two subsequent pulses is shorter than the thermal

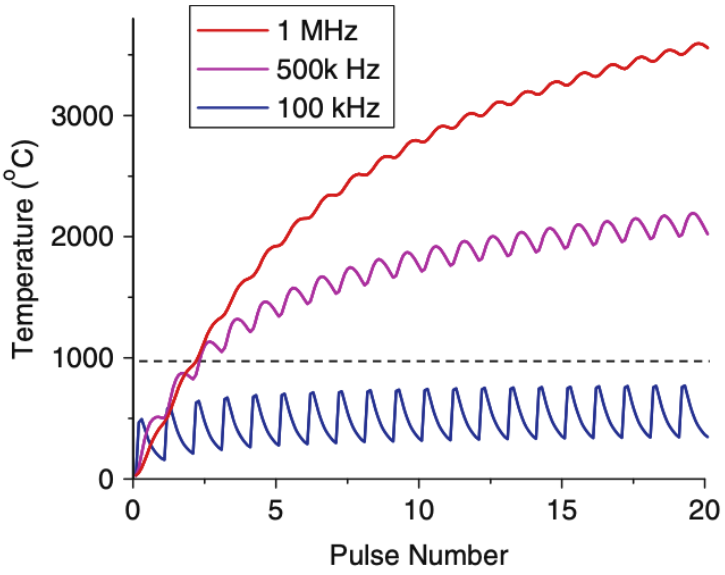

Figure 10: Model of glass temperature versus exposure at repetition rates of 100 kHz, 500 kHz, and 1 MHz, at a radial position of 3 μm from the center of the laser beam. The absorbed pulse energy of 200 nJ was the same at each repetition rate **[62]**.

diffusion time: the heat accumulates and the glass melts, then heat diffuses strongly and the glass quenches very quickly thanks to the higher writing velocity that can be employed, providing also shorter fabrication times **[37]**.
In case of waveguides written in a boro-aluminosilicate substrate, the global increment of n is not uniform and homogeneous, but can show different values according to the considered region: it is observed a *core region* with a positive refractive index change, or contrast, of the same order of commercial optical fibers, surrounded by a *depression region* where $\Delta n < 0$ meaning a reduction with respect to the unwritten glass and finally an external and wider *ring region* where the contrast is positive but lower with respect to the core one **[44]**.

2.4 Annealing

Different steps in the heating regimes induce a stress distribution in the substrate, which can induce a pronounced birifrangence that could lead to an unwanted polarization sensitive behavior of the fabricated circuit. It is convenient to remove such stresses also to reduce the ellipticity of the mode, favoring the fiber coupling with a more circular one.
In order to solve these problems, the annealing process is exploited. It consists in a thermal treatment in oven bringing the glass above the annealing point, a critical

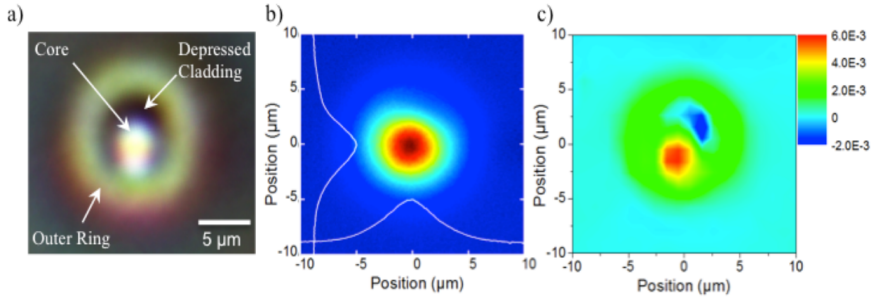

Figure 11: a) Micrograph image. b) Mode field profile al $\lambda = 1550$ nm. c) Refractive index profile at $\lambda = 635$ nm. Waveguides written in AEGLE 2000 at high repetition rate ($E_{pulse} = 40$nJ), **[44]**.

temperatures associated to the fluidic nature of glass, resulting in a macroscopic drop of the viscosity. For boro-aluminosilicate, at $T_{ann} \sim 722$°C it is $\nu = 10^{12}$ Pa·s and the stresses can relax in minutes. After that, a slow cooling in necessary to to keep the process as close to an equilibrium one as possible, bringing quasi-adiabatically the sample to room temperature. At $T_{st} \sim 669$°C is reached the *strain point* where the viscosity increases to $\nu = 10^{13.5}$ Pa·s and the relaxation occurs in hours. This threshold is important because below it, stresses are no more removed or induced, so whatever rate of cooling can be applied **[45]**.
After annealing, the outer ring is removed and the waveguides show a core region ($\Delta n > 0$), where the contrast is slightly reduced, whereas the narrow depressed region ($\Delta n < 0$) sees a contrast smooth increment **[44]**. These different regions are related to different steps in the diffusion process during the fabrication.

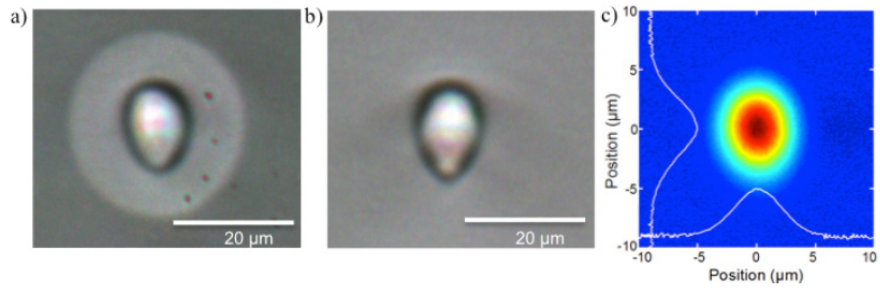

Figure 12: Bright field images of waveguides a) Before annealing; b) Post annealing; c) Refractive index post annealing (not in scale). **[44]**.

3 Experimental method and setup

The experimental activity is based on two main procedures that have been repeated many times in order to optimize the device: *fabrication* and *characterization*. This subdivision is valid for all activities involving integrated optical waveguides, regardless of the final application.

3.1 Fabrication

The aim of the fabrication is to inscribe the waveguides in the sample in the most reproducible way. The fabrication line has to be carefully prepared before any irreversible operation, and a long and meticulous cleaning of the glass surface is mandatory.

3.1.1 Fabrication setup

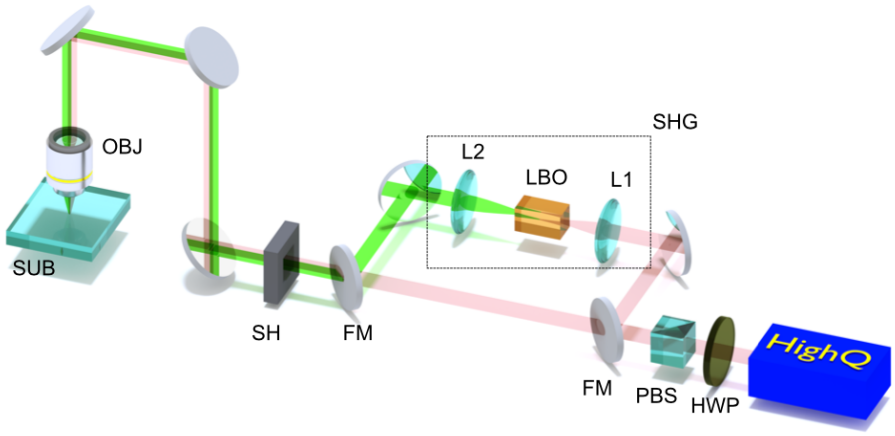

Figure 1: Schematic fabrication setup: HIGHQ: femtosecond laser realized in collaboration with the Max Planck Institute, HWP half-wave plate, PBS polarized beam splitter, FL flexible mirror, SH shutter, LBO lithium triborate crystal, L_1 and L_2 lenses with f_1 = 15mm and f_2 = 30mm **[24]**.

The setup of the fabrication line that has been employed is composed by a femtosecond laser with an emission wavelength of λ = 1030 nm, providing pulses with a time duration of τ= 350 fs and a maximum peak energy of E_{peak}=1 µJ. This source is a cavity-dumped mode-locked laser having as active medium a $KY(WO_4)_2$ crystal doped with Ytterbium and possessing an internal repetition rate of R = 17 MHz. A Pockels cell allows to extract from the cavity laser pulses with repetition rate from few kHz to 1.1 MHz, which can be set electronically. The resonant cavity of the femtosecond laser has been realized in collaboration with the Max Planck Institute **[63]**.

It is fundamental to carefully control the power of the laser, because small variations of this value can alter significantly the properties of the waveguides also within the same fabrication. To control the power, after the laser source are placed in sequence a *half-wave plate* and a *polarizer*. The former allows to rotate the polarization axis of the pulses coming from the laser source, whereas the latter filters light according to a fixed polarization: their combination allows to control the writing power and to provide a linearly polarized laser beam to be focused into the sample.
The first step of the fabrication process is the alignment of the laser beam. The power is not kept at desired value for fabrication, but at a lower one sufficient to see the laser beam though IR-photosensitive cards called *pinholes*: in this way is possible to align the beam through a sequence of mirrors, which allow to orient the laser beam perpendicularly to the sample surface. This is an iterative procedure involving several pinholes, mirrors and inspecting retro-reflexes. It is important to block the laser beam when placing or removing objects on the laser line and safety glasses are mandatory. Once the alignment condition is satisfied, it is possible to mount the objective and to align the objective to the beam. After the sample has been carefully cleaned and mounted, the focusing condition must be optimized via software through a near infrared CDD camera which inspects the retro-reflex at the glass surface, then it is possible to run the programs.
In this work, it has been used a 50x microscope objective, equipped with a correction collar for reducing the spherical aberrations, and with NA = 0.65, suitable for boroalluminosilicate and other substrates. The objective is kept fixed during the fabrication: the sample is mounted on a *motion stage*, a 3-axes air-bearing stage **Aerotech FiberGlide 3D**, that moves with respect to the focus, with three independent linear translation stages, allowing a position accuracy of 100 nm and a writing velocity up to 100 mm s^{-1}. A *mechanical shutter* **Thorlabs SH05** placed after the polarizer allows to block or transmit the beam, based on a computer input. The motion stage hosts a **ThorlabsGM100** gimbal-based adjuster that can be controlled both by hand both via software in G-Code language. The stage moves the sample to write the desired geometries and the shutter prevent unwanted inscriptions.

3.1.2 Optical microscope analysis

In order to check the success of the inscription procedure, the first step is a quick analysis with an optical microscope **Nikon ECLIPSE ME600**, objectives **Nikon Plan Flour 4x**, **10x**, **20x**, **40x**, showing eventual interruption of waveguides that may be caused by grains of dust at the surface remained despite the cleaning. A CCD camera **PixeLINK PL-B871** allows to inspect the waveguides from above, looking for interruptions, or by side, to check the success of the polishing procedure and guidance of light in transmission mode.

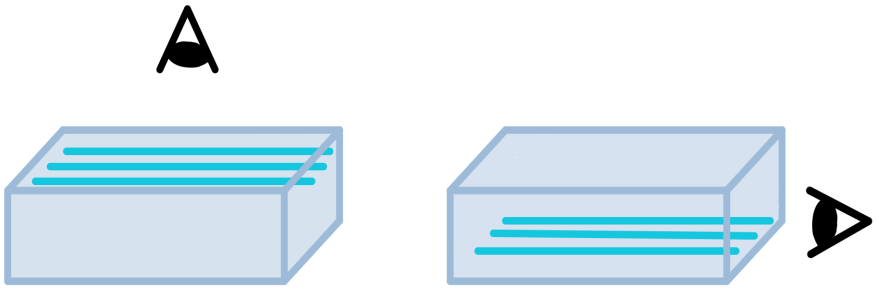

Figure 2: Up view of the sample to looking for waveguides interruptions and side view to see for scratches.

3.1.3 Anneling

If the waveguides do not show interruptions, it is possible to proceed with the annealing procedure in an oven. The program imposes a ramp that reaches T = 750°C in hour, above the annealing temperature, then the temperature decreases below the strain point till T = 630°C at a rate of -12 °C/h. The cooling rate is further increased first to -24°C/h till T = 500°C than to -200°C/h till room temperature. This recipe is a result of previous optimizations performed in the past.

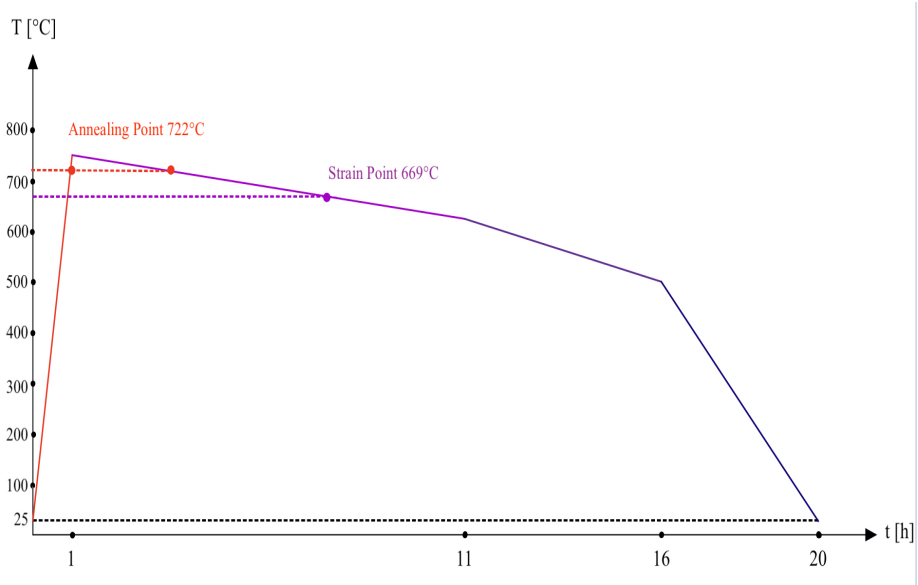

Figure 3: Thermal annealing ramp. The annealing and strain points are shown. Data referred to boro-aluminosilicate glass **Corning Eagle XG**.

3.1.4 Polishing

In order to procede with the waveguides characterization is necessary to smooth the interfaces of the sample hosting the guides' inputs and outputs. This procedure is called *lapping* and implies to use several disks of different roughnesses to polish the surfaces in a gradual and progressive way.
For small samples (wideness $\sim$ 2 cm) lapping can be carried on with a *lapping machine* **Krelltech**, which requires continuous adjustment by hand; for bigger samples a complete by hand procedure or a technician support is necessary, both assuring the best smoothy surfaces, fundamental for optimizing the coupling with the injected light.
In the manual procedure, the lapping steps involve four disks with their own roughness [μm] and lapping time and it has to be repeated for both sample faces:

- 800 or 600 μm disk is applied for 15 minutes to remove the major amount of glass at the faces to smooth big scratches;
- 30 μm disk for 5 minutes;
- 9 μm disk for 5 minutes;
- 0.3 μm disk for 3 minutes.

The lapping procedure sets the end of the fabrication: now the sample faces are optimized for light injection.

3.2 Characterization

During the characterization the guiding performance of the waveguides are tested. Many features have to be considered and different setups can be implemented, but the standard procedure consists in the injection of a light beam of known power form a laser diode with a single wavelength or broadband emission into the input of each waveguide, followed by the analysis of the output mode profile, performed by an *imaging camera*, or by the measurement of the output power through a *powermeter*. There are two main procedures for coupling the laser beam and the sample, each one showing its advantages.
An *objective coupling* requires a microscope objective to focus the laser onto the sample facet, mounted on a multi-axis micropositioner that allows to move it in three dimensions by hand. A precise alignment between the waveguide and the objective is required, since a typical guided mode has a radius of about 4 μm at 1550 nm. Moreover, for maximizing the power injected in the waveguide, it is also necessary to carefully match the working distance of the objective with the distance between objective and sample facet. The objective coupling is useful when a polarization analysis is required. Since the objective does not alter the polarization of the transmitted light, polarizers and wave-plates can be placed before it for injecting an arbitrary polarization state into the waveguide.
Another method is the *fiber coupling*, which requires an optical fiber to bring the laser beam to the sample facets. An optical microscope allowing a top-view inspection can be used to facilitate the alignment process. Indeed, the optimal alignment condition

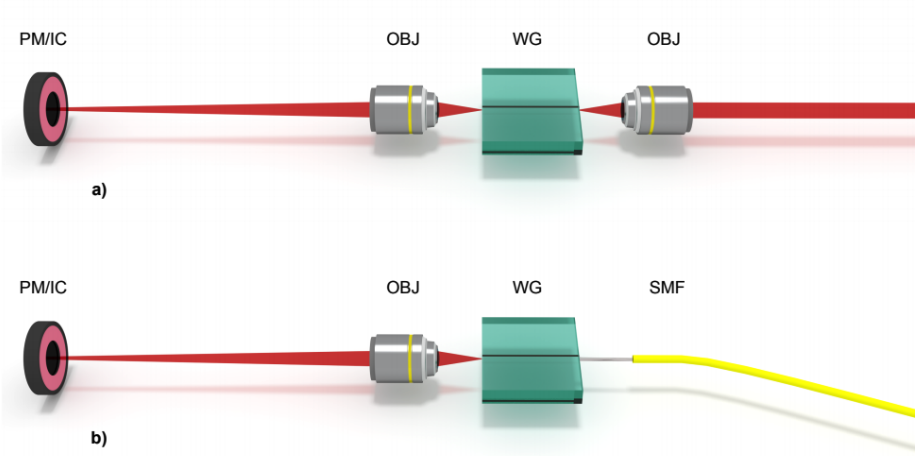

Figure 4: a) Objective coupling; b) Fiber coupling **[24]**.

occurs when the distance between the fiber and waveguide facets is in the order of hundreds of nm, so a microscope inspection allows to bring them very close without an actual contact, that would cause a quality degradation of the fragile fiber core. The fiber coupling is however less versatile than objective coupling when dealing with the analysis of the polarization behavior of the waveguides. Since standard optical fibers do not preserve the polarization state of the guided light, the injection of light with a known polarization would require expensive polarization-maintaining fibers or polarization controllers.

3.2.1 Mode profile

The first study that can be performed after the fabrication of a waveguide is the analysis of the guided mode. Indeed, depending on the energy deposited during the inscription process, the value and the shape of the induced refractive index contrast can be tuned for supporting the propagation of many modes, of only one single mode or even of no modes inside the waveguide. In integrated photonic circuits for applications in astronomy, usually single mode operation is preferred, because the fundamental mode enables the spacial filtering, reduces losses (especially bending ones), and allows to obtain a more reproducible coupling between close waveguides, when fabricating for example directional couplers. The measurement of the intensity profile of the guided mode permits to retrieve the electric field spacial distribution:

$$E(x,y) \propto \sqrt{I(x,y)}.$$

This operation requires the usage of a sensitive camera **InGaAs Xenics Bobcat 640**, that links the power to the number of activated pixels.

3.2.2 Insertion losses

Once analyzed the mode profile, the losses of the waveguides can be studied. In the characterization setup above discussed, two quantities are directly accessible: the power flowing from the diode laser through the optical elements *without* the sample (P_{in}) and the power measured passing through the optical elements *and* the sample (P_{out}). That is important because optical elements like objectives, wave-plates and polarizers induce intrinsic losses, that should not be taken into account for evaluating the waveguides' performance. So it is convenient to define the quantity called *insertion loss* expressed as:

$$IL = -10 \log\left(\frac{P_{out}}{P_{in}}\right),$$

and measured in dB. The ratio cancels the dependence of the losses on the optical elements, because each power can be factorized according to their effect. The minus sign underlines the fact that power is lost, so the value of IL result positive. Table [1] shows the IL values for some values of the $\frac{P_{out}}{P_{in}}$ ratio:

$\left(\frac{P_{out}}{P_{in}}\right)$	IL [dB]
1	0
0.90	0.45
0.75	1.5
0.50	3
0.25	6

Table 1: Conversion from ratio and logarithmic dB values.

The insertion losses can be decomposed into terms associated to the specific kind of losses afflicting the waveguides:

$$IL[dB] = FL[dB] + CL[dB] + PL\left[\frac{dB}{cm}\right] \times L[cm]$$

where FL are the Fresnel losses, CL the coupling losses, PL the propagation losses and L the length of a waveguides.

3.2.3 Fresnel losses

The Fresnel losses originate at the interface of the glass where the laser beam impinges and are due the refractive index difference between air and glass. We can define the *reflectance R*, seen as the portion of the light that is reflected so that the reflected power is:

$$P_r = RP_{in}$$

For normal incidence, we can write the *Fresnel equation*:

$$R = \left(\frac{n_{glass} - n_{air}}{n_{glass} + n_{air}} \right)^2$$

It is important to underline that techniques of *index matching* allow to reduce R exploiting materials like oil ($n_{oil} \sim 1.457$). In order to explicit the Fresnel losses is better to rewrite the equations with respect to the light transmitted by the waveguides, trough the *transmittance* T, such that T + R = 1, so the power transmitted:

$$P_t = T P_{in}$$

The Fresnel losses can be quantified as:

$$FL[dB] = -10 \log \left(\frac{P_t}{P_{in}} \right) = -10 \log \left(\frac{T P_{in}}{P_{in}} \right) = -10 \log (T)$$

In this way we have access to a directly measurable quantity $T = 1 - R$ instead of P_t, which exists in the glass after the interface. An average value for glasses for IR and visible light is $R \sim 4\%$ and $T \sim 96\%$, resulting in:

$$FL \sim 0.177 dB$$

3.2.4 Coupling losses

This kind of loss is referred to the coupling between the input of a waveguide in the sample and an optical element. This kind of loss depends on the overlapping between the electric field in waveguide E_w and the fiber one E_f, which depends on its radius a:

$$CL[dB] = -10 \log \left(\frac{\left| \iint E_w E_f^* dx\, dy \right|^2}{\left| \iint E_w dx\, dy \right|^2 \times \left| \iint E_f dx\, dy \right|^2} \right).$$

In case of objective coupling, the electric field at the focus of the microscope objective must be considered and instead of a its focal spot radius. If we consider a single modes both for waveguide and fiber, we get an expression depending on the modal coordinates in the waveguides x, y and the fiber core a:

$$CL[dB] \simeq -10 \log \left(\frac{(a^2 + x^2)(a^2 + y^2)}{4a^2 xy} \right)$$

To access the spacial variables x, y it is necessary to measure the field distribution from the intensity in the study of the mode profile with the IR-camera.

3.2.5 Propagation losses

The propagation losses are the principal cause of losses within the device and give best indication of the success of the fabrication. They quantify the light amount that is lost during the propagation inside a specific waveguide. This imply that the longer a waveguide is, the more it loses photons: this can be caused by a non uniform distribution inside the waveguide of the refractive index or to the presence of color or scattering centers. In order to compare different waveguides it is convenient to define a value normalized over their length:

$$PL\left[\frac{dB}{cm}\right] = -\frac{1}{L}10\log\left(\frac{P(L)}{P_{in}}\right)$$

$P(L)$ is the power measured after the light has passed through a waveguide of length L. Since the propagation losses are exponential with respect to the length of the waveguide, they become linear if expressed in decibel units. In order to retrieve the exponential behavior, the cut-back technique can be exploited. The same waveguide is cut several times and the propagation losses are measured for each length, so it is possible to obtain the coefficient of the exponential in a precise way. However, the sample is destroyed and at each cut polishing is required, therefore this kind of measure is very long and not suitable for a final device.
It is possible to retrieve the value of the propagation losses subtracting to the insertion losses the Fresnel and the coupling ones, which do not scale with length:

$$PL\left[\frac{dB}{cm}\right] = \frac{IL - FL - CL}{L}$$

3.2.6 Bending losses

The analysis carried till this point deals especially with straight waveguides, but FLM allows to write also bent waveguides with an arbitrary radius of curvature. This affects the light propagation inducing additional losses which increase as the radius decreases, although a smaller radius permits to write smaller devices. The bending losses show an exponential dependence on the radius:

$$BL \propto e^{-r_{curv}}$$

This behavior makes evident a limit in the design of devices. Indeed, FLM allows to fabricate circuits with an arbitrary geometry, and therefore radii of some μm could be employed: however, the typical bending losses limit this value to some mm, otherwise the losses would degradate the waveguide performance.
To evaluate the extent of these losses, straight waveguides with the same fabrication parameter have to be taken as reference.

$$BL\left[\frac{dB}{cm}\right] = -\frac{1}{L_{curv}}10\log\left(\frac{P_{curv}}{P_{straight}}\right),$$

where P_{curv} and $P_{straight}$ are the powers measured at the output of the device for the bent waveguide and the straight one, and L_{curv} the length of the curve track. This formula implies an approximation, i.e. the regions before and after L_{curv} are considered equal for both kind of waveguides. This allows to express the bending losses as a function of the insertion losses for straight and bent waveguides:

$$BL\left[\frac{dB}{cm}\right] = \frac{IL_{curv} - IL_{straight}}{L_{curv}}$$

4 Nulling interferometer design

The nulling interferometer presented in this work has the task to detect exoplanets with a peak emission wavelength at $\lambda = 1550$ nm, in the H band atmospheric transmission window. The fundamental constrains at the basis of its design are:

- Two telescopes coupling capability to exploit the Bracewell nulling interferometry;
- Broadband and polarization insensitive behavior, which imposes as a fundamental task the optimization of a broadband directional coupler;
- Improving the visibility function with an high control of the injected light to the central coupler: this accurate splitting control requires precision in the measurement of the light at the two inputs. Therefore photometric channels have to be realized in the most broadband and polarization insensitive way, providing a preferable balance splitting. Y-junctions have been studied for this target, showing in literature a more broadband behavior **[25]**.
- Realization of a Fan-in to avoid at the outputs the contribution of uncoupled light, that would reduce the quality of the signal and the visibility function.
- One or two resistances to control the relative phase of the beams at the inputs of the central coupler through termo-optical effect, tuning dynamically its operation **[46]**.

The project is born form a collaboration with the astrophotonics group of professor Lucas Labadie of the Köln University.

4.1 Straight and bending waveguides

The first fabrications were devoted to the optimization of the fabrication process for obtaining a single-mode waveguide with low propagation and bending losses at 1550 nm. In particular, different fabrication parameters were investigated, such as the power of the femtosecond laser, the translation speed of the sample and the number of scans. The power range has been investigated from $P = 400$ mW to $P = 700$ mW in steps of $\delta P = 30$ mW. For each value, three writing velocities have been varied: $v_{wr} = 10, 20, 40$ mm s^{-1} and for each velocity three scans $s = 3, 6, 12$. In a Y-junction, in order not to have interruptions, the central waveguide should be written with a number of scan that is double than the one employed for the two arms. For this reason, for every number of scan, we tested also its double, limiting our study to 12 scans.

4.1.1 Waveguides' positioning

A preliminary choice regards the writing depth of the waveguides in the chip. We are constrained to write them near the surface in order to control the nulling phase through the phase shifters. There's not an ideal distance from the surface, but it is fundamental to reproduce it as close as possible in all the fabrication: $25 - 30$ μm

should be sufficient to exploit efficiently the termo-optical effect induced by the phase shifters and at the same time preventing the waveguide facets to be scratched during the polishing procedure being at sufficient depth.

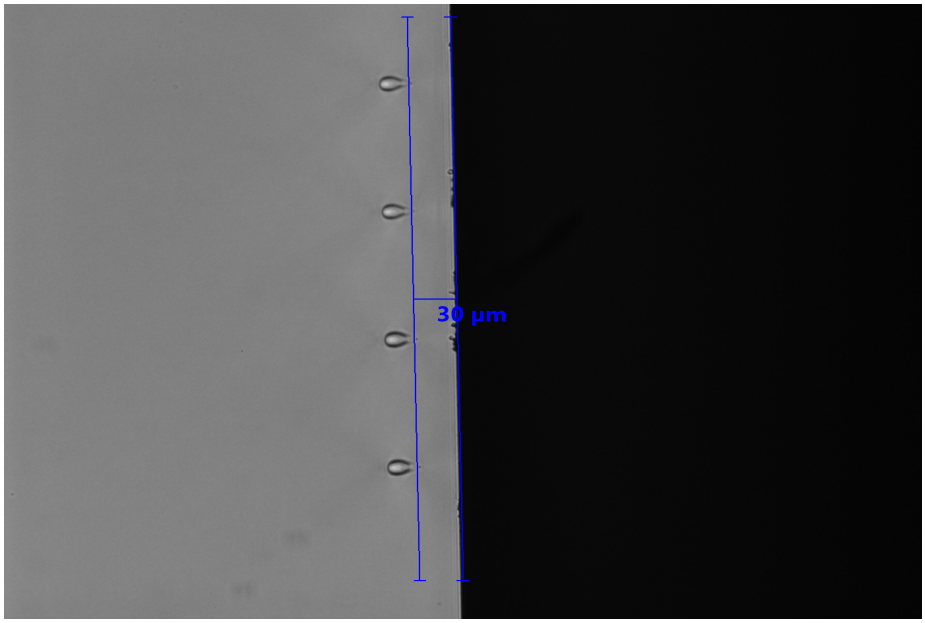

Figure 1: Waveguides written in the bottom, after polishing procedure. The clear region is the guiding core.

An *upper* configuration is more sensitive to the sample cleaning and grains of dust can completely ruin the fabrication by interrupting the focused laser beam during the inscription process. On the *bottom* instead we are not so sensitive to dust because the sample is thick $t = 1.1$ mm, so variation in the focusing condition, in the order of few microns, are only a fraction of percentage. However, spherical aberration can occur in this case, but this problem can be overcome using a objective with a correction collar, capable of adapting the internal optics for having always an optimal focusing condition also inside deep transparent materials. Considering all these reasons, we decided to fabricate the waveguides 30 µm above the bottom surface of the glass.

4.1.2 Mode analysis

The imaging camera analysis shows that waveguides written with higher powers and slower velocities are able to guide more than one mode, since the deposition of high energies during the fabrication is related to larger modification regions with higher refractive index contrasts. From $P = [580 : 700]$ mW single mode waveguides are found only for 40 mm s^{-1} and $s = 3$.

At lower powers $P = [490 : 580]$ mW waveguide pairs continue to be found for 40mm

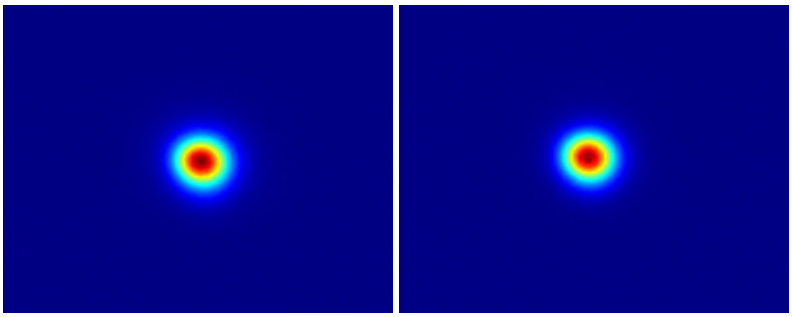

Figure 2: Single mode profile at $\lambda = 1550$ nm, for $P = 580$ mW, $v_{wr} = 40$ mms^{-1}, $s = 3$ (left) and $s = 6$ (right). For warm colors the intensity is higher and the cylindrical symmetry labels a gaussian mode.

s^{-1} and $s = 3$ but for also $s = 6$. Decreasing further the power, single mode behaviors appear but singularly with respect to the number of scan. So the most convenient region of investigation occurs for the following parameters:

$P = [580 : 400]$ mW $\qquad$ $v = 40$ mm s^{-1} $\qquad$ $s = 3$, $s = 6$

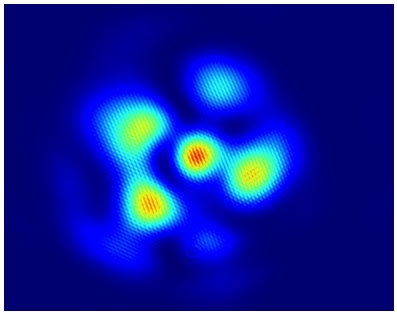

Figure 3: Example of multimode waveguide at $\lambda = 1550$ nm.

4.1.3 Losses

To identify the best performing waveguides, the study of the insertion, coupling and propagation losses must be carry out. The measurements were performed by coupling the waveguides with an **SMF-28 optical fiber**, capable of guiding a single mode at 1550 nm. Due to the fact that we are looking for a waveguides pairs, we focus our attention on the dependence on power for both number of scan. The analysis shows the same behavior almost independently of scans: increasing the writing power leads to less lossy waveguides.

Insertion losses

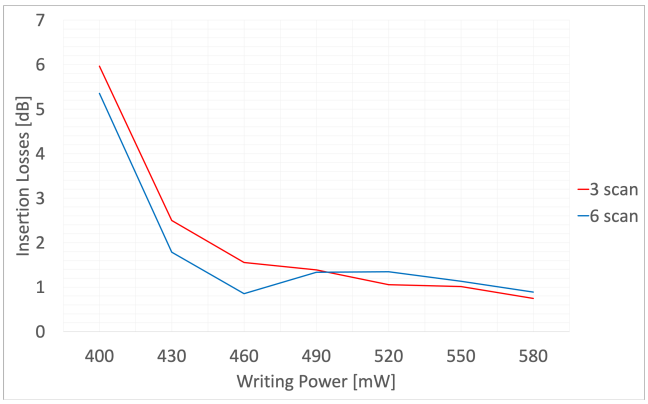

Figure 4: Insertion losses vs Writing power of waveguides written with $v = 40$ mm s^{-1} for $s = 3$ (red line) and $s = 6$ (blue line).

The insertion losses show minimal values around $P_{wr} = 580$ mW with $IL_{s=3} \sim 0.7$ dB and $IL_{s=6} \sim 0.8$ dB, assuring $\left(\frac{P_{out}}{P_{in}}\right) \sim 85\%$ and 83%.

Coupling losses

The retrieval of the coupling losses was performed via software by computing the overlap integral between the waveguide mode and the fiber one, both measured with an imaging camera.

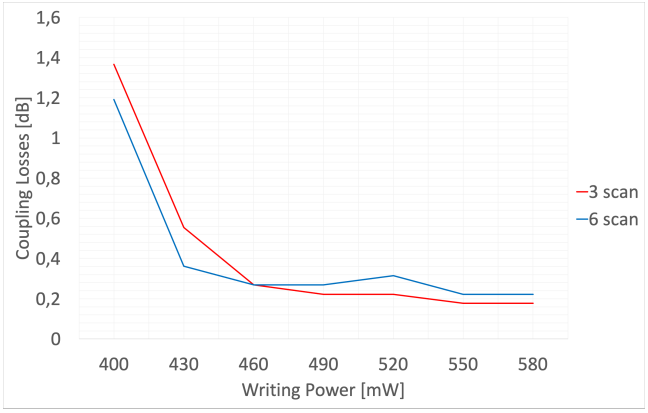

Figure 5: Coupling losses vs Writing power of waveguides written with $v = 40$ mm s^{-1} for $s = 3$ (red line) and $s = 6$ (blue line).

From the analysis, it emerges an interesting trend: the global behavior remains the same, i.e. higher powers reduce losses due to a better confinement, but in this case

the waveguides with $s = 3$ show better coupling performance with respect to $s = 6$, reaching a minimum value at $P_{wr} = 580$ mW of $CL = 0.2$ dB.

Propagation losses

Considering the propagation losses, we find the same qualitative behavior.

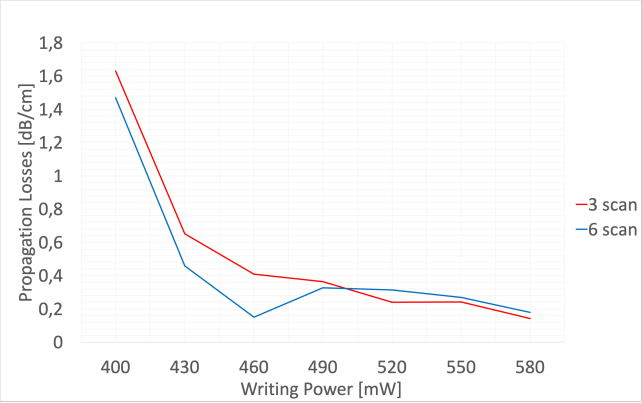

Figure 6: Propagation losses vs Writing power of waveguides written with $v = 40$ mms^{-1} for $s = 3$ (red line) and $s = 6$ (blue line).

Also in this case the minimum lies at the same power $P_{wr} = 580$ mW with values $PL_{s=3} = 0.1$ dB cm^{-1} and $PL_{s=6} = 0.1$ dB cm^{-1}. A similar fabrication has been repeated restricting the analysis to $P_{wr} = 580$ mW and to $P_{wr} = 460$ mW. However, $P_{wr} = 580$ mW still showed the best performances, so this power has been selected for the fabrication of the other integrated unities of the final interferometer.

Bending losses

The next step is to investigate the bending losses dependence on scan number and radius in the range $r = [15, 20, 30, 45, 60, 90]$ mm, for a length of the curved track of $L = 2$ cm.
The behavior, analogous to the condition $s = 6$, shows that till $r = 20$ mm the bending losses are extremely low, therefore it is possible to bend the waveguides without affecting the final performances.

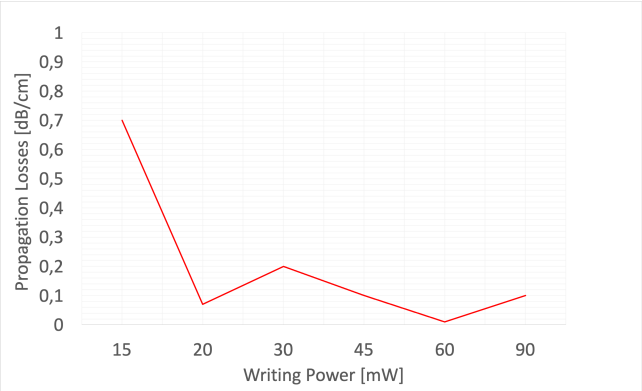

Figure 7: Bending losses vs Curvature radius for s = 3.

4.2 Y-junctions

The Y-junctions implementation has been very delicate, because we aimed to achieve for an intrinsically asymmetric integrated unity a broadband and polarization insensitive behavior. The fundamental mode propagating in the straight track of a Y-junction has to split into the two branches in equal ratio, without preferential propagation according to the input wavelength or polarization.

4.2.1 Symmetric Y-junctions

The first investigation was focused on the power splitting ratio dependency of symmetric Y-junction on radius. With *symmetric* we mean that the radii of the superior and inferior branch are the same, as well as the writing velocity. The scan number has been set to $s = 3$, so that the straight track results written with $s = 6$ and the scan cycle has been completed for a waveguide at time.
The radius range has been set to $r = [15, 20, 30, 45, 60, 90]$ mm for the parameter prior established; in this case several Y-junctions have been written many times with the same parameters in order to inspect eventual changes in the splitting ratio within the same fabrication and test reproducibility.

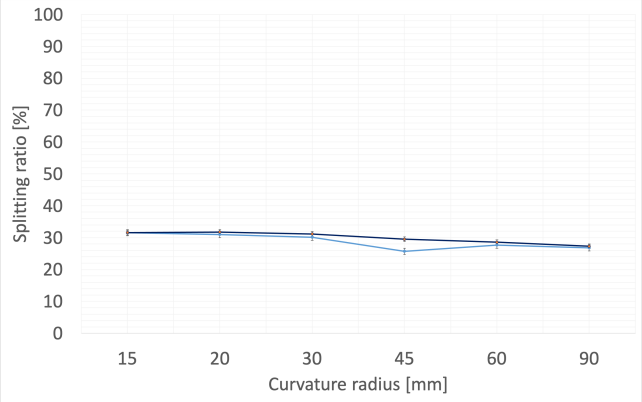

Figure 8: Symmetric waveguides, $v = 40$ mm s^{-1}. The two color indicate two series with identical writing parameters.

Although the similarities between the two fabrications evidence a good degree of reproducibility, the resulting behavior is far from the 50:50 splitting ratio, as shown in Fig. 8. The splitting ratio results different from the balanced condition because the light remains more coupled into the waveguide which has been scanned last. We have tried to sort this problem out in two ways: by reducing the radius of curvature of the last-written guide, increasing its losses, and to change the writing velocity imposing a detuning, in order to make the last-written waveguide's mode less confined.

4.2.2 Asymmetric Y-junctions

In this case the radius range has been extended to $r = [30 : 120]$ mm in steps of $\delta r = 10$ mm, cutting off $r = 15, 20$ mm because the losses for these radii are less reproducible. In order to avoid excessive dimensions and considering the performances of bending losses and couplers, $r = 30$ mm has been initially fixed for the first-written guide.

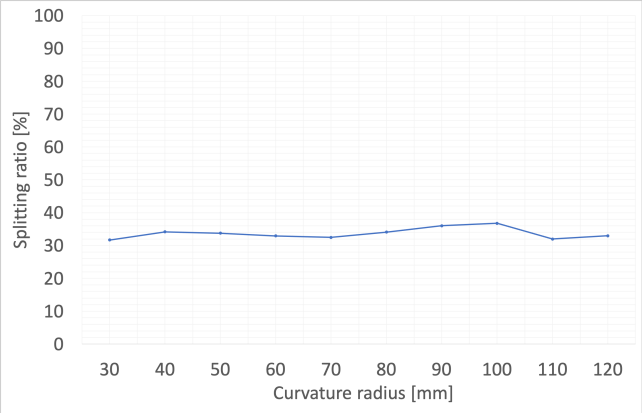

Figure 9: Asymmetric waveguides. The first guide has a radius of 30 mm. $v = 40$ mm s^{-1}.

The splitting ratio is still far from the balanced condition, as shown in Fig. 9. If we may accept a different splitting ratio, we surely cannot renounce to a broadband behavior. Hence a characterization over a band of $\Delta\lambda = 100$ nm with a broadband laser has been carried out, yielding the results presented in Fig. 10 for a horizontally polarized input and in Fig. 11 for a vertically polarized one. The band behavior is better for longer wavelengths, whereas for shorter ones some unwanted fluctuation occurs, but globally it could be considered a very good result, being the extremes within a 5%. The Y-junctions continue to be appealing, but a tailoring of the radius does not seem to have brought significative improvements in splitting ratio terms. At this point we decided to push further the fabrication, through two actions: a modification of the geometry, substituting a bend arm with a straight waveguide and a change in the velocity range. In the new geometry the unique bending waveguide, which forms a branch of the subsequent, is written after the straight one which will constitute the photometric channel.

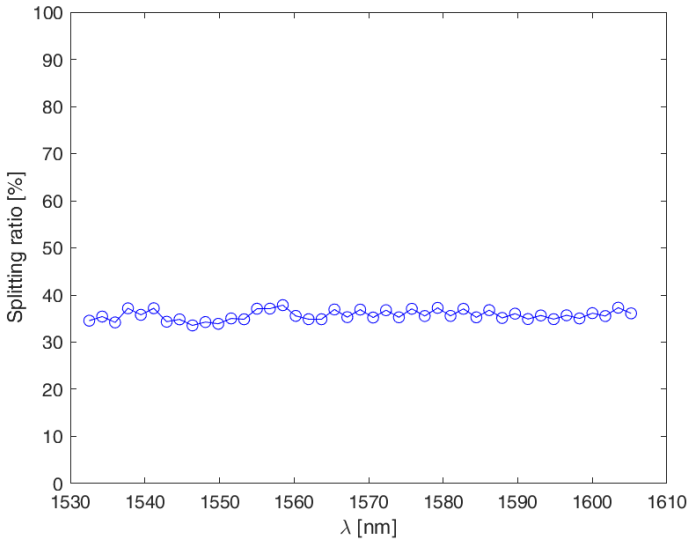

Figure 10: Wavelength behavior of asymmetric $r = (30; 60)$ mm Y-junctions for H-polarization.

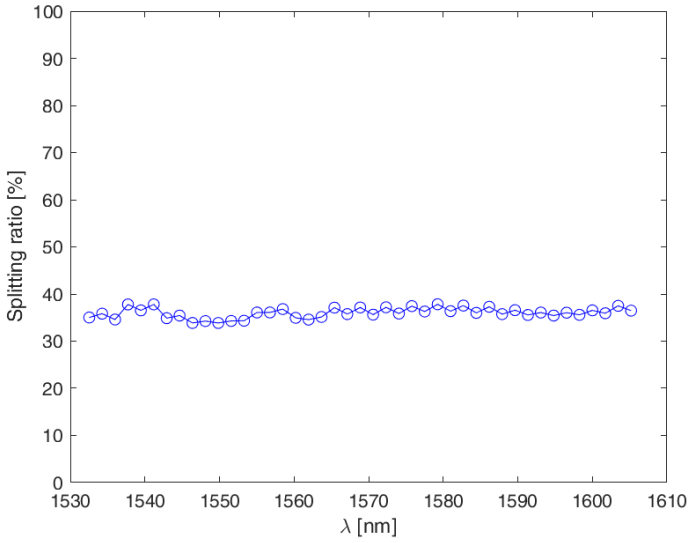

Figure 11: Wavelength behavior of asymmetric $r = (30; 60)$ mm Y-junctions for V-polarization.

4.2.3 Detuned Y-junctions

The writing velocity can significantly affect the guiding properties of the inscribed waveguides. So a further investigation has been carried out, taking into account the hypothesis to impose a detuning between the branches of each Y-junctions. This means trying to set a different propagation constant $\beta = n_{eff}k_0$ altering slightly the contrast through a writing velocity variation and scan order. The geometry has been kept symmetric, but the Y-junctions are not symmetric according to the mode propagation.
At first, we have imposed only a scan variation keeping the writing velocity fixed at $v = 40$ mm s^{-1} in order to be able to compare with previous fabrications.

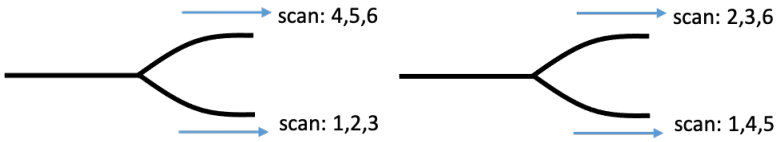

Figure 12: On the left, first scan order employed. On the right, new configuration. In both cases the waveguides have been written from left to right; the arrows indicate the writing directions and the numbers the scan order.

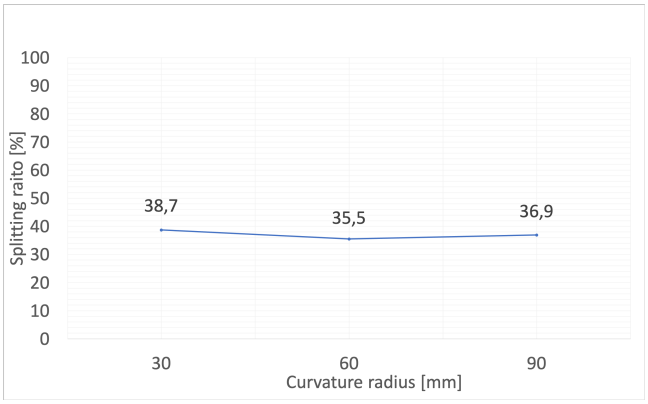

Figure 13: Splitting ratio dependence on curvature radius for Y-junction with $v = 40$ mm s^{-1} and scan order (2:3:6)(1:4:5) for detuned.

This scan order yields the results presented in Fig. 13.
We can see that the procedure has not lead to a shift of the curve: the scan order aimed to distribute the writing power more equally trying to achieve a similar index modification, but the splitting ratio is in practice equal to the previous fabrications. In a subsequent fabrication, we tried to control the detuning: in a symmetric geometry with an alternate scan order one waveguide has been written at constant velocity (40 mm s^{-1}) the other at higher velocity, inspecting a wide velocity range. This time radius of curvature has been kept fixed at $r = 60$ mm, for having negligible bending losses and therefore a more precise characterization of the splitting of the y junction.

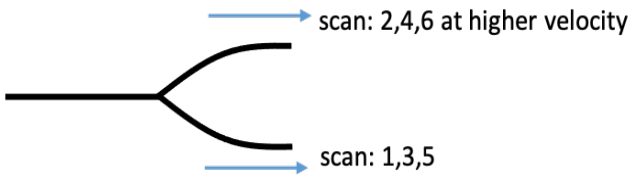

Figure 14: Writing geometry and scan order (2:4:6)(1:3:5) for detuned waveguides.

The velocity range has been set to $v_{high} = [40, 42, 44, 46, 48, 50, 52, 54]$ mm s^{-1}. The result is shown in Fig. 15:

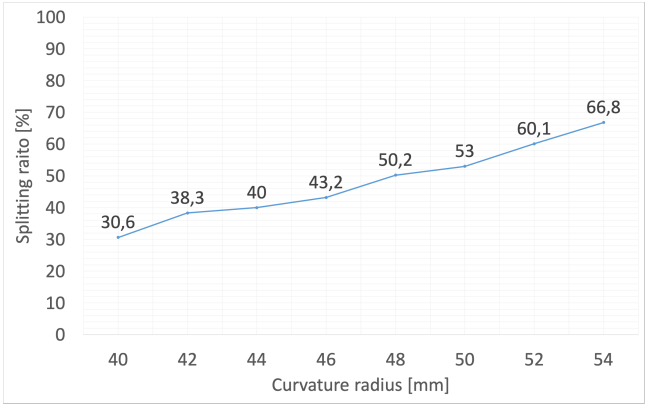

Figure 15: Power splitting ratio of detuned Y-junctions vs velocity, with $r = 60$ mm.

The splitting shows a linear dependence on the writing velocity of the waveguide written in the even scans. Moreover, we have found a Y-junctions with $SR \sim 50\%$ at $v_{high} = 48$ mm s^{-1}. This is an optimum candidate for the desired performances.
The detuned Y-junctions seem very promising in terms of splitting ratio, but the device application require in particular a response insensitive to polarization; therefore a characterization with the broadband laser in concert with a polarizer and a half-wave-plate has been carried out to the the performance of the device to both horizontal and vertical input polarizations.
The behavior looks worse with respect to the not detuned Y-junctions in terms of polarization and wavelength insensitivity, because the curve is neither flat neither the same for the polarizations. Moreover for higher writing velocities the gap between the polarization increases, leading to different splitting ratios depending on the polarization state. This constitutes a problem because we would have to choose between a polarization insensitive with an unbalanced splitting and a polarization sensitive 50:50.

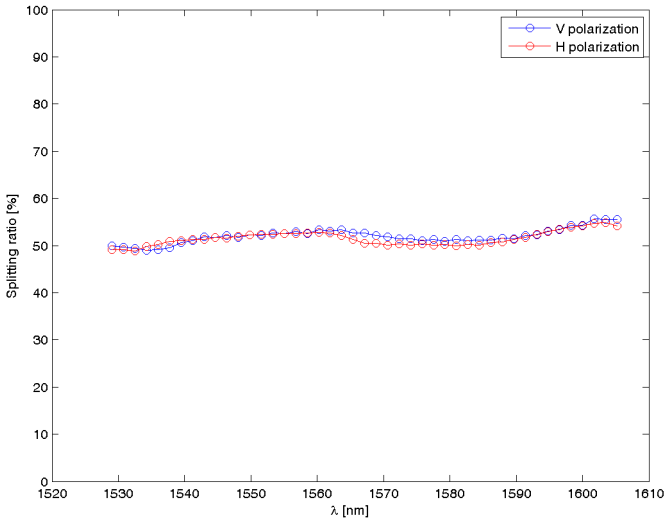

Figure 16: Polarization analysis with a tunable laser of a detuned Y-junction with $v_{high} = 48$ mm s^{-1} and $r = 60$ mm.

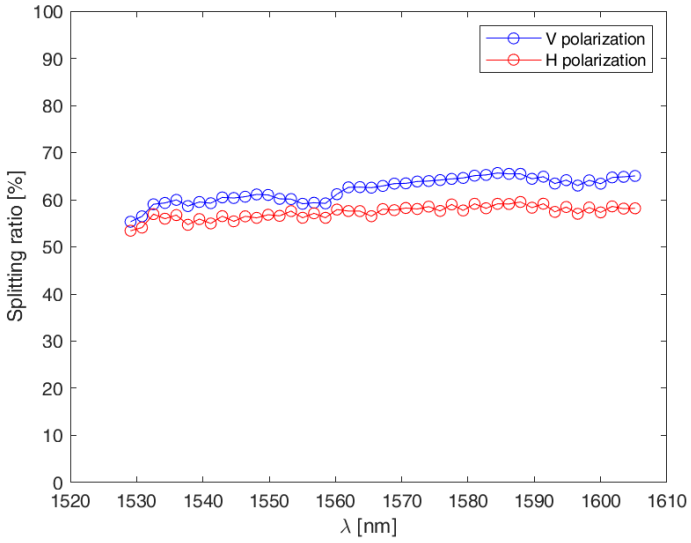

Figure 17: Polarization analysis with a tunable laser of a detuned Y-junction with $v_{high} = 50$ mm s^{-1} and $r = 60$ mm.

4.3 Directional couplers

There are three main parameters ruling the behavior of a directional coupler: the distance d between the waveguides in the coupling region, the coupling length L and the curvature radius. These play in concert with the writing power and velocity. Hence an overall optimization required many trials to achieve a mandatory balanced and broadband condition , which would guarantee a perfect interference leading to a minimum nulling ratio. The reflectivity, i.e. the fraction of light that remains in the input waveguide, has the following behavior:

$$R(\lambda) = \frac{P_{bar}}{P_{cross} + P_{bar}} = \sigma^2 sin^2 \left(F(\lambda)L + \phi(\lambda)\right)$$

Hence the parameters that we are able to control will stretch or translate this ideal trigonometric function: it is useful to explicit the dependences apart the wavelength. Being

$$\sigma = \left[1 + \left(\frac{\Delta\beta}{2\kappa}\right)^2\right]^{-1/2},$$

we can understand that the detuning $\Delta\beta$ is able to modulate the curve. Therefore, we should find a way to induce different propagation constants $\beta = k_0 n_{eff}$. This can be achieved changing the dose of the radiation, thorough a control of the writing velocity. However, the behavior of the reflectivity on the detuning is not linear, because its dependence is also present in the effective coupling coefficient:

$$F(\lambda, d, \Delta\beta) = \frac{\kappa(\lambda, d)}{\sigma(\lambda, \Delta\beta)},$$

which can induce also a translation of the reflectivity value due to the period variation. It is here fundamental the coupling distance d: the greater it is, the smaller is the overlap integral between the two modes. The coupling will be less strong and less sensitive to fabrication fluctuations, resulting in a wider period of the reflectivity. A crucial role is finally played by the bending phase:

$$\phi = \phi(\lambda, r),$$

related to an evanescent coupling occurring also before the coupling region, due to the approaching of the two waveguides while they are bending. This evanescent coupling is dependent on the radius of curvature: if the radius is high, the waveguides start early to bend, seeing each other in a wide region before reaching the coupling one. This parameter allows us to tailor in detail, adjusting and optimize the performances through many trials.

4.3.1 Symmetric Couplers

In the first analysis the interaction length of symmetric couplers has been investigated, involving couplers with a relative large distance d =9 μm and radii of r = 45 and 60 mm, a good compromise between low bending losses and compactness of the circuit. By symmetric we mean that the geometry and the writing velocity of the waveguides are the same. L has been varied in [0: 2.6] mm in steps δL = 0.2 mm.

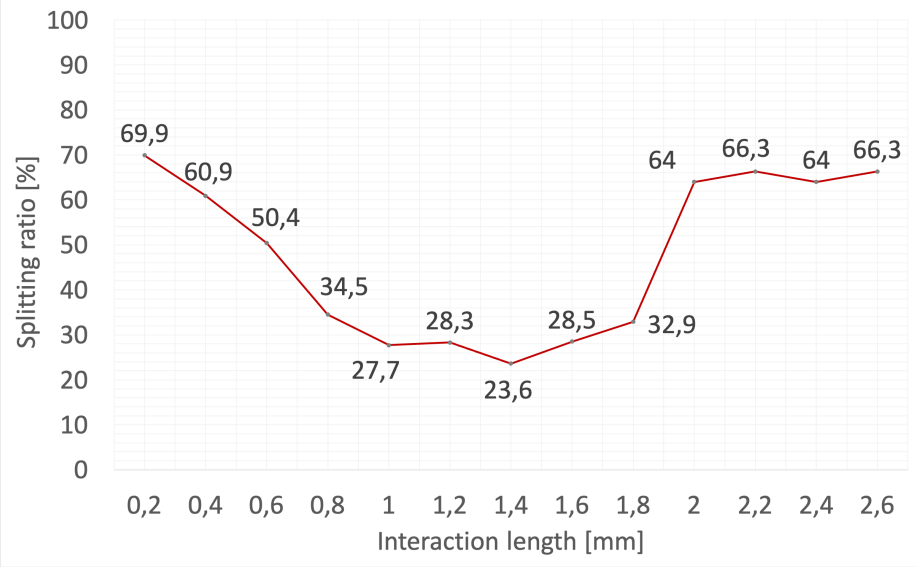

Figure 18: Symmetric couplers, d = 9 μm and r = 45 mm.

Although a balanced directional coupler has been found for L = 1.6 mm and r = 45 mm, the global behavior does not appear very regular and this threats reproducibility: another fabrication with the same parameters will show the extension of these fluctuations.
In this second trial the interaction lengths range has been reduced and the sampled space varied; the behavior remains irregular even if we have found a gap where the splitting ratio has set around 50%. Moreover, literature evidences show the possibility to reach a broadband behavior applying a detuning **[33]**. Therefore, in parallel with the Y-junctions, also for the directional coupler has been checked the influence of a detuning by changing the writing velocity of an arm with respect to the other.

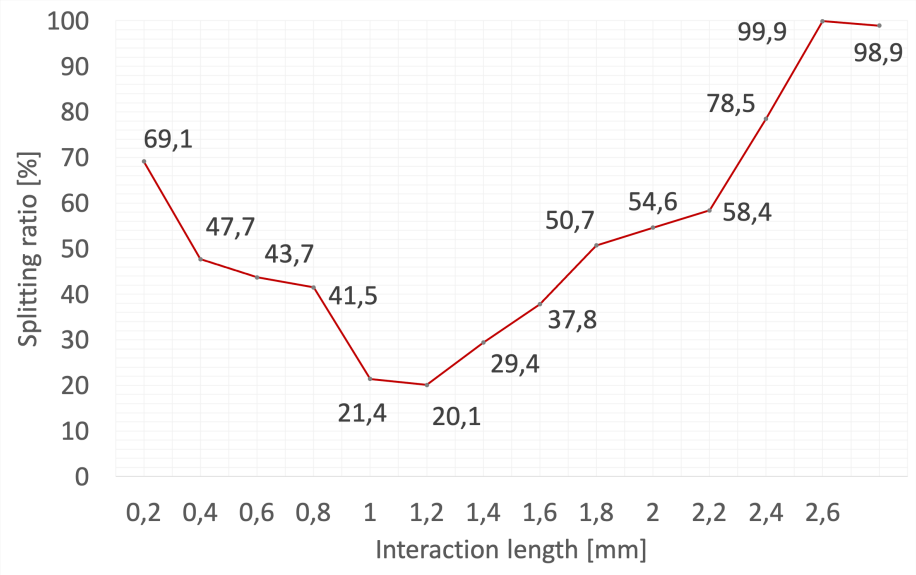

Figure 19: Symmetric couplers, d = 9 μm and r = 60 mm.

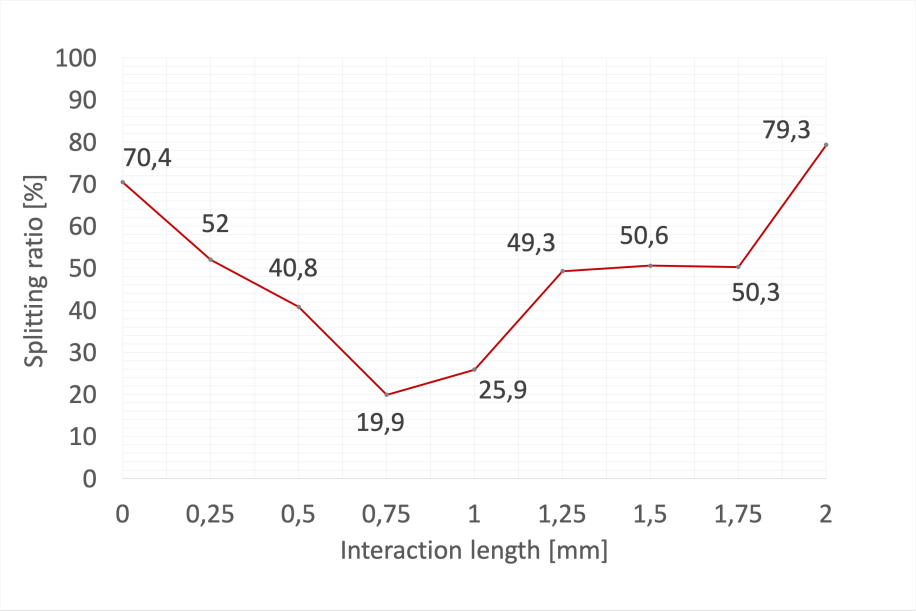

Figure 20: Symmetric couplers, d = 9 μm and r = 45 mm. Second trial.

4.3.2 Detuned Couplers

In this fabrication the curvature radius has been kept at r = 45 mm and four velocity-detuning have been tested, to inspect the achievable detuning:

v_{low} [mm/s]	v_{high} [mm/s]
37.5	42.5
35	45
32.5	47.5
30	50

Table 2: Writing velocities to detune the arms of the couplers.

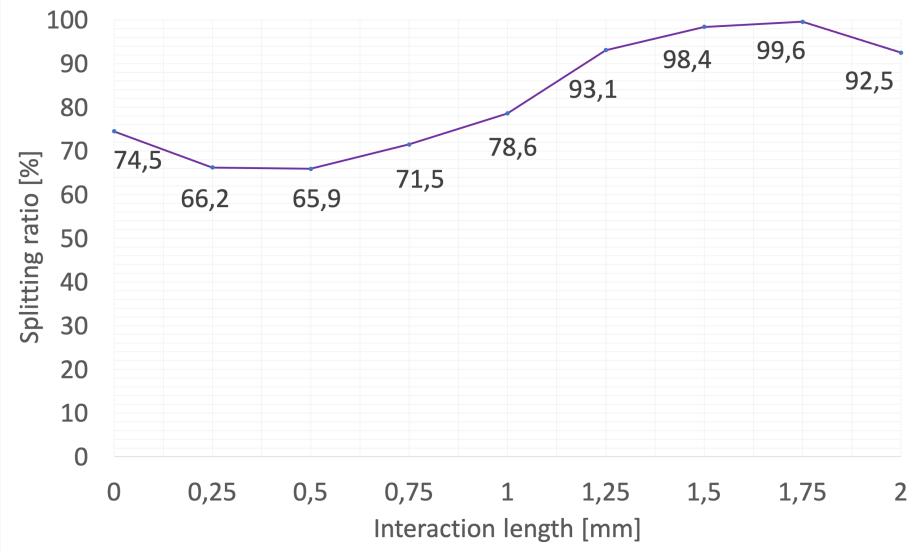

Figure 21: Detuned couplers at v = (37.5 ; 42.5) mm s^{-1} with d = 9 µm and r = 45 mm tested for different interaction lengths.

In this case the behavior is excellent because we have got the perfect $sin^2()$ trend, but the imposed detuning has shift to higher reflectivity the whole curve and no more balanced couplers have been found.
An elevated writing velocity difference between the waveguides feeds a stronger detuning that reduces the achievable power transfer. In this case indeed the reflectivity, thus the light fraction remaining in the bar channel, does not reach 0 but remains close to 1. For this reason, for obtaining a balanced directional coupler, we needed to reduce the induced detuning and therefore the velocity difference.

4.3.3 L = 0 couplers

The reflectivity depends on the wavelength and so do $F(\lambda)$ and $\phi(\lambda)$, but these contribute with different slopes: the bending phase for symmetric couplers shows a negative slope $\frac{d\phi(\lambda)}{d\lambda} < 0$, the opposite happens for coupling term $\frac{dF(\lambda)}{d\lambda} > 0$. Therefore it is convenient to set $L = 0$ and study the contribute of the bending phase to dispersion, thus reducing the involved parameters and decoupling the contributes, and then optimize them. Moreover, in case of symmetrical couplers ($\Delta\beta = 0$) a flattened response can be obtained compensating the dispersion between the straight and the bend waveguides in $1250 < \lambda < 1650$ nm, whereas for asymmetric ones a broadband response can be achieved minimizing the dispersion in the bend region and taking short interaction lengths **[33]**.

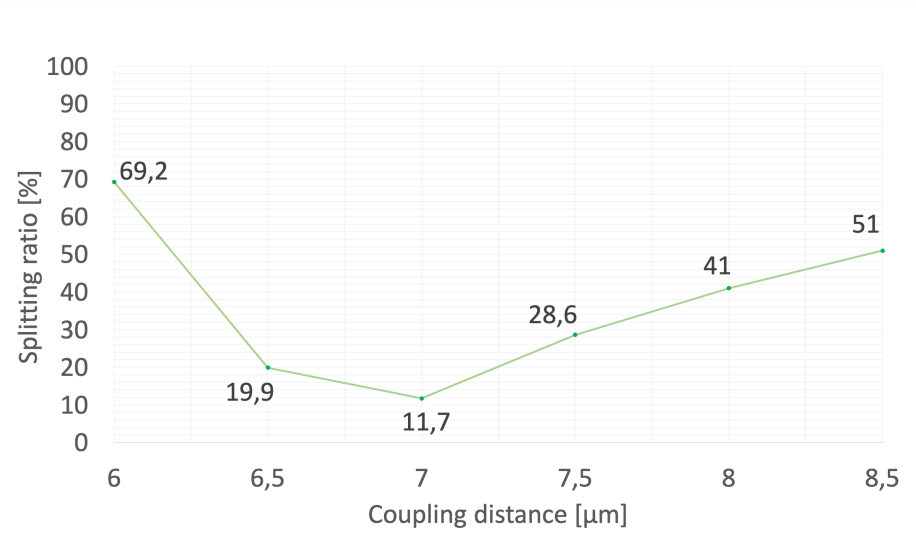

Figure 22: Symmetric couplers at v = (40 ; 40) mm s^{-1} with $L = 0$ mm and $r = 60$ mm, tested for different coupling distances.

We started writing symmetric couplers at the radii of interest $r = 45$ mm and $r = 60$ mm and tailoring over the coupling distance d, reducing its value with respect to previous cases, expecting for smaller d an increment in the coupling coefficient due to a major overlapping integral.
The gap 6 µm $< d <$ 6.5 µm in Fig. 22 is crossed by a balanced splitting ratio value, thus if we want to exploit the advantages to take a null interaction length, i.e. a more reproducible and controllable design, the region of small d must be investigated, trying to understand better the role of the radii and imposing a slightly detuning.
For this reason we have fabricated a set of couplers at $d = 6$ µm, $d = 6.5$ µm, $d = 7$ µm, in a wide radii range $r = [30 : 100]$ mm in $\delta = 10$ mm both detuned and not detuned.

Detuned couplers L = 0

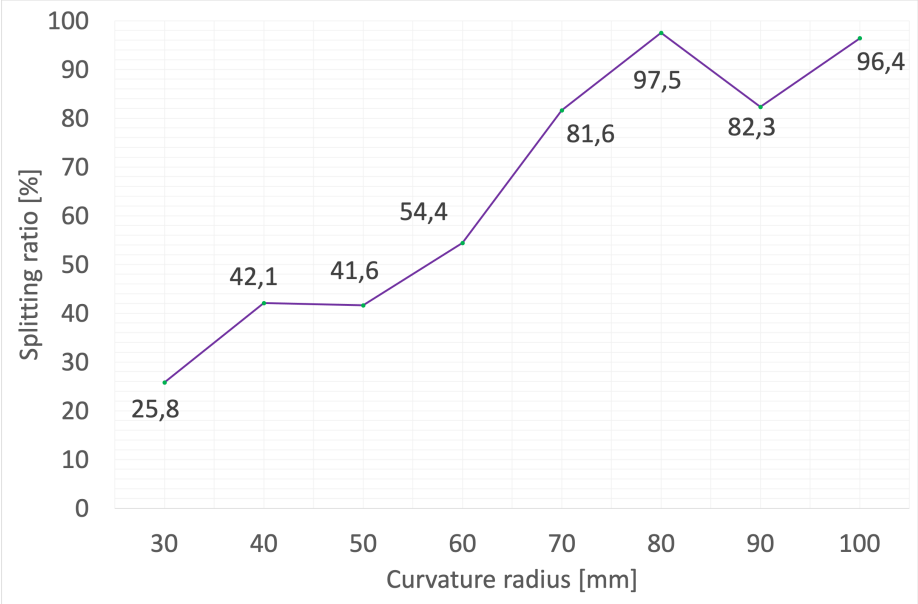

Figure 23: Detuned couplers with $d = 6$ µm, $(v_{low}; v_{high}) = (39; 41)$mm s^{-1}.

Focusing on the detuned couplers, we can notice that for great distances and high radii the reflectivity drops: since the evanescent coupling starts in the *bending region*, where the waveguides begin to bend and get progressively closer, greater radii let the waveguides interact before reaching the coupling region.
Among the detuned couplers, three reflectivity values close to the balanced condition have been found: at this point a polarization and wavelength analysis of these is required to understand whether the null-length couplers are worthy to be further developed. Some of the results are showed in Figs. 26 and 27.
The global band behavior is very satisfactory, especially for the $r = 60$ mm coupler that exhibits an excellent flat response over more than 100 nm, where the polarization fluctuation of the splitting ratio is $\sim 1\%$. The null-length configuration is at this point a definitive choice: we can obtain a flat band response, eliminating a degree of freedom among the parameters and so more facility to handle with the others. The key procedure shall be therefore a tailoring of the radius in parallel with the coupling distance, iterating in order to achieve the balanced condition.

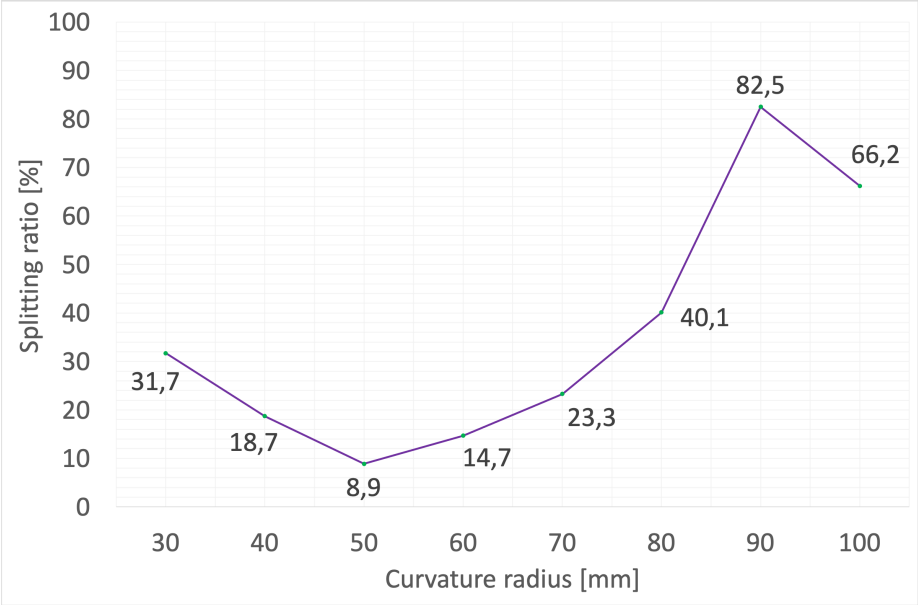

Figure 24: Detuned couplers with $d = 6.5$ µm, $(v_{low}; v_{high}) = (39; 41)$mm s^{-1}.

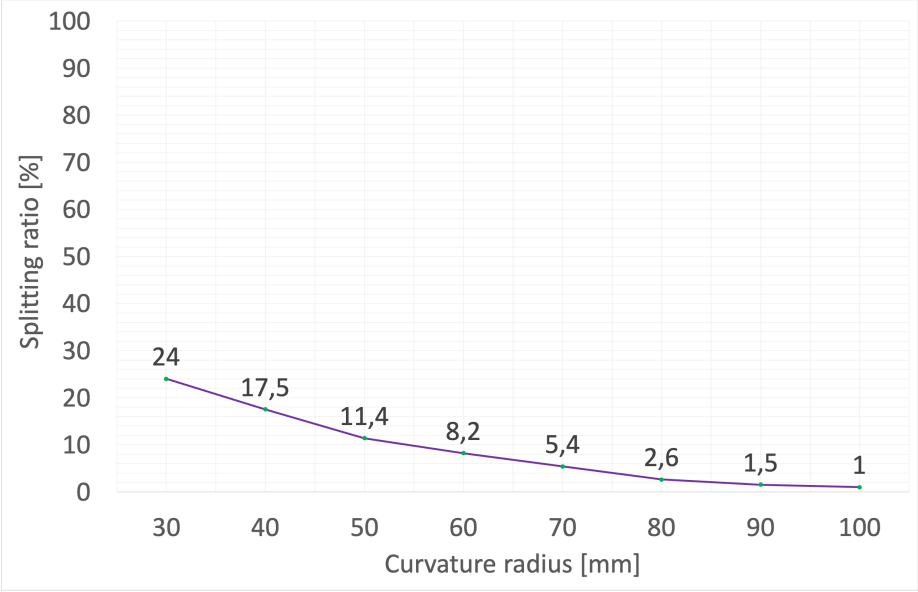

Figure 25: Detuned couplers with $d = 7$ µm, $(v_{low}; v_{high}) = (39; 41)$mm s^{-1}, tested for different radii.

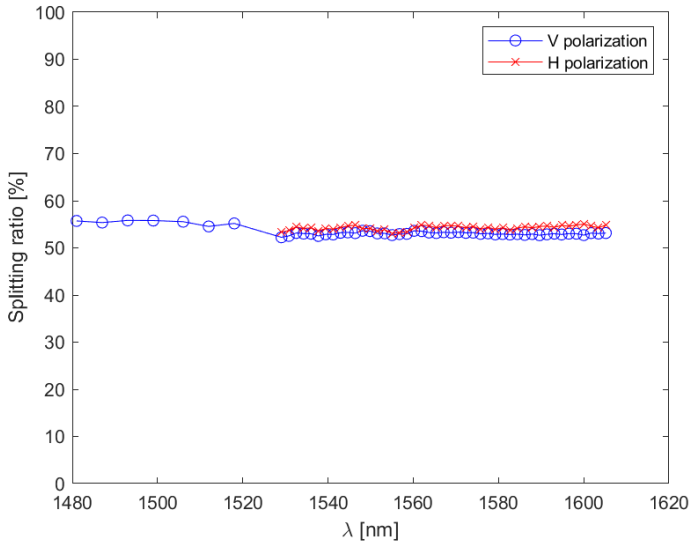

Figure 26: Broadband behavior of polarizations' components of detuned couplers d = 6 μm and r = 60 mm.The blue line at shorter wavelengths have been taken with a tunable laser for V polarization.

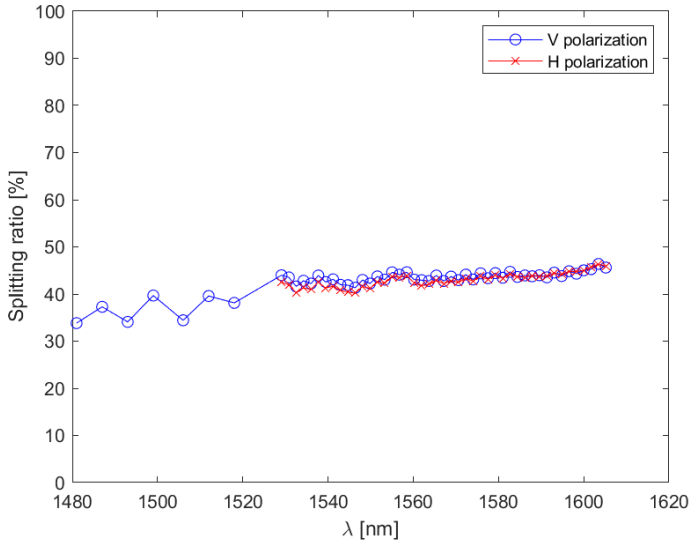

Figure 27: Broadband behavior of polarizations' components of detuned couplers d = 6.5 μm and r = 80 mm.

Not detuned couplers

The same procedure has been done for symmetric couplers without exploiting the shift of the detuning, but trying to achieve the balance condition with the radius modulation alone. The reflectivity values are shown in Figs. 28, 29 and 30, whereas the wavelength and polarization behavior in Figs. 31 and 32.

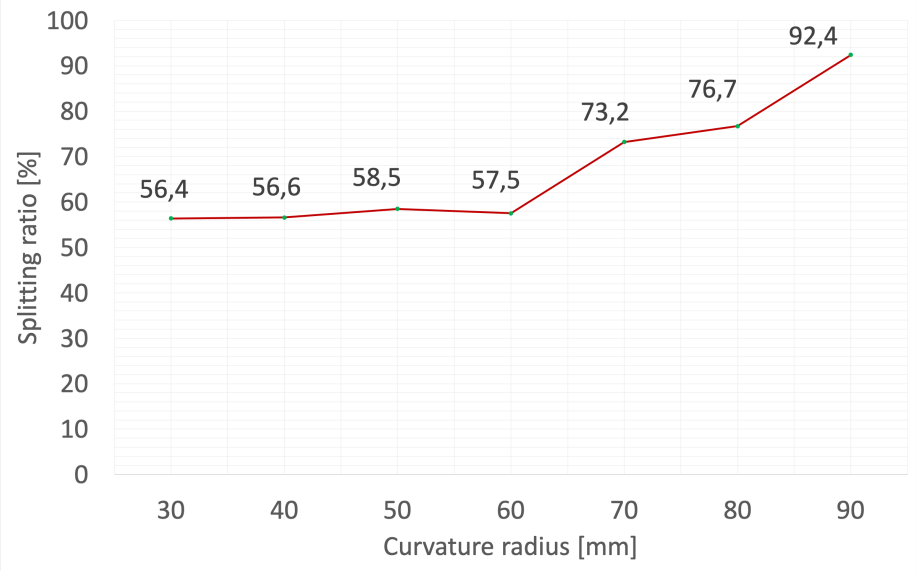

Figure 28: Symmetric couplers with $d = 6$ µm, $v = (40; 40)$ mm s^{-1}, tested for different radii.

For $d = 7$ µm no balance splitting ratio has been found, as shown in Fig 30. At higher distances we continue to find the balanced condition for longer radii, whereas in the nearby of $d = 6$ µm smaller radii seem to be sufficient. Therefore it is convenient to investigate further the null-length couplers for short distances, both detuned and not detuned.
The coupling distance has been tailored with $\delta d = 0.1$ µm (Figs. 33 and 35): this value is comparable to the positioning precision of the translational stages employed during the fabrication. Moreover, since the waveguides are very close in the interaction region, even the smallest noise on the distance between them can alter the splitting ratio of the directional coupler. Considering these aspects, we expect the future fabrications to be less reproducible than the standard performances achievable with FLM. Nevertheless, this does not represent a problem for the fabrication of the final device, since in the latter only the central directional coupler has strict requirements on the splitting ratio. The detuned couplers have been inspected for $d = 6, 6.1$ and 6.2 µm, whereas the symmetric for $d = 6$ and 6.3 µm.

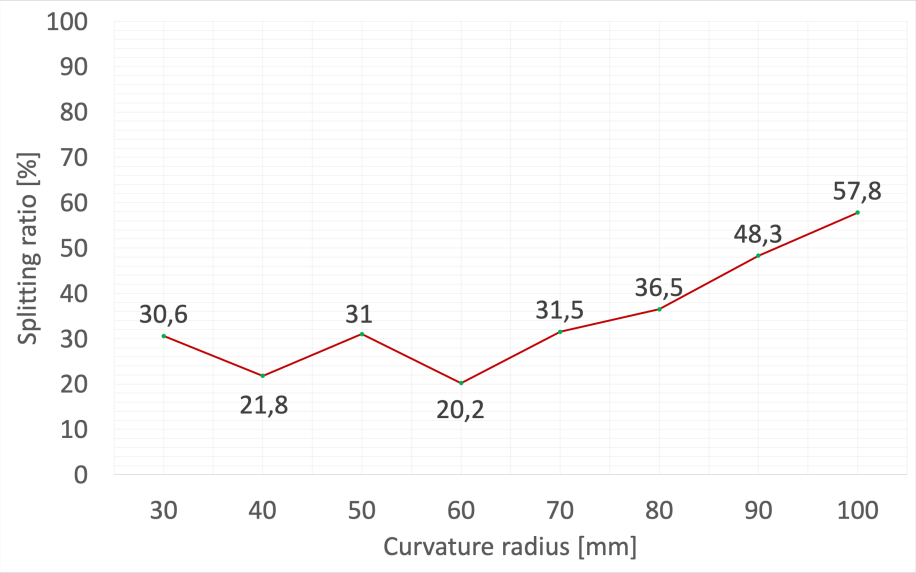

Figure 29: Symmetric couplers with $d = 6.5$ µm, $v = (40; 40)$ mm s^{-1}, tested for different radii.

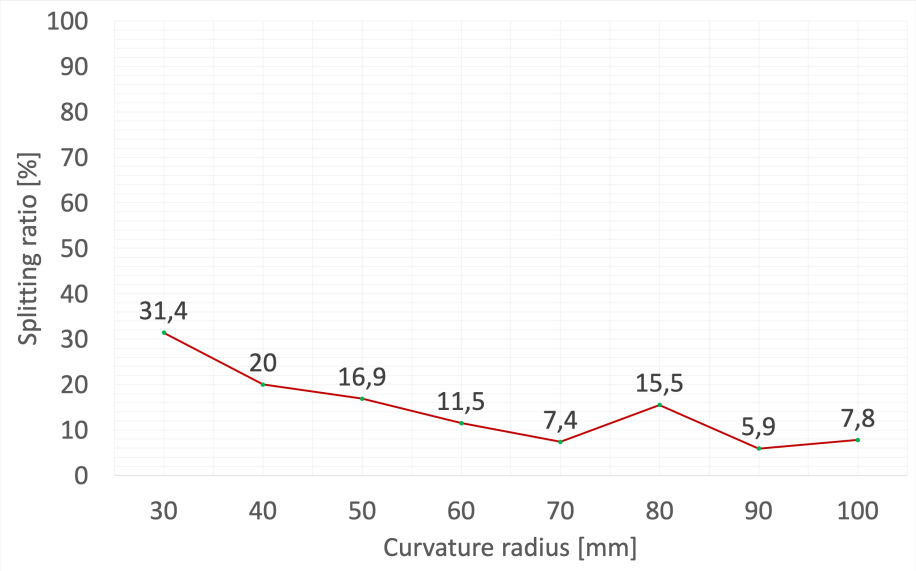

Figure 30: Symmetric couplers with $d = 7$ µm, $v = (40; 40)$ mm s^{-1}, tested for different radii.

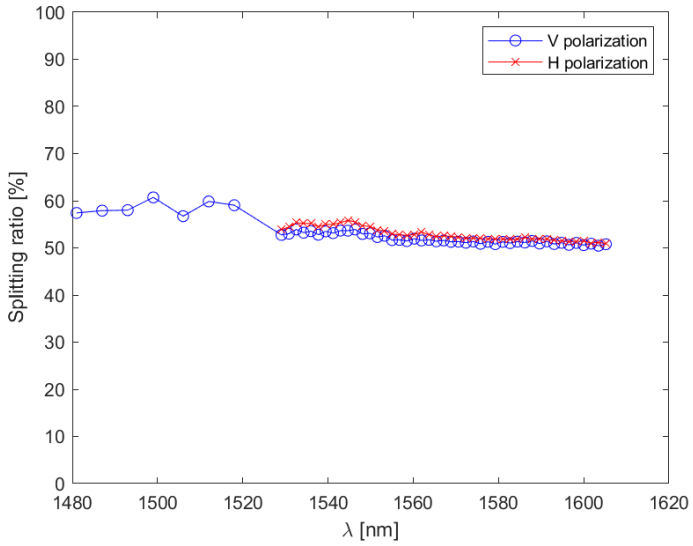

Figure 31: Broadband behavior of polarizations' components of symmetric couplers $v = (40; 40)$ mm s^{-1}, $d = 6$ µm and $r = 40$ mm.

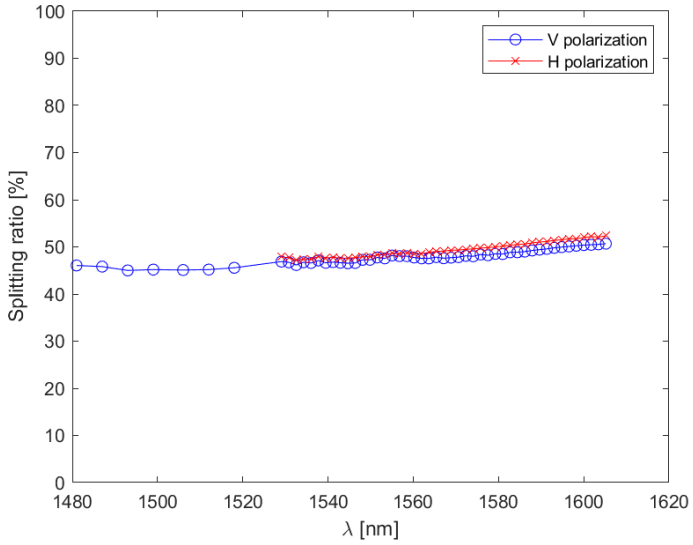

Figure 32: Broadband behavior of polarizations' components of symmetric couplers $v = (40; 40)$ mm s^{-1}, $d = 6.3$ µm and $r = 90$ mm.

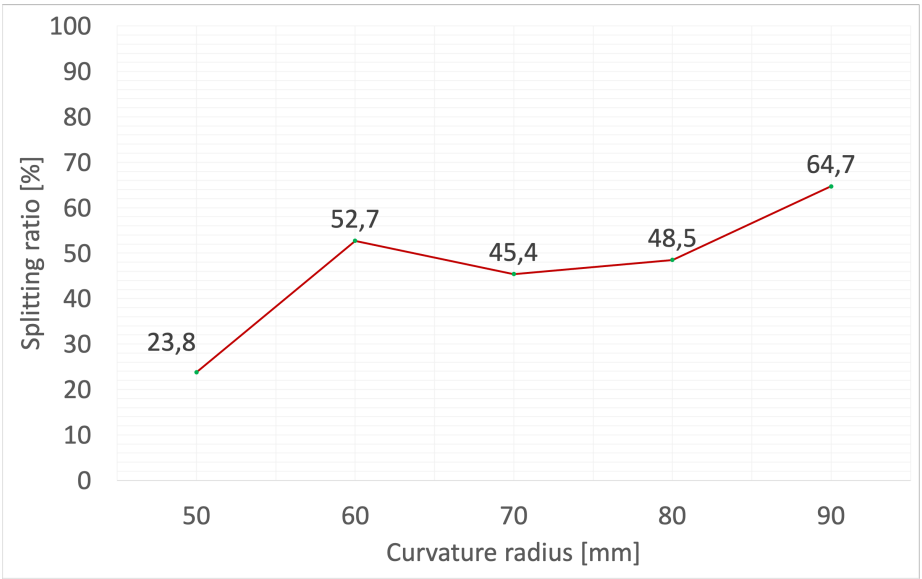

Figure 33: Symmetric couplers $v = (40; 40)$ mm s^{-1}, $d = 6.3$ μm.

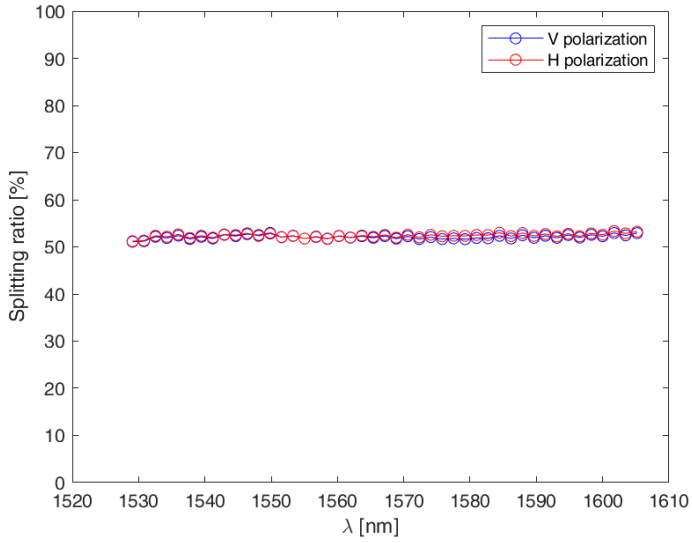

Figure 34: Broadband behavior of polarizations' components of detuned couplers $v = (39; 41)$ mm s^{-1}, $d = 6$ μm and $r = 52.5$ mm.

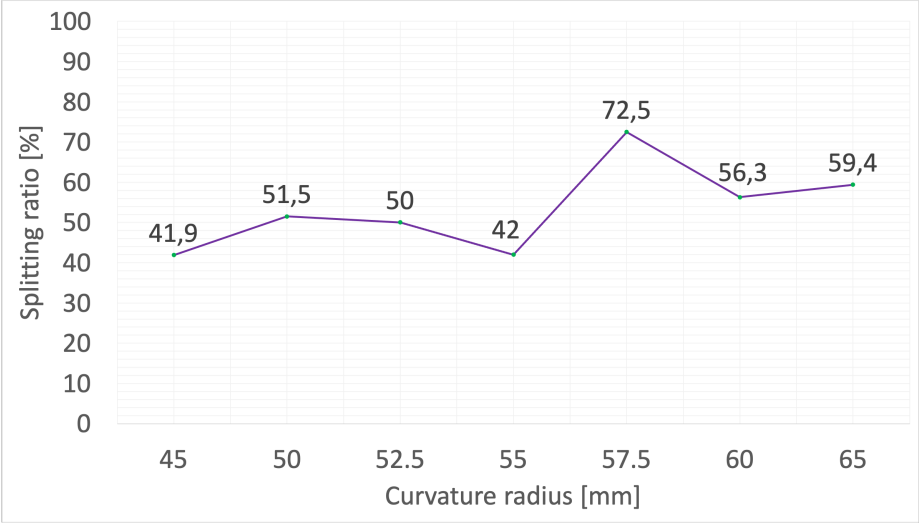

Figure 35: Detuned couplers $v = (39; 41)$ mm s^{-1}, $d = 6$ µm

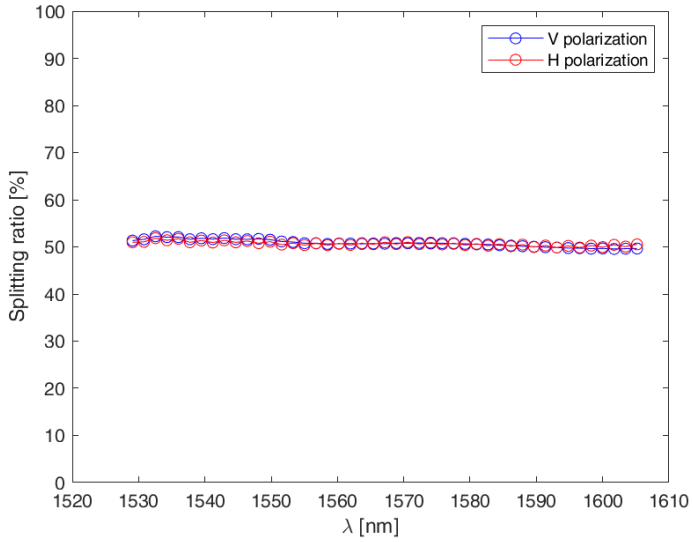

Figure 36: Broadband behavior of polarizations' components of detuned couplers $v = (39; 41)$ mm s^{-1}, $d = 6$ µm and $r = 52.5$ mm.

5 Device fabrication and characterization

The analysis on the single unities constituting the device has lead to adopt a *coupler tree* geometry instead of implementing the Y-junctions, because these have resulted too sensitive to polarization. The directional couplers exhibit the best performances under all points of view, after the study of the many geometric and inscription parameters that should be controlled for obtaining the wanted behavior.

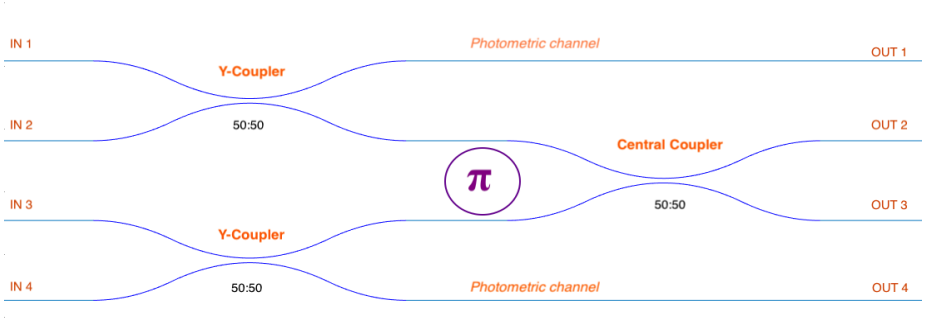

Figure 1: Prototype's geometry. The light enters from two of the four inputs on the left (one for each Y-coupler) and it is split into the photometric channels and to the central coupler, where through a phase shifter the π-phase is imposed, for obtaining the highest extinction.

5.1 Preliminary study and calibration

Once we have collected a lot of information about the directional couplers for various geometries and detuning, the first prototypes could be written. With *prototype* we mean the device without the *fan-in*, i.e. a set of bending waveguides before the device, that shift it with respect to the input waveguides in order to avoid the disturbance of the uncoupled light.
Since this fabrication have been carried out after the Summer's holidays, several couplers in the intervals of interest have been fabricated too. It is important to check the calibration of the fabrication line after a long period of time, moreover the procedure is useful to investigate further potential candidates and to have a comparison for the first prototypes that have been written with the parameters in the previous studies.

5.1.1 Detuned couplers perfomance

The most promising detuned couplers with $L = 0$ mm has been found for $d = 6$ µm and $d = 6.1$ µm with $(v_{low}; v_{high}) = (39; 41)$ mm s^{-1}. The radius has been varied in $r = [50 : 60]$ mm with $\delta r = 0.5$ mm yielding the results shown in Figs. 2 and 3:

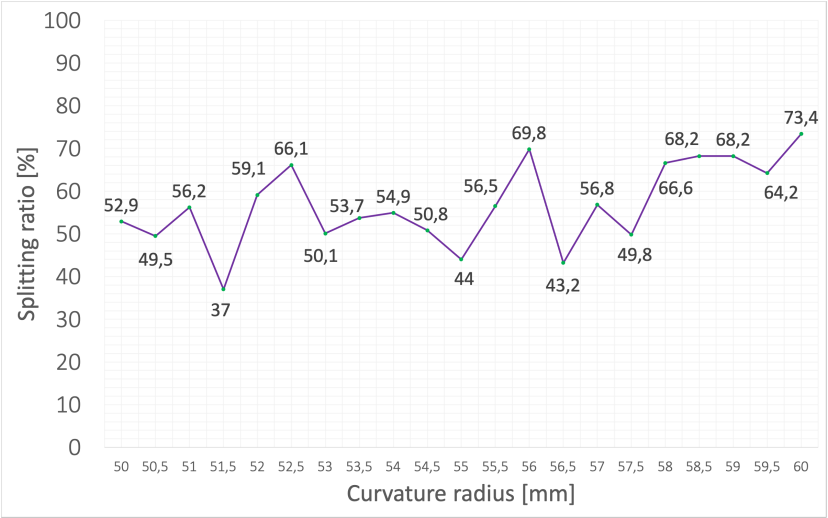

Figure 2: Detuned couplers $L = 0$ mm, $d = 6$ μm, $v = (39; 41)$ mm s^{-1}, tested for close-spaced radii.

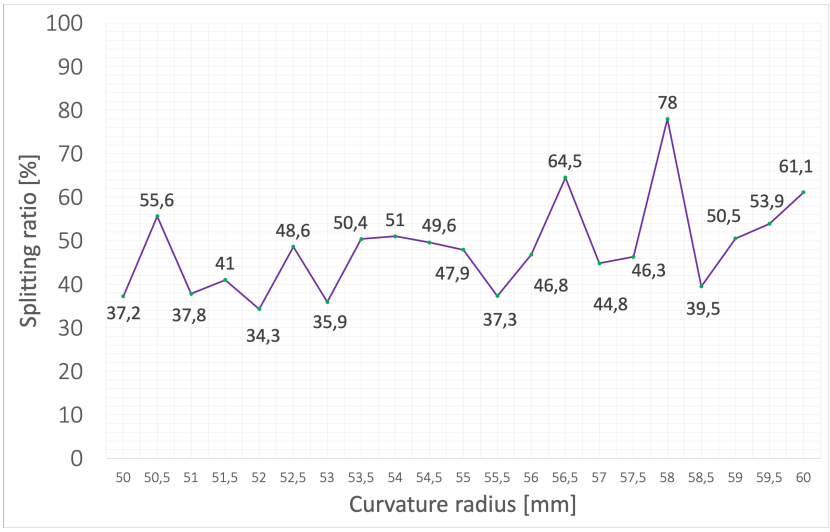

Figure 3: Detuned couplers $L = 0$ mm, $d = 6.1$ μm, $v = (39; 41)$ mm s^{-1}, tested for close-spaced radii.

We could have an idea of the fluctuations occurring due the dense sampling, underlined by the significative differences that can influence the splitting ratio of almost identical couplers. Since the coupling distance is very small, the overlap integral result very extended and therefore the behavior of the splitting ratio will be more sensitive to small differences induce by noise sources.
The fabrication reproducibility after the pause is confirmed: no evident alterations have emerged and we have found a lot of suitable couplers in the investigated interval.

5.1.2 Symmetric couplers performance

In this case the most promising candidates has been found for $d = 6.1$ µm and $d = 6.3$ µm, keeping always $v = 40$ mm s^{-1}. The radius has been varied in $r = [47 : 57]$ mm with $\delta r = 0.5$ mm.

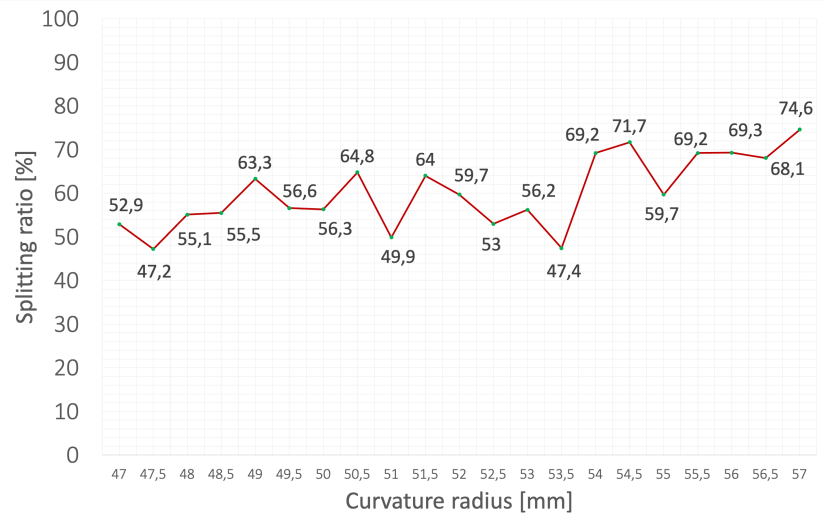

Figure 4: Symmetric couplers L = 0 mm, $d = 6.1$ µm, $v = 40$ mm s^{-1}, tested for close-spaced radii.

We have found less potential couplers for the final device with respect to the detuning case and for $d = 6.3$ µm no balanced couplers have been found.

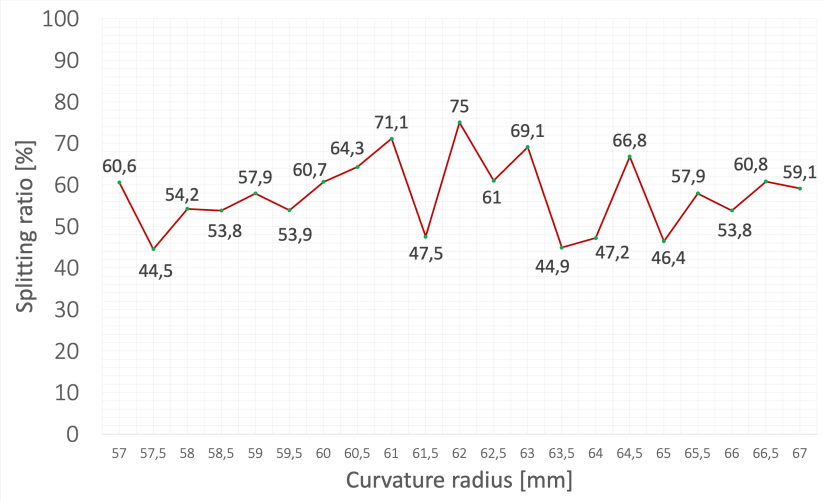

Figure 5: Symmetric couplers L = 0 mm, d = 6.3 µm, v = 40 mm s^{-1}, tested for close-spaced radii.

5.2 Prototypes characterization

The analysis has been carried out injecting light into each arm of the prototype, measuring three spots at the outputs and retrieiving the splitting ratios of each coupler. In particular we tested prototypes composed by couplers with the following features:

Type	d	r	Splitting ratio (before)	Splitting ratio (after)
Detuned	6 µm	52.5 mm	50%	66.1%
Detuned	6.1 µm	55 mm	51.4%	47.9%
Symmetric	6.1 µm	50 mm	48.9%	56.3%

Table 1: L = 0 mm couplers used to compose the first prototypes. The fabrication was based on the splitting ratio values obtained before the pause, whereas the right column shows the effective values of the couplers in the same fabrication of the prototypes. It's worthy to underline that the splitting of the detuned d = 6 µm and r = 53 mm in the prototype fabrication is SR = 50.1%.

Splitting ratio [%]	Y-coupler 1	Y-coupler 2	Central coupler
Input 1:	55.2	-	48.6
Input 2:	46.8	-	46.9
Input 3:	-	79.6	51.6
Input 4:	-	79.1	50

Table 2: Splitting ratios of the detuned prototype d = 6.1 μm, r = 52.5 mm.

Splitting ratio [%]	Y-coupler 1	Y-coupler 2	Central coupler
Input 1:	89.4	-	45.3
Input 2:	87.2	-	44.3
Input 3:	-	64.3	43.3
Input 4:	-	63.3	44.8

Table 3: Splitting ratios of the detuned prototype d = 6.1 μm, r = 55 mm.

Splitting ratio [%]	Y-coupler 1	Y-coupler 2	Central coupler
Input 1:	85.1	-	64.2
Input 2:	76.5	-	63.7
Input 3:	-	78.8	67.5
Input 4:	-	77.8	68.5

Table 4: Splitting ratios of the symmetric prototype d = 6.3 μm, r = 50 mm.

From the overall analysis an unexpected behavior emerges: the splitting ratios are not independent of the inputs, due to probable imperfections during the fabrication process. We would prefer a balanced behavior because we are trying to impose to each coupler a 50:50 splitting. Moreover, the splitting ratio of the Y-couplers result different from central one, although they have been written with the same parameters. This behavior could be correlated to the different writing *order* of the couplers, known as *quill effect*.

5.3 Quill effect

When we have wrote the waveguides, the FLM has followed a precise order and a writing direction, after having scanned three times each waveguide. Experiments showed that inverting the writing direction in an isotropic material can lead to modifications which are not centrosymmetric even if the mode of the femtosecond laser is a gaussian one **[36]**. This could visualized imagining the wavefront of the gaussian mode of the laser that during the writing finds disturbing stressed regions which affect its shape and the plasma formation, inducing different behaviors that in some application could be exploited. In every fabrication we have written before the waveguides at lower velocity, then the higher ones. Changing the writing direction would imply a new optimization of the overall process.

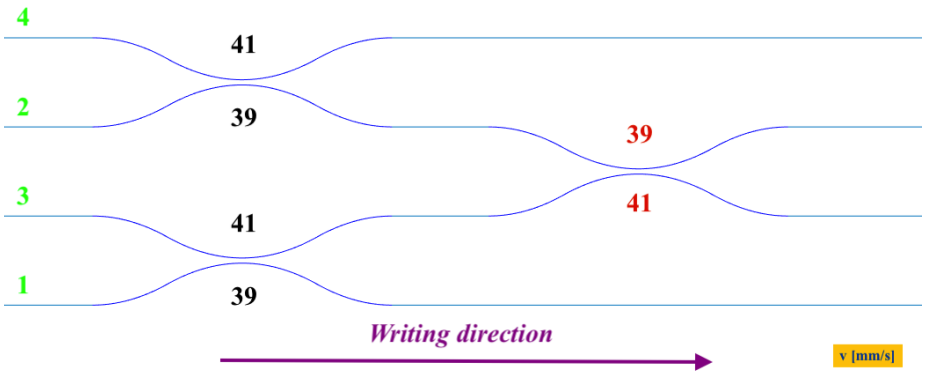

Figure 6: Detuned prototype writing order: in green the absolute waveguide writing order, in black and red are shown the writing velocities expressed in mm s^{-1}.The waveguides with v = 39 mm s^{-1} see an unperturbed glass, but the waveguides written with v = 41 mm s^{-1} are subjected to two different situations: in the Y-couplers they see a modified region at their *right* with respect to the writing direction, whereas in the central one the stressed region lies on the *left*.

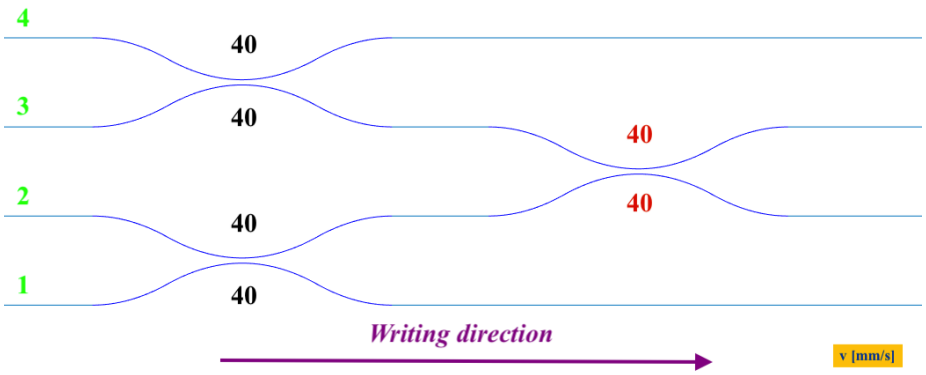

Figure 7: Symmetric prototype writing order: in green the absolute writing order, in black and red are shown the writing velocities expressed in mm s^{-1}. The velocity is the same and each coupler sees the same writing order, in fact from Table 9 we can see that the reflectivity are very close, apart the fluctuation affecting the first input.

As discussed in the previous chapters, we can accept a splitting ratio different from the balance condition for the Y-couplers, because they are used to estimate the input power of the central directional coupler from the measurement of the output power of the photometric channels, so they can be used as soon as they have a known reflectivity and do not subtract too much light from the nulling coupler. Nevertheless, we decided to study this phenomenon by fabricating some directional couplers with a different inscription order.

5.3.1 Inverse couplers

In order to achieve a balanced splitting also for the Y-coupers, in this optimization the v = 41 mm s^{-1} waveguides have still been written after the v = 39 mm s^{-1}, but *down* as the central coupler in Fig. 6, yielding the following results:

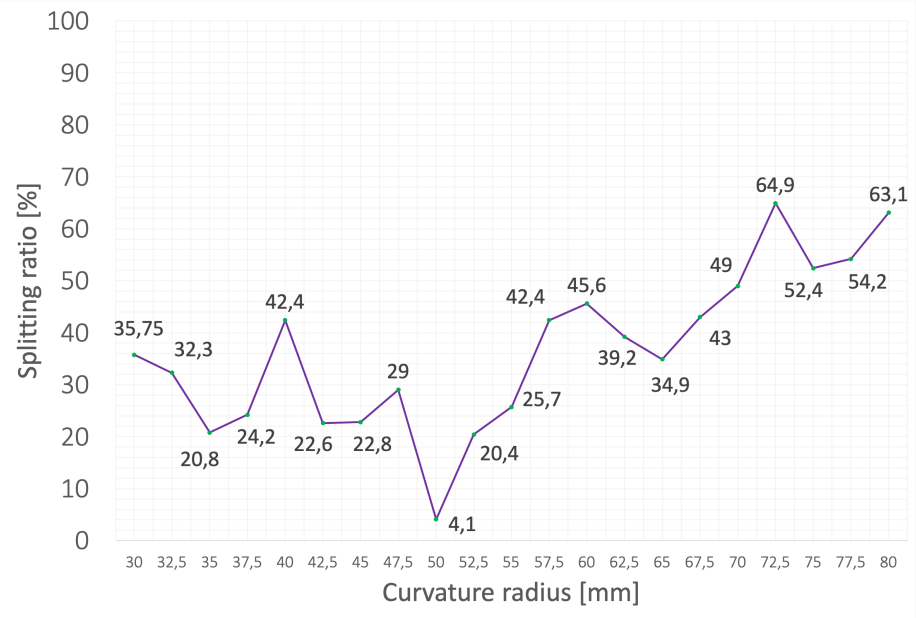

Figure 8: Characterization at λ = 1550 nm of inverse detuned couplers, L = 0, d = 6 µm, v = (39;41) mm s^{-1}.

The behavior has resulted worse with respect the other cases. At higher radii the couplers seem to reach a better response, so the interval r = [70 : 80] mm has been characterized also at λ = 1310 nm. In Fig. 9 are compared the two characterization at λ = 1310 nm and λ = 1550 nm. The values for each radius of curvature are closed for wavelength differing of more than 200 nm: this confirm a good broadband behavior also for this writing configuration.
The same procedure has be done for the couplers at d = 6.1 µm, but this case we are very far from the balanced condition, so the characterization at shorter wavelengths has not been carried out.

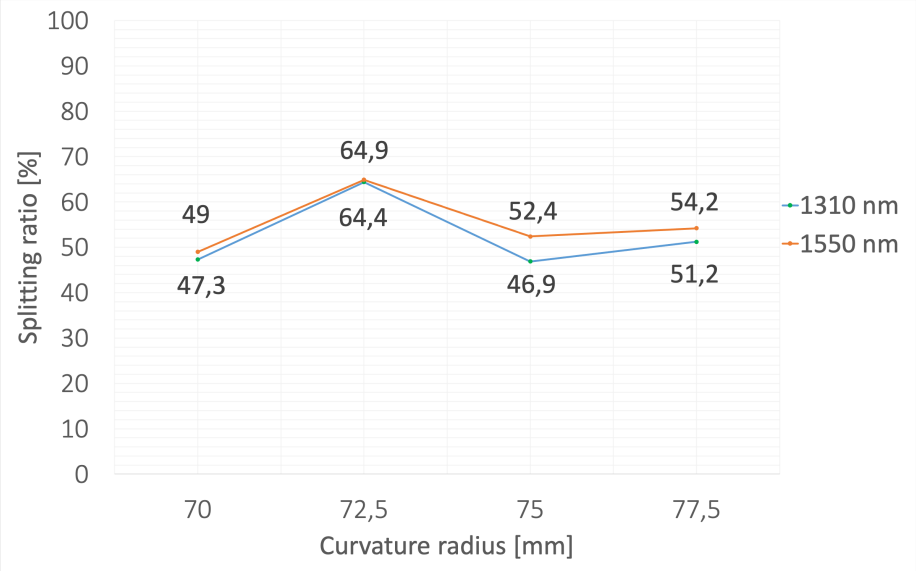

Figure 9: Characterization at λ = 1310 nm (blue) and λ = 1550 nm (orange) of inverse detuned couplers with L = 0, d = 6 μm, v = (39,41) mm s^{-1}. The closed values of the reflectivity evidence a broadband response over more than 200 nm.

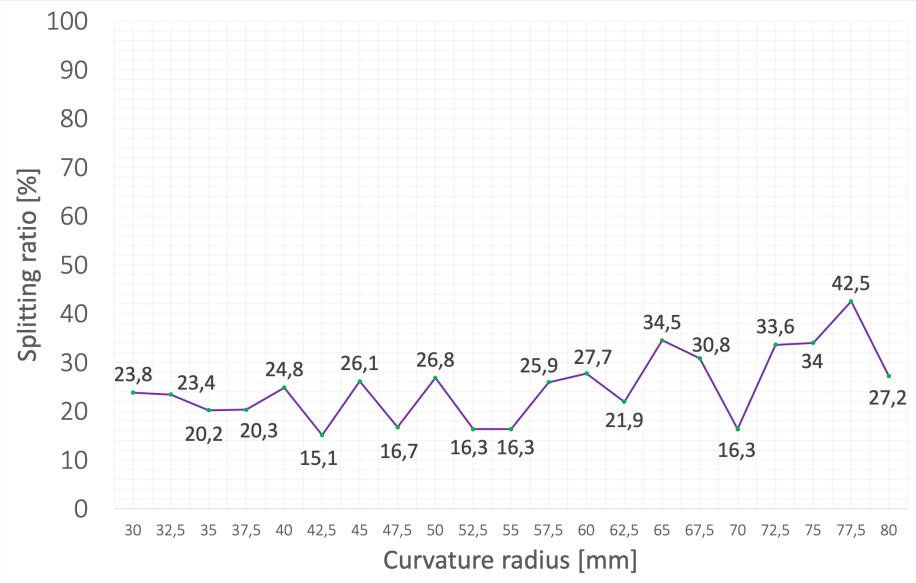

Figure 10: Characterization at λ = 1550 nm of inverse detuned couplers, L = 0, d = 6.1 μm, v = (39;41) mm s^{-1}.

5.4 Fan-in

Before proceeding with the fabrication of the device exploring the new results about the inverse couplers, the fan-in has been implemented. This is a set of bending waveguides before the inputs that shifts the real interferometer 2 mm far from the injection points. The most of the incoming light is confined into the waveguides, but a part remains uncoupled and spreads all around the glass: this can affect negatively the output intensity measure altering the results of the nulling. The distance D between the inputs of the couplers and between the outputs of the fan-in has been fixed to $D = 0.127$ mm, since standard commercial fiber arrays provide this spacing.

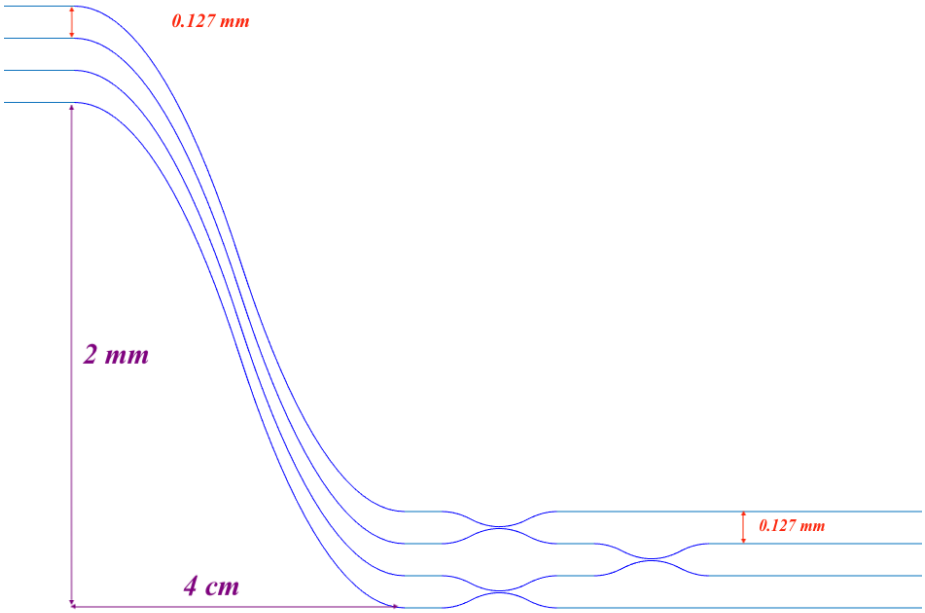

Figure 11: Fan-in representation (not in scale). The 0.127 mm spacing is adopted to allow the coupling with commercial fiber arrays.

5.5 Final device

In the final fabrication several interferometers have been written, paying more attention to the central coupler. For this reason the central coupler has been developed on the basis of the main studies that have been carried on, whereas for the Y-couplers in the detuned case inverse couplers have been tried in a small range of radii $r = [70, 72.5, 75]$ mm.

5.5.1 Detuned interferometers

In the detuned case only the $d = 6$ μm has been investigated, since the ultimate couplers results had excluded the possibility to get a balanced inverse coupler for $d = 6.1$ μm keeping the parameters that have been deepen into this work.
The detuned interferometers have been written in the following order:

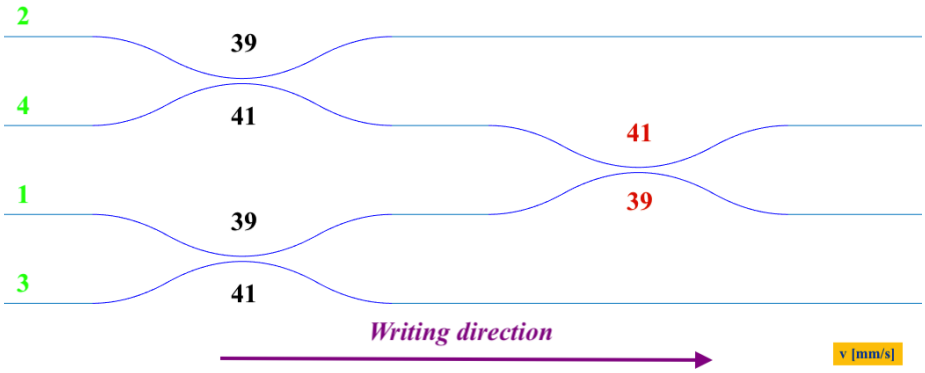

Figure 12: Detuned interferometer writing order: in green the absolute writing order, in black and red are shown the writing velocities expressed in mm s^{-1}. The fan-in is not showed in the picture.

in this way the central coupler is written with the parameters we have investigated the most, whereas the Y-couplers have been written in the inverse modality, varying the curvature radius: for each valid candidate among the central couplers three radii of the Y-couplers have been tested in a symmetric geometry. We have imposed for the central coupler $r_C = [50 : 51]$ mm and $r_C = [52.5 : 55]$ mm in $\delta r = 0.5$ mm, and for each one a Y-coupler with $r_Y = [70, 72.5, 75]$ mm.
The characterization has been done directly with a fixed polarization testing both the 2^{nd} and 3^{rd} input: in this way we could retrive the splitting ratio of the central coupler hoping to find two values as close as possible to 50:50. In case, the other polarization and the other inputs would have been checked.

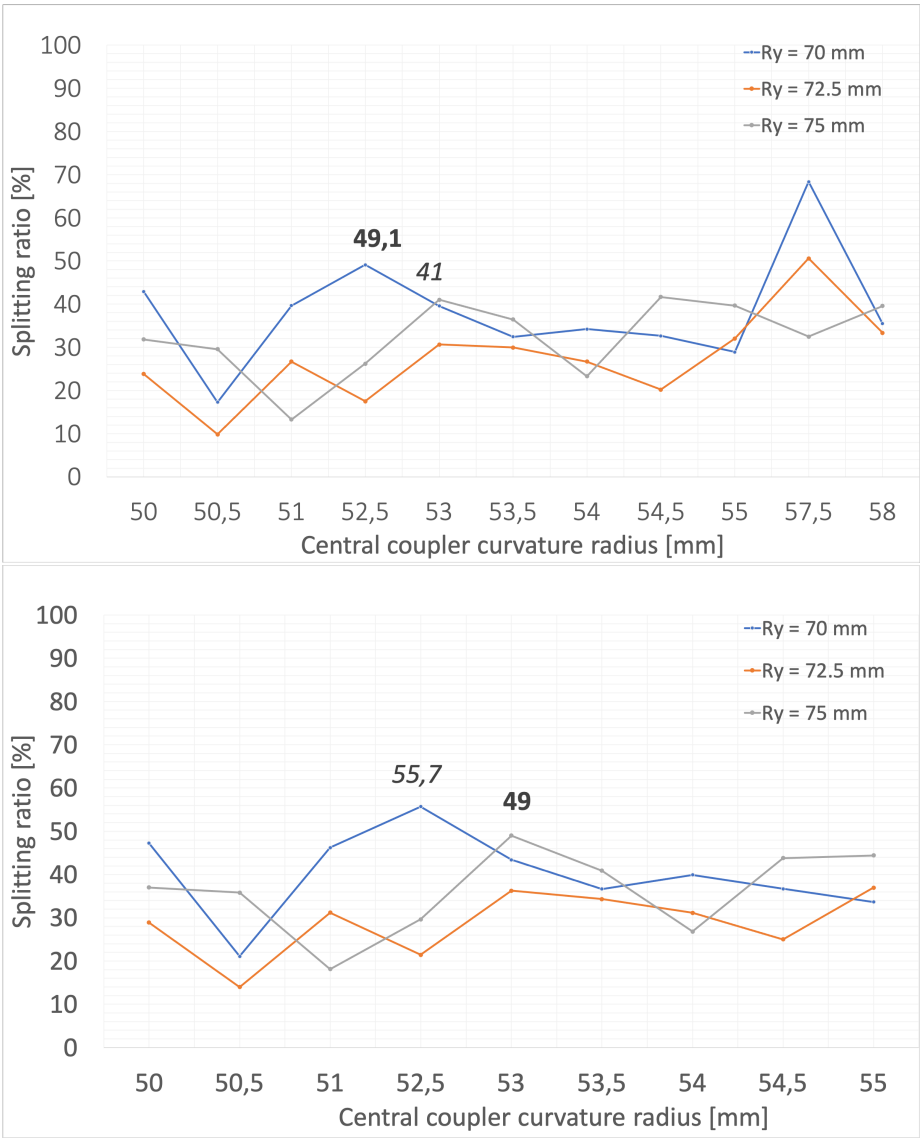

Figure 13: Central coupler's splitting ratio dependence on r_C and r_Y, for vertical polarization. *Up*: light is injected into the second input; *down*: light is injected into the third input. In bold the closest reflectivity to the balanced condition, in italics the correspondent value for the other input.

Although we can appreciate the same qualitative trend depending on the input, only two interesting values have been found, but for different radii of the central coupler: the difference in splitting ratio results excessive, being for $r = 52.5$ mm 49% (2) vs 55.7% (3) and for $r = 53$ mm 41% (2) vs 49% (3).

5.5.2 Symmetric interferometers

The symmetric interferometers do not show the quill problem, because we can exploiting a more uniform writing order among the waveguides. Two groups have been fabricated: one with $d = 6.1$ μm and $r = [47 : 54]$ mm in $\delta r = 1$ mm, the other with $d = 6.3$ μm and $r = [60 : 80]$ mm with $\delta r = 2.5$ mm. The radii of the central coupler and of the Y-couplers have been kept equal. Also in this case the light vertically polarized beam has been injected into the 2^{nd} and 3^{rd} inputs.
The two inputs of the couplers at $d = 6.1$ μm (Fig. 14) show the same qualitative trend, but the differences in splitting ratio are quite high, being between $5 - 7\%$.
For $d = 6.3$ μm instead (Fig. 15) at $r = 80$ mm we have found a symmetric interferometer that can bring to the central coupler the 50.3% of light injected from input 2 and the 51.8% from input 3. This is the best performance achieved among all fabrication, establishing a splitting ratio difference of $\sim 2\%$.
The complete characterization of this last device can be carried out, testing the polarization behavior of each input:

V polarization: Splitting ratio [%]	Y-coupler 1	Y-coupler 2	Central coupler
Input 1:	32.2	-	50.9
Input 2:	26.5	-	50.4
Input 3:	-	35.8	51.8
Input 4:	-	43.2	51.6

Table 5: Splitting ratios of the symmetric interferometers $d = 6.3$ μm, $r = 80$ mm, for V polarized input light.

H polarization: Splitting ratio [%]	Y-coupler 1	Y-coupler 2	Central coupler
Input 1:	33.3	-	51.7
Input 2:	27.3	-	51.5
Input 3:	-	36.8	53
Input 4:	-	44.5	52.8

Table 6: Splitting ratios of the symmetric interferometers $d = 6.3$ μm, $r = 80$ mm, for H polarized input light.

The best inputs are the 1^{st} and the 4^{th}, because in this way more light is brought to the central coupler, and the splitting is comparable. Therefore these has be used to characterize the device. The band analysis has shown the results shown in Figs. 16 and 17.

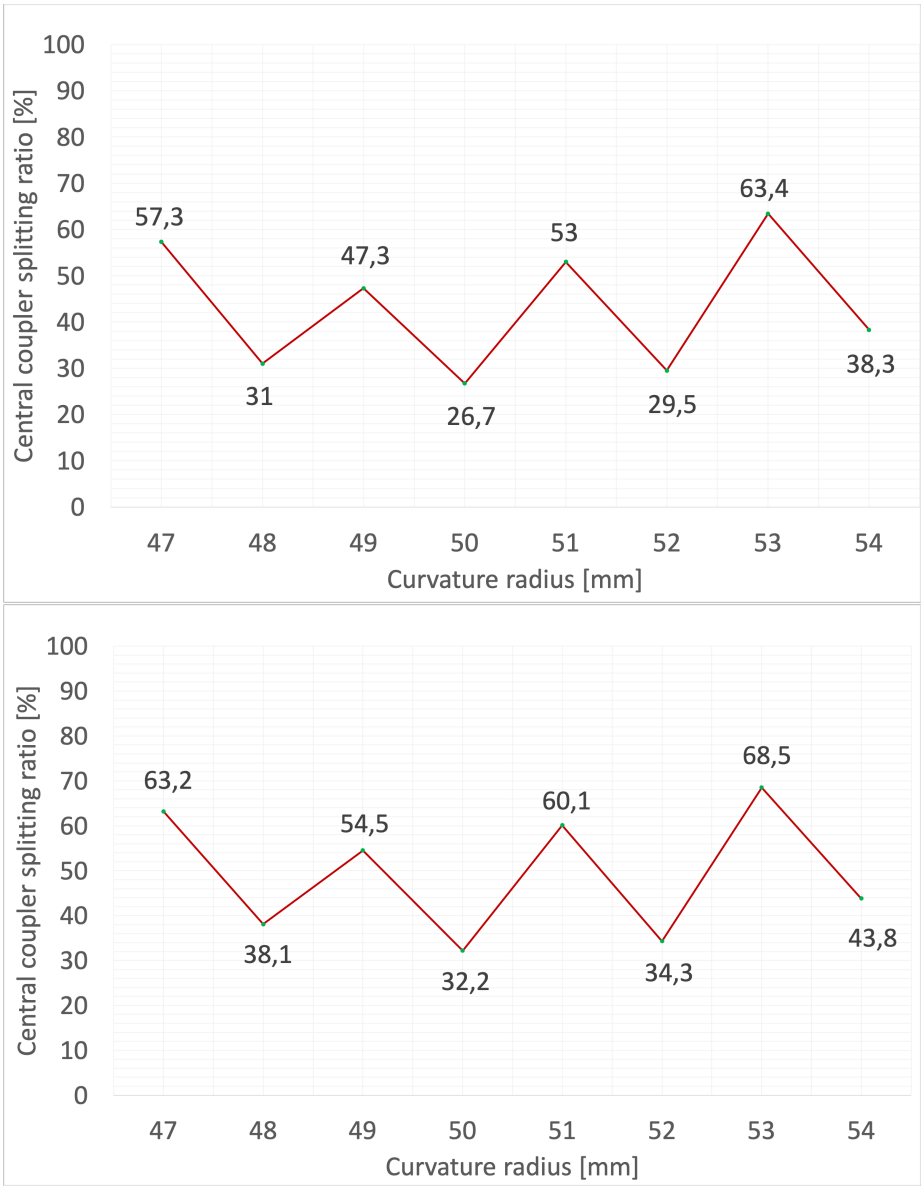

Figure 14: Splitting ratio of the central coupler according to the 2^{nd} input (up) and 3^{rd} (down) for symmetric interferometers with d = 6.1 μm, tested for several curvature radii. L = 0 mm, v = (40 ; 40) mm s^{-1}.

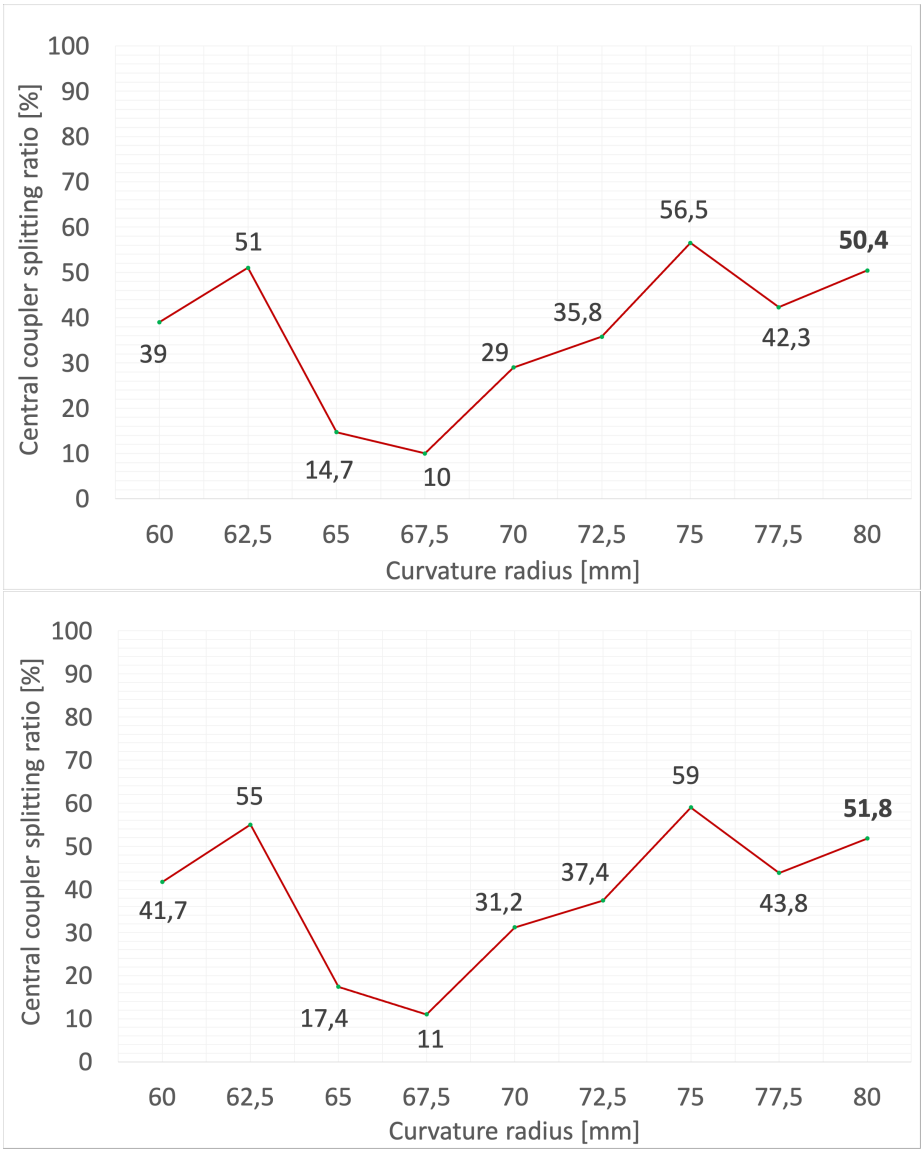

Figure 15: Splitting ratio of the central coupler according to the 2^{nd} input (up) and 3^{rd} (down) for symmetric interferometers with d = 6.3 µm, tested for several curvature radii. L = 0 mm, v = (40 ; 40) mm s^{-1}.

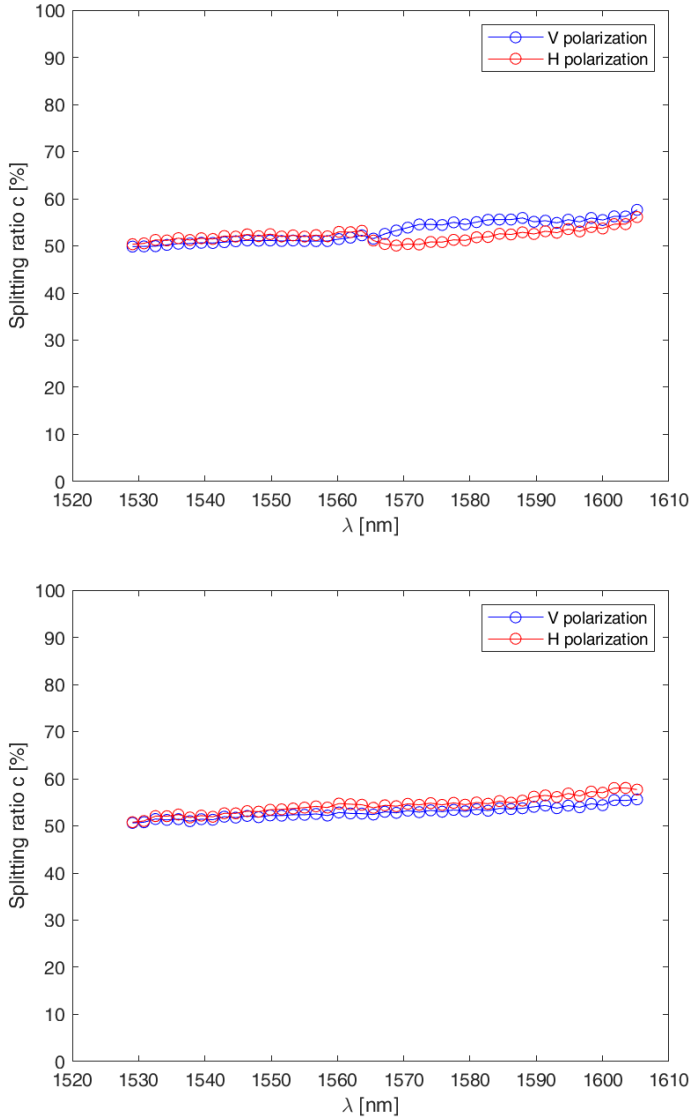

Figure 16: Splitting ratio of the central coupler according to polarization, injecting light in the 1^{st} input (up) and the 4^{th} (down).

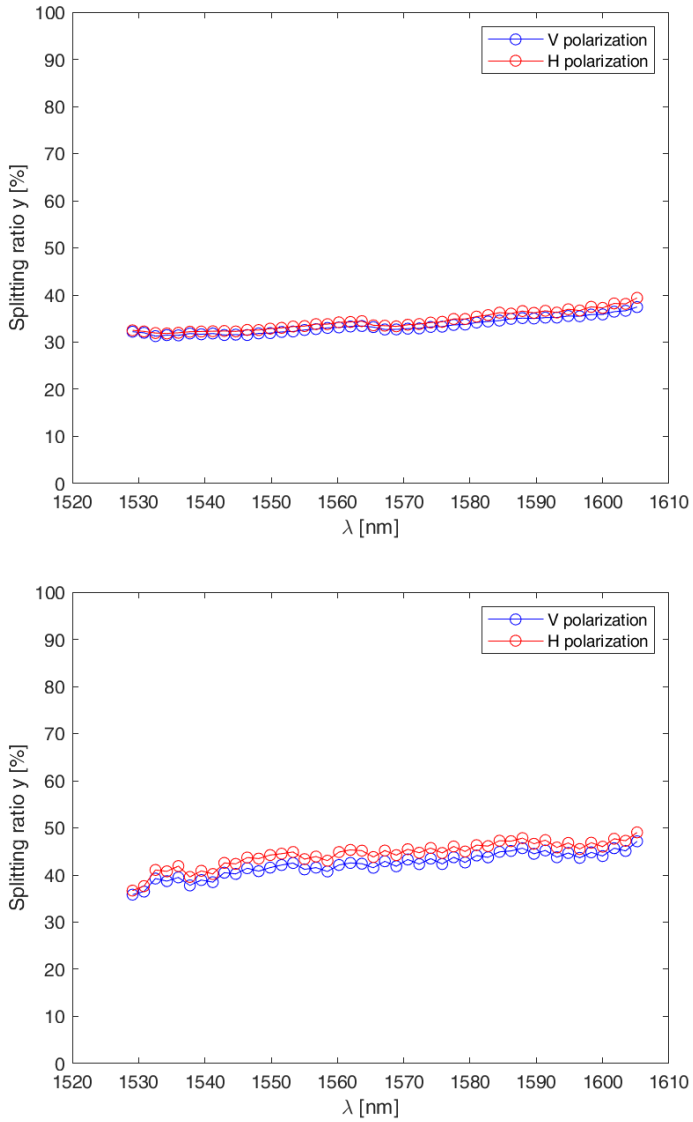

Figure 17: Splitting ratio of the Y- couplers according to polarization, injecting light in the 1^{st} input (up) and the 4^{th} (down).

The obtained results are slightly worse than the ones obtained during the optimization process, however they are still good for guaranteeing a broadband behavior of the device. Indeed, the fluctuation of 5% over 80 nm should not affect the nulling ratio of the device, and is far better than the results obtained in literature at 1550 nm.
The band behavior has been tested also with a characterization at $\lambda = 1310$ nm: in this way we have investigated a broadband of $\Delta\lambda = 300$ nm, three times the operational requirement.

V polarization: Splitting ratio [%]	Y-coupler 1	Y-coupler 2	Central coupler
Input 1:	32.2	-	50.9
Input 2:	26.5	-	50.4
Input 3:	-	35.8	51.8
Input 4:	-	43.2	51.6

Table 7: Splitting ratios of the symmetric interferometers at $\lambda = 1310$ nm. $d = 6.3$ μm, $r = 80$ mm, for V polarized input light.

5.6 Star simulation: modified Michelson interferometer

In order to test the functionality of the nulling interferometer, it is necessary to provide to the two inputs a coherent beam and implement a phase control, which in the complete design is carried out in a very precise way by the phase-shifters. To simulate these and to have a first raw estimation of the nulling ratio, we set up a bulk Michelson interferometer in a modified geometry: we are not interested in nulling the light as in the Michelson experiment, instead we want to provide to the device two identical coherent beams, therefore a mirror is substituted with a converging lens, and a phase delay has been put in one through a translational stage to play the role of the phase-shifter.

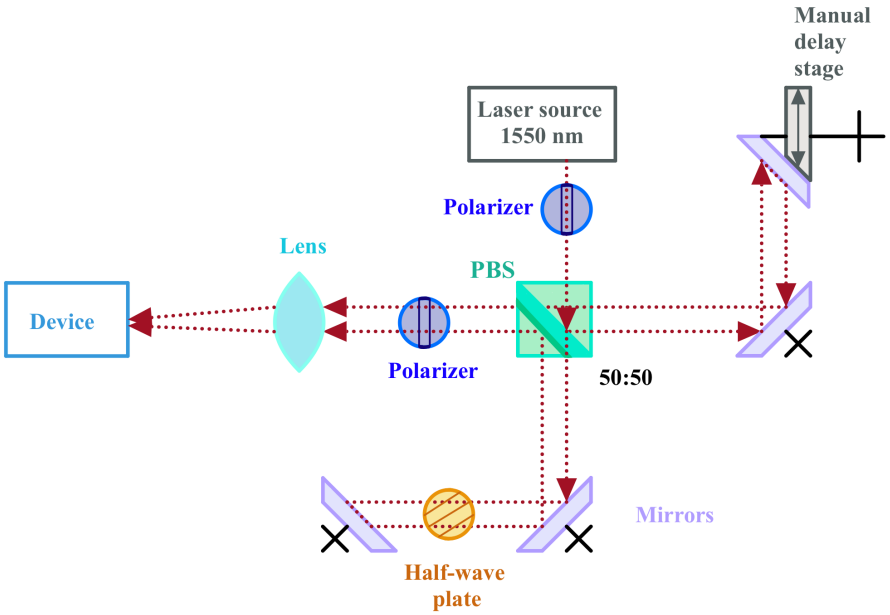

Figure 18: Graphic representation of the modified Michelson interferometer setup. A coherent beam is generated by the laser diode at $\lambda = 1550$ nm, it passes through a polarizer and reaches a polarized beam splitter, which splits the light 50:50. A manual delay stage is mounted at the right side, controlling the relative phase of the beams. In the bottom, the reflected light beam passes through an half-wave plate that in concert with the polarizer before the lens allow to attenuate it to calibrate the photometric channels intensity. The lens focalizes the beams into the inputs of the device, with the help of the mirrors.

.

The delay stage affects only one beam, changing its phase with respect to the other one. As shown in Fig. 19, the two beams are still able to interfere since the induced path difference is much lower than the coherence length of the laser diode. If the relative phase is $\Delta\phi = \pi$, the light is completely nulled in one channel (ideal case), so the

filtering action succeeds.

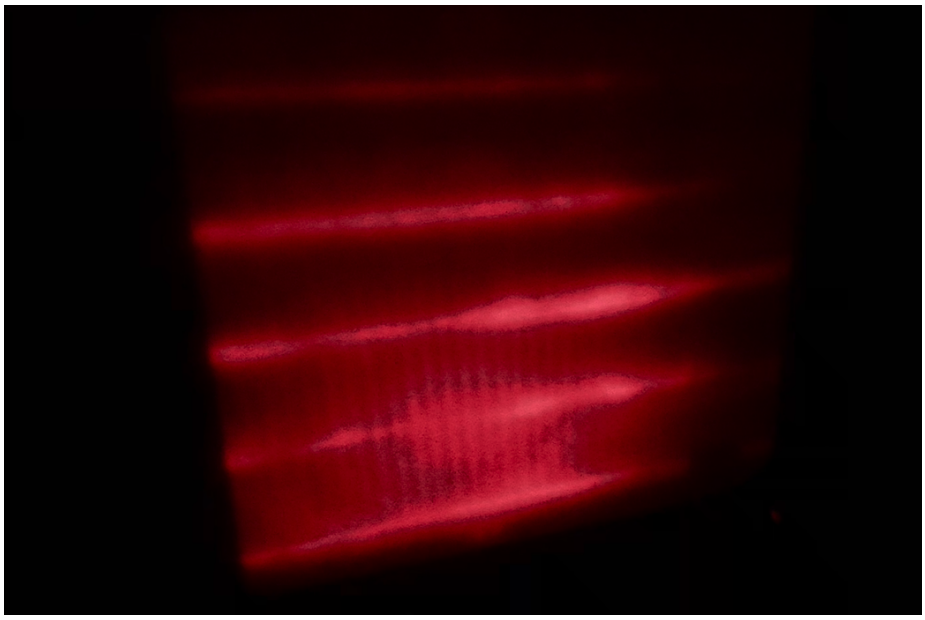

Figure 19: Fringe pattern on a IR sensitive card. The horizontal lines are due to the light reflection on the sample interfaces, wheres the vertical fringes resemble the Young's experiment, as the two outputs of the interferometer behaves as point-like sources.

At the output of the interferometer, an IR-camera is placed to measure with high accuracy the intensity of the four peaks. According to the characterization analysis and calling the photometric channels P and Q, from the values of the reflectivity of the Y-couplers we can retrieve their intensity ratio in order to get a balanced power injection into the central coupler:

$$R_P = 32\%$$

$$R_Q = 43\%$$

$$\frac{68}{32} I_P = \frac{57}{43} I_Q$$

$$I_P \sim 62\% I_Q.$$

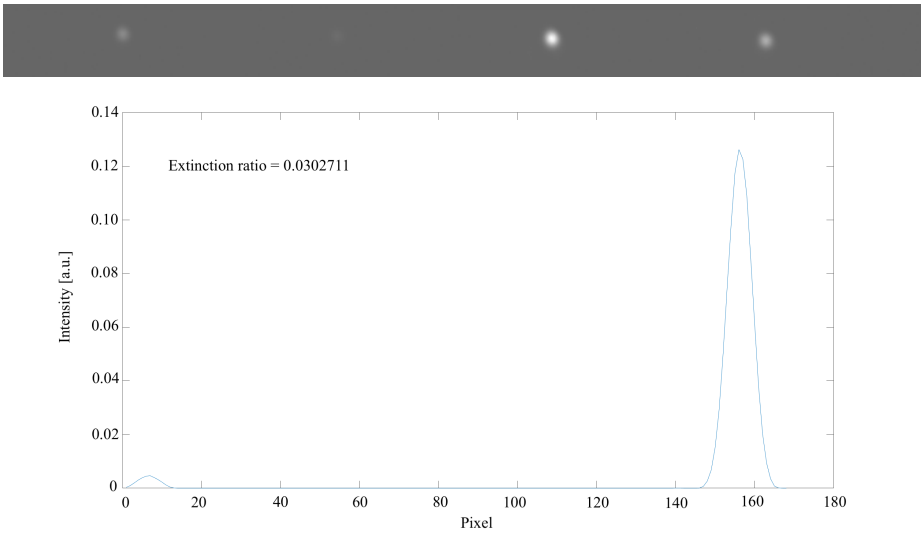

Figure 20: The pictures show a phase conditions leading to null the second channel. *Up*: spots captured by the camera. *Down*: intensity peaks profiles. The control of the intensity of the photometric channel is done exploiting an half-wave plate and the polarized by hand.

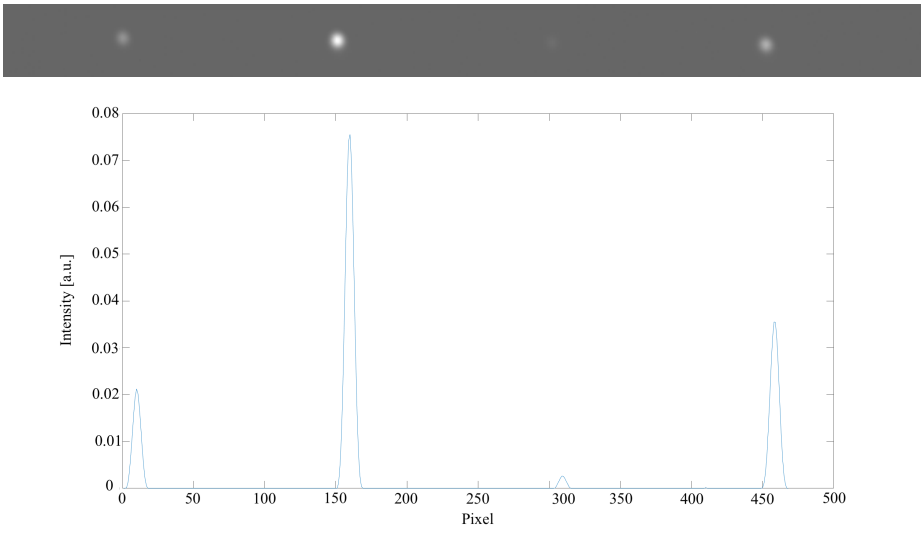

Figure 21: The pictures show a phase conditions leading to null the third channel. *Up*: spots captured by the camera. *Down*: intensity peaks profiles.

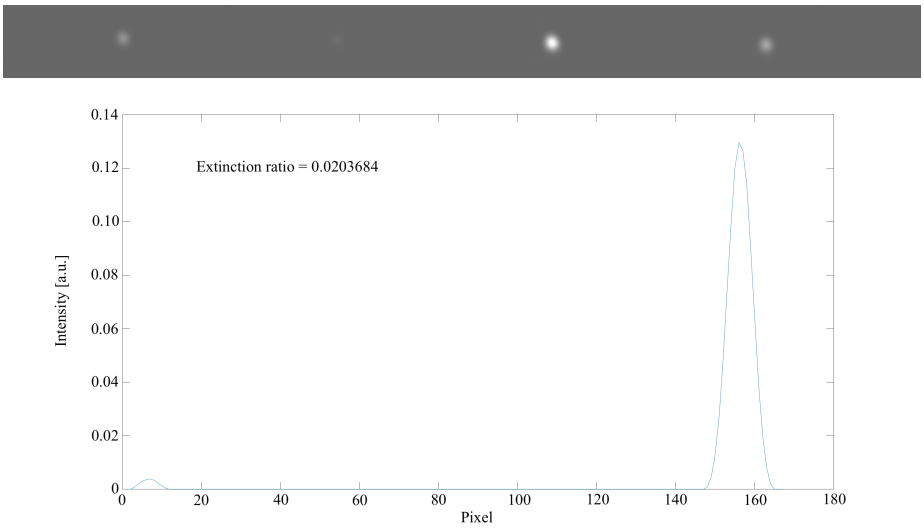

Figure 22: Final nulling ratio achieved in the characterization with the modified Michelson interferometer setup.

Focusing on the centrals peaks, we have obtain a minimum nulling ratio of the order of 10^{-2}. This value shows that the nulling interferometer works, but the setup resulted too rudimental to obtain the best performance achievable by the device. An optimum extinction ratio would require a much higher control of the relative phase and on the power injection ratio. The resolution of a manual stage delay is insufficient, moreover the overall setup is sensitive to vibration of the environment.
A more precise measurement can be achieved implementing thermal phase shifters on the device and controlling the power injection ratio through an integrated Mach-Zehnder interferometer supported by an other phase shifter.

5.7 Thermal phase shifter

Thermal phase shifters allow to modify locally and not permanently the refractive index of a waveguide, exploiting the thermo-optical effect **[46]**. The temperature of the waveguide is modulated by a resistive microheater, resulting in a change of the propagation constant and therefore in a phase control. The phase shifters are realized depositing a thin film of gold on the chip surface, which is subsequently ablated to pattern the resistor, the metal interconnections and the contact pads.

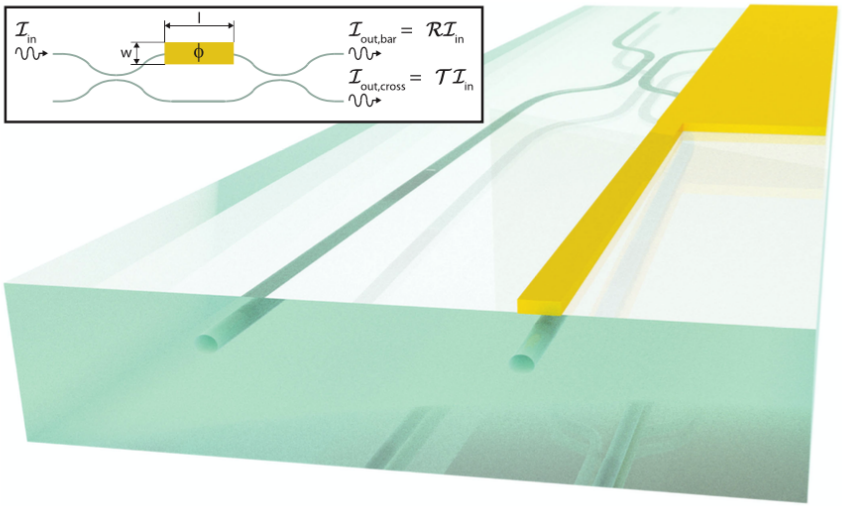

Figure 23: Phase shifter implementation on a Mach-Zehnder integrated interferometer. The gold layer represent the resistor that locally heats an arm of the MZI to tune its the reflectivity **[46]**.

Part of the fabrication will be carried out in the PoliFab cleanroom, the micro-nanofabrication facility of Politecnico di Milano. The fabrication process will follow an already optimized recipe, consisting in the following steps:

1. Deposition of a thin film of chromium (t = 2 nm) to improve the adhesion of the gold layer. The film must be sufficiently thick to guarantee the adhesion of the gold layer, but at the same time the diffusion of chromium ions must be avoided ($T \sim 200$ °C), that would result in a drift of the resistivity of the phase shifter.

2. Deposition of the gold layer (h = 100 nm). This allow to realize a the thermal shifter resistance of R_{ts} = 50 Ω, with an operating voltage ΔV = 5 V and a current of I = 100 mA, for a microheater dissipation of P = 500 mW. These values are sufficient to obtain a complete shift of the optical signal for an integrated Mach-Zehnder interferometer.

3. Ablation of the film with a femtosecond laser, the same used to inscribe the waveguides.

4. Thermal annealing treatment to improve the growth of grains of the polycrystalline film, reaching a single-crystal state and avoiding the growth during the thermal shift operation of the device. The annealing temperature reaches T = 400 °C, far below the strain point of the glass, without affecting the waveguides.

5. Mounting of the pin headers and connection to the contact pads with an epoxy electrical conductive glue.

In Fig. 24 is shown the design of the ablation on the final chip. 1 and 2 represent two contacts of two resistances, that in concert increase the phase control and assure the presence of a substitute in case of damage. Applying a voltage difference between 1 and the mass will result in a flow of current and local heating of the waveguide below the rectangle, whereas a voltage in 2 heats the waveguide above.
The resistance upon the waveguides is expressed by:

$$R_{ts} = R_{layer}\frac{l}{w},$$

where R_{layer} is the sheet resistance of the gold film, l is the length of the resistance and w its width. The portions of gold between the ablations on the waveguides constitute a portion of gold where the width is minimal, increasing in that point the power dissipation and performing the phase shift. The rest of the layer can be considered not affected. Moreover, a crosstalk between the resistances must be avoided: the red rectangle in Fig. 24 represents an ablation with this task. The crosstalk can reduce drastically the phase shift capability, requiring higher power dissipation; moreover the resistances can be damage by the reciprocal heating, which follow a non linear behavior with respect to the power.

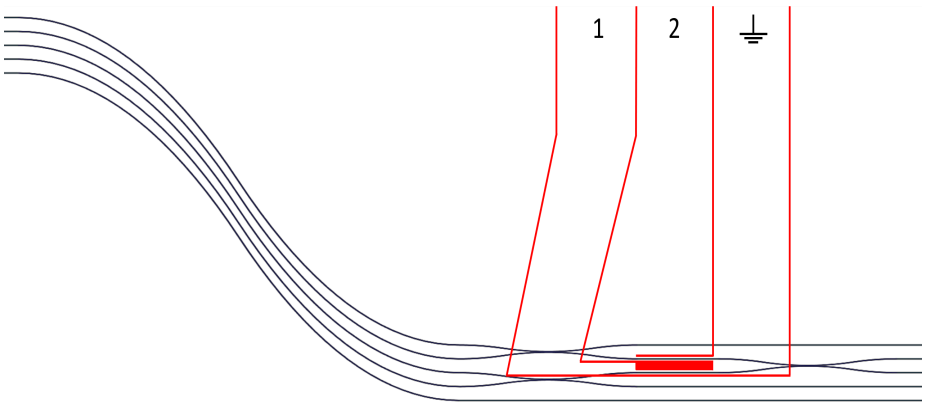

Figure 24: Design of the thermal phase shifter on the nulling interferometer. 1 and 2 represent the contacts of two resistances, the red lines and the rectangle show the ablation of the gold layer. In the design l = 4 mm.

6 Conclusions and future perspectives

In this thesis work we presented the design and fabrication of an integrated nulling interferometer, with application in the detection of exoplanets. The hearth of this device was a directional coupler combining the light collected by two telescopes, in order to perform the destructive interference of the starlight and leave only the signal of the planet. Since the celestial light is unpolarized, the device response needed to be independent of the polarization of the incoming light. For its fabrication we exploited therefore the Femtosecond Laser Micromachining technique followed by a thermal annealing treatment. This fabrication process is indeed capable of providing high quality integrated photonic circuits, with a birefringence of the order of 10^{-6} and propagation losses below 0.2 dB cm^{-1}. The first part of this work was therefore devoted to the optimization of the fabrication, for obtaining a low-loss single mode waveguide at 1550 nm. After a fine tuning of some inscription parameters, like translation speed, laser power and number of scans, the best waveguide showed propagation losses of 0.15 dB cm^{-1} and negligible bending losses down to a radius of curvature of 20 mm. For confirming the polarization insensitivity of the inscribed circuits, we fabricated some directional couplers and characterized them with different polarization states, finding deviations of the splitting ratio lower than 2%.

The second part of the work was instead focused on obtaining a broadband operation. Indeed, a wavelength independent circuit would not need bandpass filters, which would further reduce the already faint exoplanet light. For this purpose, we fabricated directional couplers with a very low coupling distance between the waveguides and a zero-interaction length, since these characteristics have been demonstrated in literature to reduce the wavelength dependence of the splitting ratio. Moreover, we investigated the possibility of inducing a detuning between the waveguides for further flattening the curve. Despite the fabrication process became less reproducible, we were able to obtain directional couplers that showed a variation of the splitting ratio below 5% in a 300 nm band, much broader than the band of operation of the final device.

With these promising results, we fabricated the integrated interferometer. We implemented the possibility of measuring the input light of the directional coupler by adding two photometric channels, that collect a fraction of the input light by means of two additional broadband and polarization-insensitive directional couplers. By injecting light in both the two input waveguides of the device, and by controlling the phase difference between them, we were able to obtain a nulling ratio of $2\ 10^{-2}$.

In the future, the fabrication of thermal phase shifters on top of the waveguides will allow a more reproducible and controllable tuning of the phase difference between the inputs, further reducing the nulling ratio. Moreover, additional investigations will be performed on obtaining a more reproducible fabrication, still preserving the broadband operation of the directional couplers: for instance, either a different focusing objective or a different laser wavelength could be used. Solving this issue would allow to obtain more reproducible directional couplers, enhancing the possibility to achieve a balanced splitting ratio and increase the extinction capability of the device.

7 References

[1]: Barnaby Norros and Joss Bland-hawthorn, *Astrophotonics The Rise of Integrated Photonics in Astronomy*, Optics and Photonics News, May 2019.
[2]: www.nasa.gov.
[3]: R. L. Akenson, X. Chen, D. Ciardi, M. Crane, J. Good, M. Harbut, E. Jackson, S. R. Kane, A. C. Laity, S. Leifer, M. Lynn, D. L. McElroy, M. Papin, P. Plavchan, S. V. ramírez, R. Rey, K. Von Braun, M. Wittman, M. Abajian, B. Ali, C. Beichman, A. Beekley, G. B. Berriman, S. Berukoff, G. Bryden, B. Chan, S. Groom,C. Lau, A. N. Payne, M. Regelson, M. Saucedo, M. Schmitz, J. Stauffer, P. Wyatt And A. Zhang, *The NASA Exoplanet Archive: Data and Tools for Exoplanet Research*, 2013 July 19.
[4]: Micheal Perryman: *The exoplanet handbook*, second edition, Cambrige University Press.
[5]: Steven Soter: *What is a planet?*, The Astronomical Journal,American Astronomical Society, 2006 January.
[6]: Nikku Madhusudhan, Kanani K. M. Lee, and Olivier Mousis, *A possible carbon-rich interior in super-earth 55 Cancri e*, The Astrophysical Journal Letters, 2012 November 10.
[7]: Edward W. Schwieterman, Nancy Y. Kiang, Mary N. Parenteau, Chester E. Harman, Shiladitya DasSarma, Theresa M. Fisher, Giada N. Arney,Hilairy E. Hartnett, Christopher T. Reinhard, Stephanie L. Olson,Victoria S. Meadows, Charles S. Cockell, Sara I. Walker, John Lee Grenfell, Siddharth Hegde, Sarah Rugheimer, Renyu Hu, and Timothy W. Lyons, *Exoplanet Biosignatures: A Review of Remotely Detectable Signs of Life*,Astrobiology,Mary Ann Liebert Inc, 2018 June.
[8]: Stephen Joseph Messenger, *Detectability of Biosignature Gases in the Atmospheres of Terrestrial Exoplanets*, Massachusetts Institute of Technology 2013.
[9]: Jason T. Wright, *Radial Velocities as an Exoplanet Discovery Method*, Handbook of Exoplanets, Springer International Publishing, 2018.
[10]: Barnaby R. M. Norris, Nick Cvetojevic, Tiphaine Lagadec, Nemanja Jovanovic, Simon Gross, Alexander Arriola, Thomas Gretzinger, Marc-Antoine Martinod, Oliver Guyon, Julien Lozi, Michael J. Withford, Jon S. Lawrence and Peter Tuthill, *First on-sky demonstration of an integrated-photonic nulling interferometer: the GLINT instrument*, Monthly Notices of the Royal Astronomical Society, Oxford University Press, 2019 November 23.
[11]: C. Broeg and A. Fortier and D. Ehrenreich and Y. Alibert and W. Baumjohann and W. Benz and M. Deleuil and M. Gillon and A. Ivanov and R. Liseau and M. Meyer and G. Oloffson and I. Pagano and G. Piotto and D. Pollacco and D. Queloz and R. Ragazzoni and E. Renotte and M. Steller and N. Thomas and the CHEOPS team, editor Roberto Saglia, *CHEOPS: A transit photometry mission for ESA's small mission programme*, 2013 April 25.
[12]: Vladimir V. Mitin, Dmitry I. Semenstov and Nizami Z. Vagidov, *Quantum Mechanics for Nanostructures*, Cambridge University Press, 2010.
[13]: Andreas Glindemann, *Principles of Stellar Interferometry*, Astronomy and astrophysics library, Springer, 2010.
[14] :Ronald N. Bracewell And Robert H. Macphie, *Searching for Nonsolar Planets*, Academic Press Inc.,1978 September 18.

[15]: Pavel Gabor. *A study of the performance of a nulling interferometer testbed preparatory to the Darwin mission*. Astrophysics [astro-ph]. Université Paris Sud - Paris XI, 2009. English. tel-00439669.
[16]: Bertrand Mennesson and Jean Marie Mariotti, *Array Configurations for a Space Infrared Nulling Interferometer Dedicated to the Search for Earthlike Extrasolar Planets*, Academic Press, ICARUS 128, 202–212 (1997) Article No. IS975731.
[17]: M. M. Colavitaa, P. N. Swanson, A. F. Boden, S. L. Cratiorda, A. B. Meinela, M. Shao, G. T. van Bellea, G. Vasishta, J. K. Wallace, P. L. Wizinowichb, J. M. Walkerb, Jet Propulsion Laboratory, California Institute of Technology, Pasadena, CA 91109, W. M. Keck Observatory, California Association for Research in Astronomy, Kamuela, HI 96743,04/26/98.
[19]: J. R. P. Angel And N. J. Woolf, *An Imaging Nulling Interferometer To Study Extrasolar Planets*, The Astrophysical Journal, 475:373-379, 1997 January 20.
[20]:Naoshi Baba, Naoshi Murakami, and Tsuyoshi Ishigaki, *Nulling interferometry by use of geometric phase*, August 1, 2001 / Vol. 26, No. 15 / Optics Letters.
[21]: Marc Ollivier, Jean-Marie Mariotti, Alain Léger, Predrag Sékulic, Jacqueline Brunaud, Guy Michel, *Nulling interferometry for the DARWIN space mission*, 2001 Académie des sciences/Éditions scientifiques et médicales Elsevier SAS.
[22]: www.keckobservatory.org.
[23]: J.M. Le Duigou, M. Olliver, A. Léger, F. Cassaing, B. Sorrente, B. Fleury, G. Rousset, O. Absil, D. Mourard, Y. Rabbia, L. Escarrat, F. Malbet, D. Rouan, R. Clédassou, M. Delpech, P. Duchon, B. Meyssugnac, P.-Y. Guidotti, N. Gorius, *Pegase: a space-based nulling interferometer*, John C. Mather and Howard A. MacEwen and Mattheus W. M. de Graauw, SPIE, 2006.
[24]: Giacomo Corrielli: *Integrated photonic circuits by femtosecond laser writing for qubit manipulation, quantum cryptography and quantum-optical analogies*, Doctoral dissertation, Politecnico di Milano, 2015.
[25]: Thomas Gretzinger,Simon Gross, Alexander Arriola, And Michael J. Withford, *Towards a photonic mid-infrared nulling interferometer in chalcogenide glass*, OPTICS EXPRESS,18 Mar 2019.
[26]: Giacomo Corrielli,Simone Atzeni, Simone Piacentini, Ioannis Pitsios, Andrea Crespi, And Roberto Osellame, *Symmetric polarization-insensitive directional couplers fabricated by femtosecond laser writing*, Optical Society of America,Optics EXPRESS, 2018.
[27]: P. Gondoina, O. Absilc, R. den Hartoga, R. Wilhelmb, P. Gittonb ,L. d'Arcioa, P. Fabrya, F. Puechb, M. Fridlunda, M. Schoellerb, A. Glindemannb E. Bakkerd, A. Karlssona, A. Peacocka, S. Volontea, F. Paresceb, A. Richichib, *Darwin-GENIE: a nulling instrument at the VLTI*.
[28]: Sascha P. Quanza, Jens Kammererb, Denis Defr'erec, Olivier Absilc, Adrian M. Glausera, and Daniel Kitzmannd, *Exoplanet science with a space-based mid-infrared nulling interferometer*, 9 Aug 2018.
[29]: Brian A. Hicks, Richard G. Lyonb, Matthew R. Bolcarb, Mark Clampinb, Peter Petrone IIIc, Michael A. Helmbrechtd, and Joseph M. Howardb, Ian J. Millere, *Recent developments with the Visible Nulling Coronagraph*, Optical and Infrared Interferometry and Imaging V, edited by Fabien Malbet, Michelle J. Creech-Eakman, Peter G. Tuthill, Proc. of SPIE Vol. 9907, 99072O © 2016 SPIE.

[30]: Colin Dandumont, Denis Defrère, Jens Kammerer, Olivier Absil, Sascha P. Quanz, and Jérôme Loicq, *Exoplanet detection yield of a space-based Bracewell interferometer from small to medium satellites*,Journal of Astronomical Telescopes, Instruments, and Systems,SPIE, 2020.
[31]: Lucas Labadiea, Laëtitia Abel-Tiberini, Etienne LeCoarer, Caroline Vigreux-Bercovici, Brahim Arezki, Marc Barillot, Jean-Emmanuel Broquin, Alain Delboulbé, Pierre Kern,Volker Kirschner, Pierre Labeye, Annie Pradel, Cyril Ruilier, Pierre Saguet, *Recent Progress in Mid Infrared Integrated Optics for Nulling Interferometry*, Advances in Stellar Interferometry, edited by John D. Monnier, Markus Schöller, William C. Danchi, Proc. of SPIE Vol. 6268, 62682E, (2006).
[32]: Hsien-kai Hsiao, K. A. Winick, John D. Monnier and Jean-Philippe Berger, *An infrared integrated optic astronomical beam combiner for stellar interferometry at 3-4 μm*, 2009 Optical Society of America.
[33]: Wei-Jen Chen, Shane M. Eaton, Habibin Zhang, Peter R. Herman, *Broadband directional couplers fabricated in bulk glass with high repetition rate femtosecond laser pulses*, 2008 Optical Society of America.
[34]: Valérie Weber , Marc Barillot , Pierre Haguenauer , Pierre Kern , Isabelle Schanen-Duport , Pierre Labeye , Laurence Pujol , Zoran Sodnik, *Nulling interferometer based on an Integrated Optics combiner*, New Frontiers in Stellar Interferometry, edited by Wesley A. Traub, Proceedings of SPIE Vol. 5491 (SPIE, Bellingham, WA, 2004).
[35]: Lucas Labadie, Jean-Philippe Berger, Nick Cvetojevic, Roger Haynes, Robert Harris, Nemanja Jovanovic, Sylvestre Lacour, Guillermo Martin, Stefano Minardi, Guy Perrin, Martin Roth, Robert R. Thomson, *Astronomical photonics in the context of infrared interferometry and high-resolution spectroscopy*,Optical and Infrared Interferometry and Imaging V, edited by Fabien Malbet, Michelle J. Creech-Eakman, Peter G. Tuthill, Proc. of SPIE Vol. 9907, 990718© 2016 SPIE.
[36]: Roberto Osellame, Giulio Cerullo, Roberta Ramponi, *Femtosecond Laser Micromachining Photonic and Microfluidic Devices in Transparent Materials*, Springer.
[37]: Rafael R. Gattas, Eric Mazur, **Femtosecond laser micromachining in transparent materials**, Nature Publishing Group, April 2008.
[38]: K. M. Davis, K. Miura, N. Sugimoto, and K. Hirao, *Writing waveguides in glass with a femtosecond laser*, Optical Society of America, November 1, 1996 / Vol. 21, No. 21 / OPTICS LETTERS.
[39] : Y. Shimotsuma, P.G. Kazansky, J. Qiu, K. Hirao, Phys. Rev. Lett. 91(24), 247405 (2003).
[40]: Robert Freedman and J. A. Hertz, *Theory of a Fermi glass*,Physical review. B, Condensed matter · February 1977.
[41]: Nevill Mott, *Electrons in glass*, Nobel Lecture, Cavendish Laboratory, Cambridge, England, 8 December, 1977.
[42]: Orazio Svelto, **Principles of Lasers**, fifth edition, Springer.
[43]: L. V.Keldysh, *Ionization in the field of a strong electromagnetic wave*, Soviet Physics Jetp ,Volume 20, Number 5 May, 1965.
[44]: Alexander Arriola, Simon Gross, Nemanja Jovanovic, Ned Charles, Peter G. Tuthill, Santiago M. Olaizola, Alexander Fuerbach and Michael J. Withford, *Low bend loss waveguides enable compact, efficient 3D photonic chips*, 2013 Optical Society of America.

[45]: W. Vogel,*Glass Chemistry*, Springer, 1994.
[46]: Francesco Ceccarelli , Simone Atzeni, Alessandro Prencipe, Raffaele Farinaro, and Roberto Osellame , Fellow, OSA, *Thermal Phase Shifters for Femtosecond Laser Written Photonic Integrated Circuits*, journal of lightwave technology, vol. 37, no. 17, September 1, 2019.
[47]: Bland-Hawthorn, Joss, and Pierre Kern. *Astrophotonics: a new era for astronomical instruments*. Optics express 17.3 (2009): 1880-1884.
[48]: Paiè, Petra, et al. *Selective plane illumination microscopy on a chip*. Lab on a Chip 16.9 (2016): 1556-1560.
[49]: Wang, Jianwei, et al. *Integrated photonic quantum technologies*. Nature Photonics 14.5 (2020): 273-284.
[50]: Thompson, Mark G., et al. *Integrated waveguide circuits for optical quantum computing*. IET circuits, devices & systems 5.2 (2011): 94-102.
[51]: Birks, Timothy A., et al. *The photonic lantern*. Advances in Optics and Photonics 7.2 (2015): 107-167.
[52]: Jovanovic, Nemanja, et al. *Starlight demonstration of the Dragonfly instrument: an integrated photonic pupil-remapping interferometer for high-contrast imaging*. Monthly Notices of the Royal Astronomical Society 427.1 (2012): 806-815.
[53]: Bland-Hawthorn, Joss, et al. *PIMMS: photonic integrated multimode microspectrograph*. Ground-based and Airborne Instrumentation for Astronomy III. Vol. 7735. International Society for Optics and Photonics, 2010.
[54]: G. Corrielli, A. Crespi, R. Geremia, R. Ramponi, L. Sansoni, A. Santinelli, P. Mataloni, F. Sciarrino, and R. Osellame. *Rotated waveplates in integrated waveguide optics*. In: Nature Communications 5.May (2014), pp. 1–6.
[55]: L. Sansoni, F. Sciarrino, G. Vallone, P. Mataloni, A. Crespi, R. Ramponi, and R. Osellame. *Two-particle bosonic-fermionic quantum walk via integrated photonics*. In: Physical Review Letters 108.1 (2012), pp. 1–5.
[56]: R. Martinez Vazquez, R. Osellame, M. Cretich, M. Chiari, C. Dongre, H. J. Hoekstra, M. Pollnau, H. Van Den Vlekkert, R. Ramponi, and G.Cerullo. *Optical sensing in microfluidic lab-on-a-chip by femtosecondlaser-written waveguides*. In: Analytical and Bioanalytical Chemistry 393. (2009), pp. 1209–1216.
[57]: E. N. Glezer, M. Milosavljevic, L. Huang, R. J. Finlay, T.-H. Her, J. P. Callan, and E. Mazur. *Three-dimensional optical storage inside transparent materials*. In: Optics Letters 21.24 (1996), p. 2023.
[58]: S. Juodkazis, S. Matsuo, H. Misawa, V. Mizeikis, A. Marcinkevicius, H. B. Sun, Y. Tokuda, M. Takahashi, T. Yoko, and J. Nishii. *Application of femtosecond laser pulses for microfabrication of transparent media*. In: Applied Surface Science 197-198 (2002), pp. 705–709.
[59]: B. C. Stuart, M. D. Feit, S. Herman, A. M. Rubenchik, B. W. Shore, and M. D. Perry. *Nanosecond-to-femtosecond laser-induced breakdown in dielectrics*. In: Physical Review B 53.4 (1996), pp. 1749–1761.
[60]: M. Lenzner, J. Krüger, S. Sartania, Z. Cheng, C. Spielmann, G. Mourou, W. Kautek, and F. Krausz. *Femtosecond Optical Breakdown in Dielectrics*. In: Physical Review Letters 80.18 (1998), pp. 4076–4079.
[61]: Cerullo G., Osellame R., Taccheo S., Marangoni M., Polli D., Ramponi R & De Silvestri S. (2002). Femtosecond micromachining of symmetric waveguides at 1.5 μm

by astigmatic beam focusing. Optics letters, 27(21), 1938-1940.
[62]: S. Eaton, H. Zhang, P. Herman, F. Yoshino, L. Shah, J. Bovatsek, and A. Arai. *Heat accumulation effects in femtosecond laser-written waveguides with variable repetition rate*. In: Optics express 13.12 (2005), pp. 4708–4716.
[63]: Alexander Killi, A. Steinmann, J. Dörring, U. Morgner, M. J. Lederer, D.Kopf, and C. Fallnich. *High-peak-power pulses from a cavity-dumped Yb:KY(WO2)2 oscillator*. In: Optics Letters 30.14 (2005), pp. 1891–1893.

List of Figures

List of Tables